Search for Dark Matter with High-Energy Neutrinos

Miguel Gutiérrez González

Departamento de Física Teórica y del Cosmos

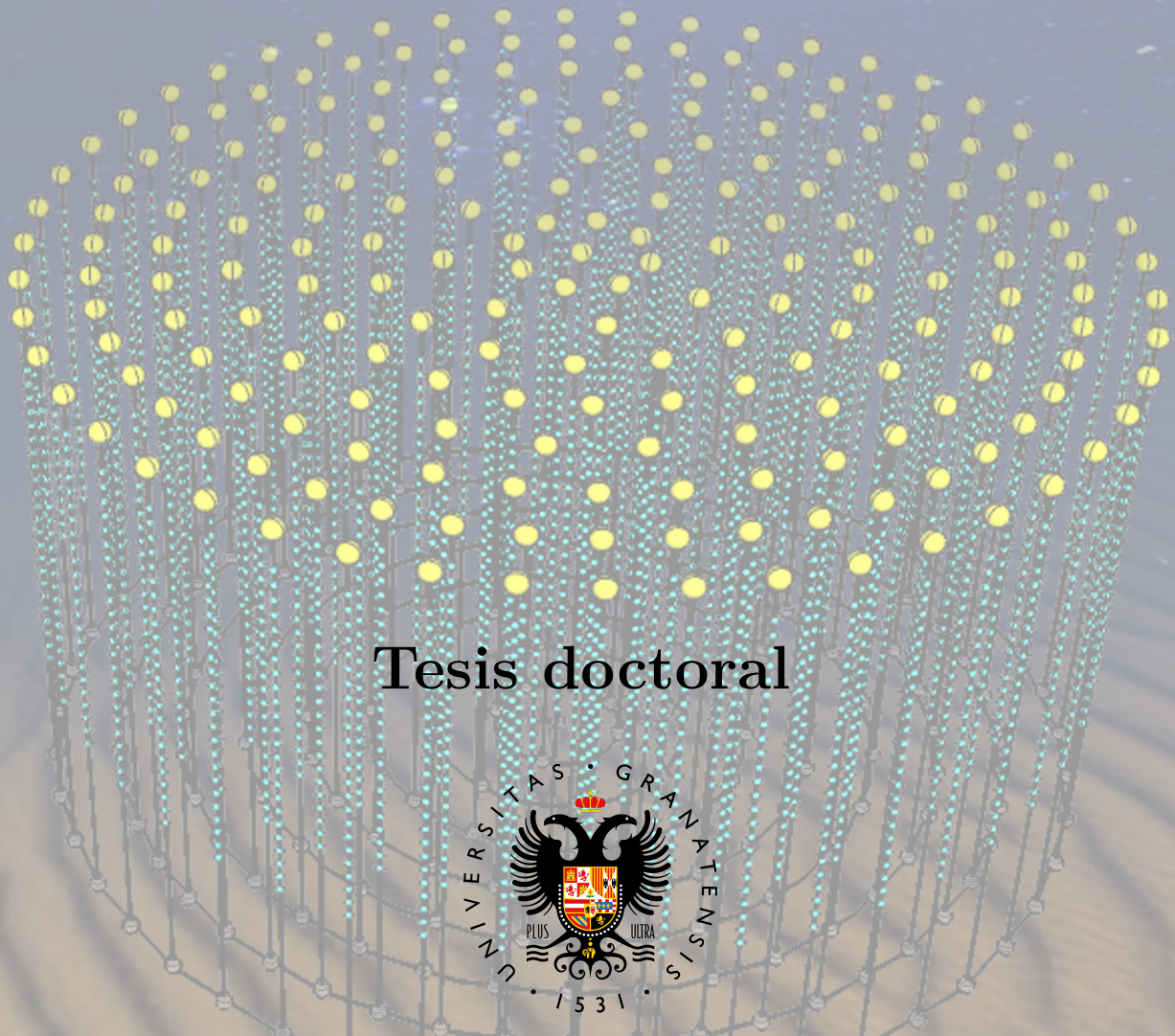

Tesis doctoral

UNIVERSIDAD DE GRANADA

Abril, 2024

Miguel Gutiérrez González

Search for Dark Matter with High-Energy Neutrinos

Thesis presented to obtain the PhD in *Física y Ciencias del Espacio* by the University of Granada.

Advisors: Prof. Manuel Masip Mellado
Prof. Sergio Navas Concha

UNIVERSIDAD DE GRANADA

Departamento de Física Teórica y del Cosmos
Abril, 2024

Editor: Universidad de Granada. Tesis Doctorales
Autor: Miguel Gutiérrez González
ISBN: 978-84-1195-302-3
URI: https://hdl.handle.net/10481/92346

Dedicated to my grandparents,
Miguel Gutiérrez Rueda and María del Carmen Moreno Rivera.

Declaration of Authorship

I, Miguel Gutiérrez González, declare that the thesis entitled "Search for Dark Matter with High-Energy Neutrinos" and the work presented in it are my own. I confirm that:

- This work was done wholly or mainly while in candidature for a research degree at this University.
- Where any part of this thesis has previously been submitted for a degree or any other qualification at this University or any other institution, this has been clearly stated.
- Where I have consulted the published work of others, this is always clearly attributed.
- Where I have quoted from the work of others, the source is always given. With the exception of such quotations, this thesis is entirely my own work.
- I have acknowledged all main sources of help.
- Where the thesis is based on work done by myself jointly with others, I have made clear exactly what was done by others and what I have contributed myself

Signed:

Acknowledgments

I would like to begin this section by expressing my gratitude to my PhD advisors, Profs. **Manuel Masip** and **Sergio Navas**, for their dedication, and support, both academically and personally. This thesis is the result of the work I have been able to carry out over these years, thanks to both of you.

I would like to thank **Dr. Daniel López**, who has been a tremendous help during the development of the experimental part of the analysis, serving as a guide and providing unquestionable support.

I would also like to express my gratitude to the KM3NeT collaboration – and within it, a special mention to the Dark Matter and Exotics group – as well as all the members of the *Departamento de Física Teórica y del Cosmos* at the University of Granada. I would like to give special thanks to **Dr. Rebecca Gozzini**, **Dr. Miquel Ardid**, and **Adrián Saina** (KM3NeT) for supervising my analysis within the collaboration, as well as to **Prof. José I. Illana** (UGR).

A special mention to **Dr. Marco Circella** for inviting me to the INFN-Bari to make a doctoral stay. I would also like to thank the rest of the team for making my days in the laboratory so nice.

Me gustaría también agradecer a mis padres, **Miguel** e **Isabel**, y a mi hermana **Patricia**, por todo el apoyo que me han brindado estos años y los valores que me han inculcado, sin los cuales no hubiese podido llegar hasta aquí. Del mismo modo, quiero agradecer al resto de mi familia (tíos, primos, abuelos...), y, en especial, a mis abuelos paternos, **Miguel** y **Mari Carmen**, a quienes dedico esta tesis. No pasa un día sin que me acuerde de vosotros y sé que ambos habríais estado muy orgullosos.

Me gustaría continuar dando las gracias al profesor **Antonio J. Lechuga**. Su pasión por la enseñanza y su dedicación como profesor dejaron en mí una huella muy profunda, y fue lo que, finalmente, me hizo decantarme por estudiar física.

Quiero agradecer también a mis amigos de Málaga, Madrid y Almería: **Lucas, Pelayo, Juanchi, Charo, Esther y Alejandro**, por aguantarme durante estos años y no haber dejado que la distancia sea un impedimento para estar a mi lado y servirme de apoyo.

Quiero también dedicar unas palabras similares a mis amigos de Granada: **Vicky, Carlos, Gloria, Paloma, Aitor, Damián, Roberto, Antonio, Borja, Belén** y **Vero**. Vosotros habéis hecho que mis años en esta ciudad hayan merecido la pena y se hayan convertido en una experiencia inolvidable.

A **José Manuel**, por ser mi amigo más antiguo y la persona con la que he pasado más horas en llamada durante esas noches trabajando en la tesis. A **Inma**, por haberme demostrado una y mil veces que puedo contar contigo para lo que necesite y por todas esas tardes haciendo planes alocados a lo largo de estos años. Y por último, a **Marina**, una de las mejores personas que he tenido la oportunidad de conocer, con la que siempre he podido contar para cualquier tipo de plan y que siempre me ha apoyado en todo lo que he hecho.

Acronyms

AGN Active Galactic Nuclei

AU Astronomic Unit

CC Charged Current

CMB Cosmic Microwave Background

CR Cosmic Ray

DAQ Data-acquisition

DM Dark Matter

DOM Digital Optical Module

DU Detection Unit

EM Electromagnetic

GC Galactic Center

IH Inverted Hierarchy

LHC Large Hadron Collider

MC Monte Carlo

NC Neutral Current

NH Normal Hierarchy

NMO Neutrino Mass Ordering

ORCA Oscillation Research with Cosmics in the Abyss

PDF Probability Density Function

PE Pseudo-experiment

PMTs Photo-Multiplier Tubes

PSF Point Spread Function

SD Spin-dependent

SHM Standard Halo Model

SI Spin-independent

SM Standard Model

SN Supernovae

ToT Time-over-Threshold

TS Test Statistics

WIMP Weakly Interacting Massive Particle

Preface

Dark matter is one of the great mysteries of modern particle physics. Cosmological and astrophysical observations suggest that it accounts for approximately 27% of the matter-energy density in the universe. Despite important efforts in recent decades, it has not been possible to directly confirm its existence. As a result, the basic properties of the particle that constitutes the dark matter are still unknown: we do not know its mass, its bosonic or fermionic nature, or if it is connected to the visible matter through interactions other than gravity.

In this thesis, we focus on what has been the most popular dark matter scenario during the past 40 years: the WIMP paradigm. Although there are other possibilities, a weakly interacting massive particle is the only candidate that may have interesting phenomenological implications in direct, indirect and collider searches. Here we will analyse the WIMP from both a phenomenological and an experimental perspective. In particular, we will be interested in the so-called indirect dark matter searches with high energy neutrinos. These are neutrinos produced when two dark matter particles annihilate in different astrophysical environments, then reach the Earth and are detected in a neutrino telescope.

In the first (phenomenological) part of the thesis our objective will be to define a dark matter model implying a neutrino signal from the Sun observable at telescopes. The model should explain the dark matter density that we see and should be consistent with the bounds from direct and collider searches. As we will show, this is a non-trivial feature for a WIMP model nowadays, since direct searches put stringent bounds on its interaction cross section that tend to increase the predicted relic density and also to reduce the capture rate by the Sun. In our analysis we will pay special attention to the high energy neutrino background produced by cosmic rays showering in the solar surface. The model that we propose, a Higgs portal with heavy sterile neutrinos, implies a monochromatic component in the neutrino flux that could be well above

this background.

In the second (experimental) part of the thesis we analyse the dataset from the KM3NeT/ORCA neutrino telescope in its 6-line configuration. Although ORCA is still under construction and currently provides just a fraction of what will be its final reach, our objective here is to explore and develop the techniques, the software and the possibilities of this telescope in the search for dark matter. In particular, we will employ a likelihood analysis to obtain a limit on the neutrino flux originating from WIMP pair annihilation in three cases ($b\bar{b}$, $\tau^+\tau^-$, W^+W^-) and we will deduce constraints on the spin-dependent and spin-independent cross sections.

The results in this thesis have been published in several articles and conference proceedings. In particular, our study of the solar backgrounds can be found in

- M. Gutiérrez and M. Masip, *The Sun at TeV energies: gammas, neutrons, neutrinos and a cosmic ray shadow,* Astropart. Phys. **119** (2020), 102440;
- M. Gutiérrez, M. Masip and S. Muñoz, *The Solar Disk at High Energies,* Astrophys. J. **941** (2022) no.1, 86,

whereas the dark matter model is described in

- P. de la Torre, M. Gutiérrez and M. Masip, *Monochromatic neutrinos from dark matter through the Higgs portal,* JCAP **11** (2023), 068.

Other results used here that have also been published concern mostly cosmic rays and air showers,

- M. Gutiérrez, G. Hernández-Tomé, J. I. Illana and M. Masip, *Neutrino events within muon bundles at neutrino telescopes,* Astropart. Phys. **134-135** (2022), 102646;
- C. Gámez, M. Gutiérrez, J. S. Martínez and M. Masip, *High energy muons in extensive air showers,* JCAP **01** (2020), 057.

The results related to KM3NeT can be found in

- M. Gutierrez, A. Saina *et al.* [KM3NeT], *Search for dark matter towards the Sun with the KM3NeT/ORCA6 neutrino telescope,* PoS **ICRC2023** (2023), 1406.

- A. Saina, M. Gutierrez *et al.* [KM3NeT], *Indirect Search for Dark Matter with the KM3NeT Neutrino Telescope,* PoS **ICRC2023** (2023), 1377.
- An article entitled *Indirect Search for Dark Matter with the KM3NeT Neutrino Telescope* is currently under the Collaboration internal review.

Miguel Gutiérrez González
February 21, 2024

Contents

1

Introduction

> The Standard Model is so complex it would be hard to put it on a T-shirt — though not impossible; you'd just have to write kind of small.
>
> Steven Weinberg.

1.1 The Standard Model

The Standard Model (SM) of particle physics [1, 2, 3] is one of science's most successful achievements, providing a satisfactory description of the physics at the subatomic level. It is a theoretical framework for an unified understanding of the particles and forces that define matter and its interactions, describing three of the four fundamental forces [4]:

i. **Electromagnetic:** Responsible for the interactions between electrically charged particles, including the attraction between protons and electrons that holds atoms together. The photon, a massless particle with zero electric charge, serves as the force carrier.

ii. **Weak**: Responsible for beta decays and other radioactive processes producing neutrinos. The $W^{\pm}$ and Z^0 bosons mediate these weak interactions.

iii. **Strong**: Responsible for binding quarks together to form hadrons, and for holding protons and neutrons together within an atomic nucleus. The mediator is the gluon, a massless particle that comes in 8 *color* charges.

While the SM is not in contradiction with any experimental particle physics observations, it still faces certain challenges and limitations, particularly in its

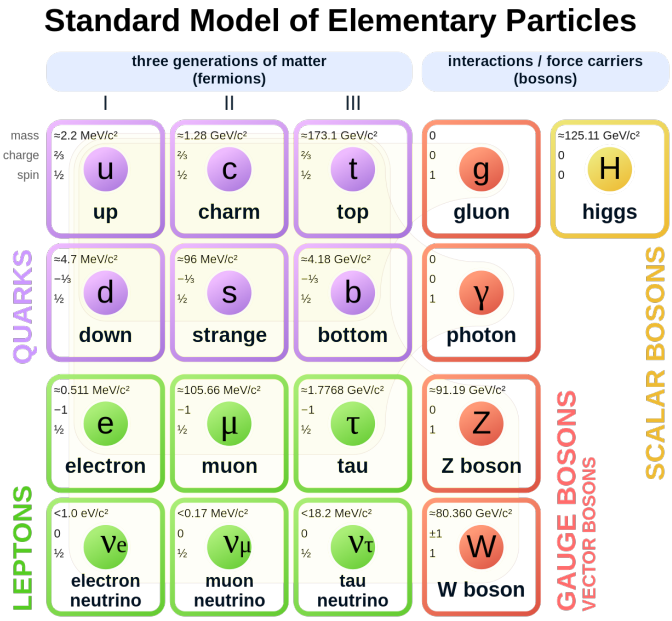

Figure 1.1: Particles composing the SM. Together, leptons and quarks define the matter sector of the SM. On the other side, the red particles are the mediators of the interactions, while the yellow particle is the Higgs boson. From Wikimedia.

treatment of **gravity** [5]. Gravity, mediated by the spin-2 graviton, is the weakest of the fundamental forces but responsible for the large-scale structure of the universe, including its expansion or the formation of stars and galaxies.

The elementary particles of the SM include fermions – with half-integer spin – and bosons. Fermions are divided into quarks (particles with *color*) and leptons (with no coupling to gluons), that can be charged (electrons, muons and taus) or neutral (neutrinos). In the SM, quarks and leptons come in three families or generations that only differ in their mass. Bosons, in turn, come in spin 0 and 1. The former includes the Higgs doublet, whereas the vector bosons serve as the intermediaries of the three interactions: the photon, the $W^{\pm}$ and Z^0 bosons, and the eight gluons. Fig. 1.1 shows the complete list of particles in the SM.

The SM has been probed at the quantum level at LEP [6, 7] and other precision experiments, providing the most precise prediction in Physics [8], namely, the 14 digits prediction in the anomalous magnetic moment of the electron. Despite that, there are some fundamental questions that today still remain unsolved:

1. **The Strong CP Problem** [9, 10]: The Standard Model predicts that strong

interactions could violate the CP symmetry and imply, for example, an electric dipole moment for the neutron 10^{10} times larger than current bounds. This forces that one of its parameters (the so-called θ parameter) must be tuned to a value 10^{-10} times smaller than the *natural* one.

2. **The Neutrino Mass Problem** [11]: The *renormalizable* SM predicts that neutrinos are massless. However, the flavor of neutrinos has been observed to oscillate, which can only be explained if they have a mass. Neutrino masses may appear through the dimension-5 Weinberg operator, but we do not know what is the scale or the matter content of the ultraviolet complete theory that generates this operator.

3. **The Baryon Asymmetry of the universe** [10, 12]: The SM can not explain why there is much more matter than antimatter in the universe. This asymmetry requires CP violating interactions and non-equilibrium conditions in the early universe that are not provided by the SM.

4. **The Existence of Dark Matter and Dark Energy** [13, 14]: Cosmological observations indicate that the SM only explains around 5% of the total matter-energy content of the universe: 26% should be dark matter and 69% dark energy. The SM must be *completed* as it does not contain any good candidates for the dark matter of the universe.

5. **The Unification of Forces** [15, 16, 17]: The strength of the three forces in the SM is fixed by independent couplings. However, the value of these couplings changes with the scale, and at energies around $M_{\text{GUT}} \approx 10^{16}$ GeV the value of the three couplings seems to coincide. This is a clear indication of a *Grand Unification* that would imply the presence of new particles and symmetries at that large scale.

6. **The Hierarchy Problem** [18]: The Higgs boson mass is not protected by any symmetry, and it is affected by quadratic loop corrections that tend to make it very large. The value that we observe is much smaller than the Planck Mass, $m_h^2 \approx 10^{-32} M_P^2$. This requires a fine tuning mechanism that could be related to new symmetries (*e.g.*, supersymmetry) or to a *multiverse* of disconnected regions where m_h^2 (and also the dark energy density) take different values.

For these reasons, one may expect new elements that during the next decades will complete the SM and will give us a better understanding of particle physics and cosmology.

In this thesis we focus on one of these issues: the dark matter (DM) of the universe. We will analyse this problem from both a theoretical and an experimental point of view. In the theory side, we will define a DM model that provides the *right* relic abundance, that is consistent with direct bounds and collider searches, and that uses heavy (TeV) neutrinos to generate masses for the SM neutrinos through an inverse *see-saw* mechanism. The main feature of the model is that the annihilation of DM pairs could produce a monochromatic signal of high energy neutrinos detectable at telescopes. Then, in the second part of the thesis, we analyse experimental issues related to the indirect search for DM using the neutrino telescope KM3NeT/ORCA. More precisely, we focus on the detection of a high energy neutrino signal that could have its origin in the annihilation of DM pairs captured by the Sun.

Before we describe these results, however, we would like to summarise in this introduction some properties of two SM particles playing an essential role in our search for DM: neutrinos and muons. In the last section of this chapter we also provide some basic notions of cosmology.

1.2 Neutrinos

The neutrino was first postulated by Wolfgang Pauli in 1930 [19] as a neutral, nearly massless particle to account for the missing energy in certain radioactive decays. Even today, in hadron colliders like the LHC they appear as missing energy. Just like for the rest of fermions, it has been established that there are three families of neutrinos (ν_e, ν_μ and ν_τ), but it is apparent that they are very *different* in several important aspects. First of all, they are much lighter than quarks and charged leptons. In particular, the combined results on neutrino oscillations (see below) in solar, atmospheric, reactor and collider experiments imply a spectrum with two *large* and one *small* mass differences[1] [20]:

$$\Delta m^2_{21} \ll |\Delta m^2_{31}| \sim |\Delta m^2_{32}|\,, \tag{1.1}$$

where $\Delta m^2_{ij} \equiv m^2_i - m^2_j$. This could be fit with a *normal hierarchy* (NH), $m_1 \ll m_2 < m_3$ or an *inverted hierarchy* (IH), $m_3 \ll m_1 < m_2$. In the first case the minimum values of m_2 and m_3 should be around 8.6×10^{-3} eV and 0.05 eV, respectively. For an IH the minimum values are $m_1 \approx 0.049$ eV and $m_2 \approx 0.05$ eV. For comparison, the mass difference between the electron and the muon is 1.05×10^8 eV (in this thesis we will use natural units with $\hbar = c = k_B = 1$).

In second place, as already mentioned, the flavor of a neutrino may change or *oscillate* as it propagates in vacuum or matter – in the latter case the oscillations also depend on the properties of the medium. This happens because the flavor and mass eigenstates do not coincide. Although this is actually also the case for the three quark and charged lepton families, the mass difference between neutrinos is so extremely small that they can propagate through long (macroscopic) distances as a coherent superposition of mass eigenstates. In vacuum, a simple calculation for distances L involving just two families with mixing angle $\theta_{\alpha\beta}$ gives [20],

$$P(\nu_\alpha \to \nu_\beta) = \sin^2(2\theta_{\alpha\beta}) \sin^2\left(1.27\,\frac{\Delta m^2_{\alpha\beta} L}{E}\right)\,, \tag{1.2}$$

where L must be written in km, E in GeV and $\Delta m^2_{\alpha\beta}$ in eV^2. An analogous calculation

[1] As we explain below, mass and flavour neutrino eigenstates do not coincide: flavor eigenstates $\nu_{\alpha=e,\mu,\tau}$ are related to the mass eigenstates, $\nu_{i=1,2,3}$, through the so called PMNS matrix U, $\nu_\alpha = \sum_i |U_{\alpha i}| \nu_i$.

involving the PMNS matrix, U, gives the result for three families [20]:

$$P(\nu_\alpha \to \nu_\beta) = \delta_{\alpha\beta} - 4\sum_{i<j}^{3} \mathrm{Re}\left(\sum_{i<j}^{3} U_{\alpha i}U_{\beta j}U^*_{\alpha j}U^*_{\beta i}\right)\sin^2\left(\frac{\Delta m^2_{ij}L}{4E}\right) + 2\sum_{i<j}^{3} \mathrm{Im}\left(\sum_{i<j}^{3} U_{\alpha i}U_{\beta j}U^*_{\alpha j}U^*_{\beta i}\right)\sin\left(\frac{\Delta m^2_{ij}L}{2E}\right), \tag{1.3}$$

where $\delta_{\alpha\beta}$ is the Kronecker delta. The PMNS matrix is [20]

$$U = \begin{pmatrix} c_{12}c_{13} & s_{12}c_{13} & s_{13}e^{-i\delta_{\mathrm{CP}}} \\ -s_{12}c_{23} - c_{12}s_{23}s_{13}e^{i\delta_{\mathrm{CP}}} & c_{12}c_{23} - s_{12}s_{23}s_{13}e^{i\delta_{\mathrm{CP}}} & s_{23}c_{13} \\ s_{12}s_{23} - c_{12}c_{23}s_{13}e^{i\delta_{\mathrm{CP}}} & -c_{12}s_{23} - s_{12}c_{23}s_{13}e^{i\delta_{\mathrm{CP}}} & c_{23}c_{13} \end{pmatrix}, \tag{1.4}$$

where $c_{ij} \equiv \cos\theta_{ij}$ and $s_{ij} \equiv \sin\theta_{ij}$ (see below). For a NH the best-fit values for the mixing angles among the three families are [20]:

$$\begin{aligned} &\theta_{12} = 33.82^\circ, \quad \theta_{13} = 8.61^\circ, \quad \theta_{23} = 48.3^\circ, \\ &\delta = 261^\circ, \\ &\Delta m^2_{12} = 7.39 \times 10^{-5}\,\mathrm{eV}^2, \quad \Delta m^2_{13} = 1.25 \times 10^{-3}\,\mathrm{eV}^2. \end{aligned} \tag{1.5}$$

This implies, for example, that a ν_e produced in the surface of the Sun with 41 TeV that interacts in the Earth has a 0.1 probability to be detected with the muon flavor;

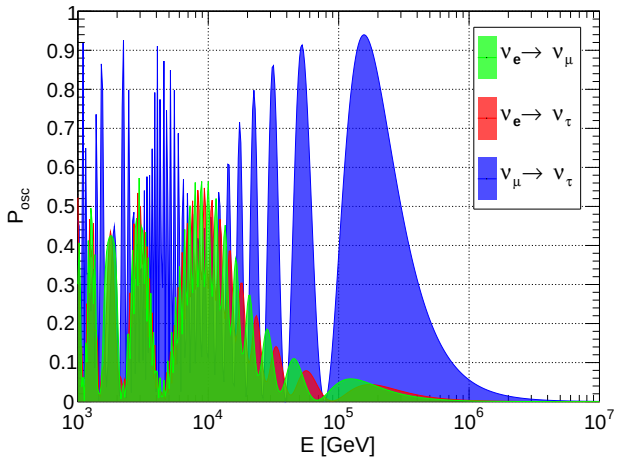

Figure 1.2: Probability of a ν_e to oscillate into a ν_μ or ν_τ, and for a ν_μ to oscillate into a ν_τ at a distance $L = 1$ UA.

at lower energies there will be multiple oscillations and the average probability of $\nu_e \to \nu_\mu$ conversion would be ~ 0.3. At lower energies even the $\nu_e \to \nu_\tau$ oscillations are significant within 1 AU: 0.1 probability at 35 TeV. Analogously, conversions $\nu_\mu \to \nu_\tau$ will mostly occur at $E \leq 10^6$ GeV with an average probability ~ 0.45. These results can be observed in Fig. 1.2. Therefore, oscillations are not negligible even at these relatively high energies due to the large distance (1 AU) between the Sun and the Earth.

The third fundamental property that distinguishes neutrinos from quarks and charged leptons is that they only experience weak interactions. We observe charged currents (CC) $\nu_\ell \to \ell$ mediated by the $W^\pm$ and neutral currents (NC) $\nu_\ell \to \nu_\ell$ coupled to the Z^0 boson. For this reason, despite its wide presence in the universe, neutrinos are very difficult to detect. In this thesis we will use the neutrino cross sections with protons and neutrons provided in [21] (see Fig. 1.3-left for details). To illustrate how elusive this particle is, let us obtain the probability that a high energy ν_μ (or $\bar{\nu}_\mu$) produced in the center of the Sun reaches the surface without being absorbed through a CC interaction. We see in Fig. 1.3-right that neutrinos of 50 GeV escape the Sun with no interaction, at 200 GeV they have a 50% chance to reach the surface and at $E \approx 900$ GeV only 1% of them are able to reach the surface. In this calculation we have used the solar model described in Sec. §2.4.

It may also be interesting to estimate how likely it is that a neutrino propagating in water has an interaction. Fig. 1.4 shows the interaction length in water for a ν_μ

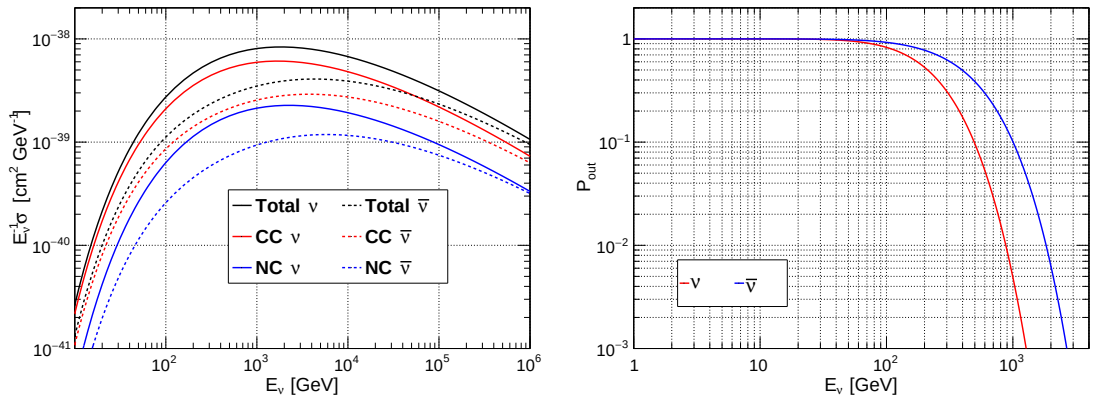

Figure 1.3: Left: Cross section for the CC, NC and CC+NC interaction of a muon neutrino or a muon antineutrino with a nucleon. Right: Probability that a ν_μ or $\bar{\nu}_\mu$ produced in the center of the Sun reaches the surface unscattered.

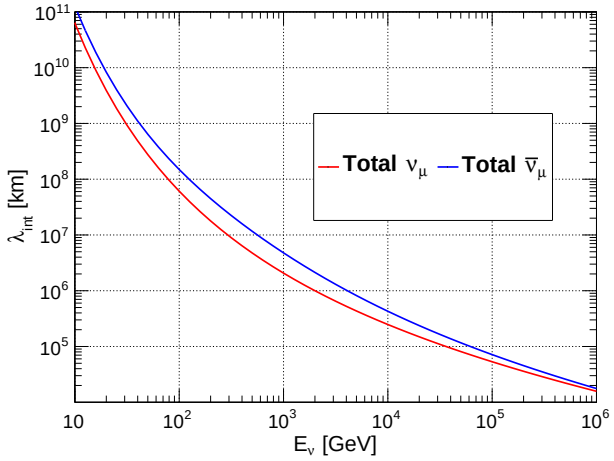

Figure 1.4: Total interaction length in water for muon neutrinos and muon antineutrinos.

and a $\bar{\nu}_\mu$. The interaction length of the antineutrino is longer than the neutrino one at low energies by a factor of two. We also observe a very strong dependence on the neutrino energy: only 1 out of 2×10^6 muon neutrinos of $E_\nu = 1$ TeV interact within one km of water, but 1 out of 2.3×10^3 at $E_\nu = 10^8$ GeV will do it within the same distance. The small interaction cross section of neutrinos with matter is the main reason why we need very large detectors like KM3NeT (described in §4) to register just a few events. On the other hand, this could also bring some interesting phenomenological possibilities: with neutrinos we can *see* very distant regions of the universe (they propagate unscattered through cosmological distances) or the interior of astrophysical objects.

As for the sources of high energy neutrinos (we focus on $E_\nu \geq 10$ GeV), one expects a variety of unresolved sources that would combine into the so-called *diffuse* neutrino flux. Indeed, in 2013 the IceCube detector discovered a flux of high energy extraterrestrial neutrinos at 30 TeV–1 PeV [22]. In addition, one very important feature of astrophysical neutrinos is that they can be used in astronomy: being electrically neutral, their trajectory is not affected by the magnetic fields present at different scales in the universe and points to their source. Although the results are still very limited, during the last years a few sources of high energy neutrinos have been discovered [23].

The known sources of neutrinos include:

- **Terrestrial sources**: Neutrinos produced in particle accelerators [24] or in nuclear reactors. They are also emitted by radioactive materials.
- **Solar neutrinos**: Neutrinos from the nuclear reactions that synthesise He from H in the Sun.
- **Atmospheric neutrinos**: From cosmic rays (CRs) that reach the Earth and produce air showers (see Secs. §2.2 and §2.3) [25].
- **Supernova (SN) explosions**: A star in its final phase (protoneutron star) is so dense that only neutrinos can escape its core: a significant fraction of energy in a SN explosion is emitted as neutrinos [26].
- **Active Galactic Nuclei** (AGN): A fraction of the immense gravitational energy liberated by accreting matter falling into the nucleus of these galactic nuclei is emitted as neutrinos [27].
- **Cosmological and cosmogenic neutrinos**: The first ones are a relic from the Big Bang, whereas cosmogenic neutrinos come from the interactions of CRs with Cosmic Microwave Background (CMB) photons at GZK energies (see Sec. §2.1).

Fig. 1.5 shows the relevance of these sources at different neutrino energies.

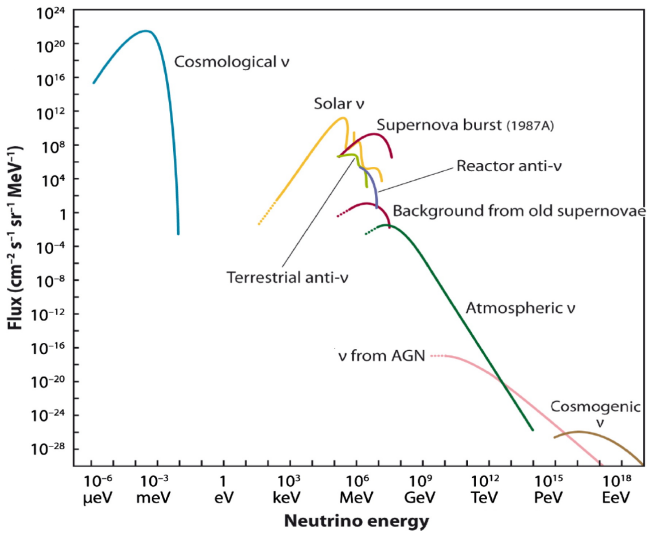

Figure 1.5: Different fluxes of neutrinos reaching the Earth, together with the sources that produce them – if known. From [28].

1.3 Muons

The muon, discovered in 1936 by C. D. Anderson and S. Neddermeyer [29], is a massive copy of the electron: $m_\mu = 105.7$ MeV versus $m_e = 0.51$ MeV. This larger mass makes it very different from a phenomenological point of view. First of all, it makes the muon unstable: it decays weakly,

$$\mu^- \to e^- + \bar{\nu}_e + \nu_\mu \,, \tag{1.6}$$

with a lifetime of $\tau_\mu \approx 2.2\,\mu$s. This may look brief, but the muon is, after the neutron, the longest lived of all the unstable elementary particles. In addition, at high energies its lifetime is Lorentz dilated, so that its decay length $\lambda_\mu \approx \beta c\tau\gamma$ becomes ~ 628 km at 100 GeV. But what makes the muon really different from the electron is its ability to propagate in matter: it is a factor of $m_\mu^2/m_e^2 \approx 4.2 \times 10^4$ more penetrating than an electron and it can cross more matter than any other particle except for the neutrino. Let us be a bit more specific.

The main processes where a muon loses energy are [30]:

- **Ionization**. A charged particle moving in a medium frees the electrons that were trapped in atoms. Since the typical length between consecutive ionizations is very short, it can be considered a continuous energy loss. This is the dominant source of energy loss for a muon at $E_\mu < 500$ GeV.

- **Radiative losses**. These are larger energy depositions caused by stochastic processes that have a much larger interaction length (a *radiation* length). In each interaction the muon will lose a fraction of energy that can be from very small to close to 1. We distinguish three types of interactions:

  i. **Bremsstrahlung**: the muon interacts with the electric field of a nucleus in the medium, goes off-shell and emits a photon.

  ii. **Pair production**: the muon emits a photon that fluctuates into an e^+e^- pair that goes on-shell after interacting with the EM field of a nucleus.

  iii. **Photonuclear interactions**: the muon emits a photon that converts into an off-shell ρ meson, that then interacts hadronically with a nucleus.

Fig. 1.6 shows the cross section for the three stochastic processes in water as a function of the fraction of the energy lost in the interaction, $x = E/E_\mu$, for $E_\mu = 1$ TeV.

The energy loss due to ionization for muons of kinetic energy $T_\mu > 100$ MeV is approximately constant, while its average energy loss due to radiative processes per

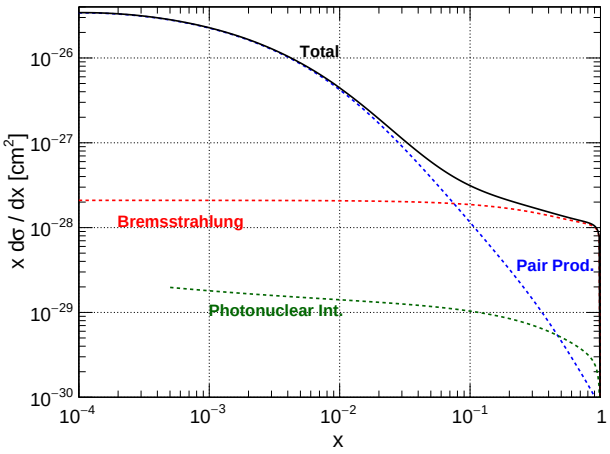

Figure 1.6: Cross section of the radiative processes during muon propagation in water as a function of the fraction of the energy for a muon with energy $E_\mu = 1$ TeV. The pair production process dominates at low energy, while at higher energy Bremsstrahlung becomes dominant.

unit depth is proportional to the energy of the muon [30]. Therefore, the total energy loss per unit length can be written as

$$-\left\langle \frac{\mathrm{d}E_\mu}{\mathrm{d}\ell} \right\rangle = a + b\,E_\mu\,, \tag{1.7}$$

where a and b depend on the medium but not on the muon energy. In water, for example, we have $a = 0.274$ GeV m^{-1}, $b = 0.000349$ m^{-1} [30]. Notice that at energies above $E_c = a/b$ the loses will be dominated by stochastic processes. In our analysis we will also need to propagate muons in a very different environment: the Sun. As we explain in next chapter, the matter in the Sun is partially ionised, what slightly reduces the continuous energy loss. But the main difference in the muon propagation there with respect to water or the Earth's atmosphere is that near its optical surface the Sun is much thinner, and muons of $E \approx 1$ TeV will be able to propagate and cross very long distances before they lose energy. This increases their probability to decay and produce neutrinos, which is one of the reasons (see next chapter) why the high-energy neutrino flux from the Sun is larger than the atmospheric one. For the Sun, an explicit calculation [31] of the three radiative cross sections yields

$$-\left\langle \frac{\mathrm{d}E_\mu}{\mathrm{d}t} \right\rangle = (1 - r_{\mathrm{ion}})\left[r_{\mathrm{H}}\left(a^{\mathrm{H}} - a^{\mathrm{He}}\right) + a^{\mathrm{He}}\right] + \left[r_{\mathrm{H}}\left(b^{\mathrm{H}} - b^{\mathrm{He}}\right) + b^{\mathrm{He}}\right] E_\mu\,, \tag{1.8}$$

being $a^{\mathrm{H}} = 4.8$ MeV cm^2/g, $a^{\mathrm{He}} = 2.8$ MeV cm^2/g, $b^{\mathrm{H}} = 2.1 \times 10^{-6}$ cm^2/g, $b^{\mathrm{He}} = 1.6 \times 10^{-6}$ cm^2/g, r_{ion} the fraction of ionised matter deduced from the Saha equation, r_H the fraction of hydrogen in the Sun and t the *depth* crossed by a particle as it propagates. The depth – also referred to as *column density* – between two points characterises the amount of matter that the particle faces when it propagates between the two points. It is defined as the density times the length or

$$t = \int_0^L \rho(\ell)\, \mathrm{d}\ell\,, \tag{1.9}$$

and its units are g/cm^2 or km w.e. (km of water equivalent). For example, if crossed vertically, the atmosphere has a total depth of 1000 g/cm^2, equivalent to 10 metres of water.

Fig. 1.7 shows the reach of a muon (we define it as the distance crossed before its energy is reduced to 10 GeV) at different energies in water ($\rho = 1$ g/cm^3). In the solar medium a significant fraction of high-energy muons will decay with $E > 10$ GeV, as their reach is larger than their decay length. For example, a 1 TeV muon produced in the solar medium at a depth of 100 g/cm^2 below the optical surface (the matter density there is around 2.3×10^{-6} g/cm^3) has a reach of 9.7×10^4 km, versus a decay length of 6.6×10^3 km. Notice that in the Earth's atmosphere a TeV muon will reach the ground and lose there all its energy before decaying.

A final aspect of the muon propagation in matter that will be very relevant in

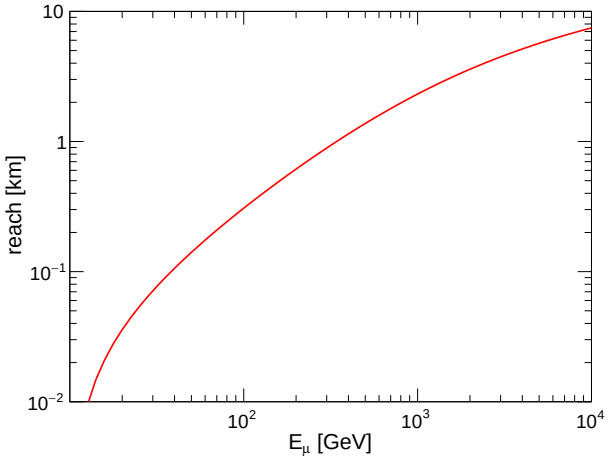

Figure 1.7: Reach in water of a muon as a function of its energy.

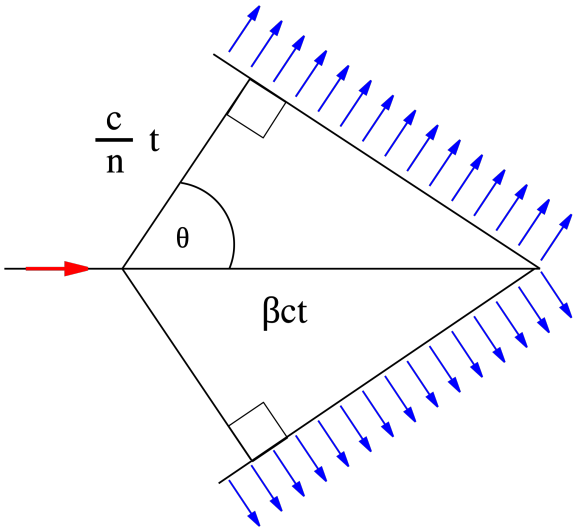

Figure 1.8: Scheme for a Cherenkov emission. The particle is moving with velocity βc while the phase velocity in the medium is c/n. In a time t the charged particle travels a distance βct while the emitted light travels a distance ct/n. From A. Horvath under Creative Commons license.

the work presented in this thesis is the emission of **Cherenkov radiation** [32, 33, 34], named after Pavel Cherenkov. A charged particle moving faster than c/n in a dielectric medium, being c the speed of the light in vacuum and n the refractive index of the medium, emits light. The particle excites the electrons in the atoms, that go back to the ground state with an emission along the direction of the track. This asymmetric emission along the trajectory interferes and leads to the appearance of a cone-like light signal called Cherenkov light. Fig. 1.8 shows the general scheme behind the emission of this light. The emission angle is related to the velocity of the particle,

$$\cos\theta = \frac{1}{\beta n}. \tag{1.10}$$

At very high energies β is close to 1 and the emission angle does not depend on the energy of the particle, but only on the refractive index of the medium. For example, in water $n \approx 1.35$ and $\theta \approx 42^{\circ}$.

Cherenkov light is not monochromatic, but it is emitted in a wide range of frequencies. The number of photons $\mathrm{d}N$ emitted per path length within a wavelength interval $\mathrm{d}\lambda$ is given by

$$\frac{\mathrm{d}^2 N}{\mathrm{d}\ell\,\mathrm{d}\lambda} = \frac{2\pi\alpha}{\lambda^2}\left(1 - \frac{1}{\beta^2 n^2}\right), \tag{1.11}$$

with $\alpha \approx 1/137$ the fine-structure constant. Due to the dispersion effects, most of the Cherenkov radiation produced in water lies in the ultraviolet and blue side of the spectrum. In particular, for a wavelength in the $300 - 600$ nm range, where most water-based neutrino telescopes operate, the number of emitted photons per unit of track longitude is

$$\frac{\mathrm{d}N}{\mathrm{d}\ell} \approx 340\,\mathrm{cm}^{-1}. \tag{1.12}$$

Finally, the Cherenkov condition on the velocity of the charged particle translates into a threshold energy,

$$E_{\mathrm{th}} \approx \frac{m_0}{\sqrt{1 - \frac{1}{n^2}}}. \tag{1.13}$$

In water, it implies a threshold kinetic energy of $T_{\mathrm{th}} = 0.25$ MeV for electrons or $T_{\mathrm{th}} = 53$ MeV for muons [35, 36].

1.4 Cosmology

We would like to finish this introductory chapter by giving some elements of cosmology, since cosmological observations provide the framework to understand what the properties of the DM particle should be.

Our current cosmological model is known as ΛCDM [37, 38], as it includes both a dark energy density (a vacuum energy density or *cosmological constant* $\Lambda \approx (10^{-4}\,\mathrm{eV})^4$) and cold (non relativistic) DM. It is based on the Friedman-Robertson-Walker metric, that for a *flat* universe (with a total energy density equal to the so-called critical energy density) depends on a single parameter: the scale factor $a(t)$. The scale factor changes with time according to Einstein's equations. Assuming that the content of the universe is a homogeneous and isotropic fluid in thermal equilibrium, the equations read

$$G_{\mu\nu} \equiv R_{\mu\nu} - \frac{1}{2} g_{\mu\nu} R = 8\pi G T_{\mu\nu}, \tag{1.14}$$

where $R_{\mu\nu}$ is the Ricci tensor, R the scalar curvature, $g_{\mu\nu}$ the metric tensor and $T_{\mu\nu}$ the stress-energy tensor of a perfect fluid. $T_{\mu\nu}$ can be expressed in terms of the energy density $\rho(t)$ and the pressure $p(t)$ in the fluid,

$$T_{\mu\nu} = \mathrm{diag}\left(\rho, -p, -p, -p, -p\right) . \tag{1.15}$$

The growth of the scale factor with time describes an expanding universe characterised by a temperature T that, in turn, decreases with time. In the early universe the particles of the SM are the building blocks of the cosmological fluid, where we can distinguish 3 components: matter (ρ_m), radiation (ρ_r) and vacuum (ρ_v), with $\rho_m + \rho_r + \rho_v = \rho_c$ or $\sum \Omega_i = 1$ with $\Omega_i \equiv \rho_i/\rho_c$.

The energy density in these three components evolves in a different way with the expansion dictated by the scale factor. The radiation (particles with a kinetic energy larger than their mass) is red-shifted: as a increases, the energy of each particle goes like E_0/a. Since the number density of particles dilutes as $1/a^3$, the energy density of this component will evolve like $\rho_r \propto 1/a^4$. In contrast, matter particles (with a mass larger than their kinetic energy) lose velocity but do not change their energy with the expansion, resulting in $\rho_m \propto 1/a^3$. As a consequence, an initial matter component like the DM of the universe or the nucleons at $T \approx 1$ MeV will be initially irrelevant ($\rho_m \ll \rho_r$), but since the expansion dilutes ρ_r faster than ρ_m, matter starts dominating the energy density of the universe at $T < 1$ eV. The universe was initially dominated by radiation (notice that all the SM particles *are* radiation at $T > m_{top}$),

but then matter became the dominant component dictating the expansion rate of the universe, which is expressed in terms of the Hubble parameter

$$H \equiv \frac{\dot{a}}{a} = \sqrt{\frac{\rho_{\rm tot}}{3M_P^2}}\,. \tag{1.16}$$

Currently it is the vacuum energy density (which is unaffected by the expansion) what dominates $\rho_{\rm tot}$ over radiation and matter energy density, with $\Omega_v h^2 \approx 0.331 \pm 0.018$, $\Omega_m h^2 \approx 0.122 \pm 0.018$, $\Omega_r h^2 \approx 3.74 \times 10^{-5}$ and

$$h = \frac{H_0}{100}\,\text{Mpc s km}^{-1}\text{m}^{-1}, \tag{1.17}$$

where $H_0 = 73.4^{+0.99}_{-1.22}$ (km/s)/Mpc [1] is the Hubble constant [39].

In this thesis we consider that our DM candidate, χ, is a WIMP (*Weakly Interacting Massive Particle*), *i.e.*, a particle with a relatively large mass that is connected with the Standard Model through a weak interaction [41]. The evolution of a WIMP constituting the DM in the early universe can be easily understood within this cosmological framework. As we have already mentioned, a comoving volume grows due to the expansion and dilutes the number density of particles of a given specie ϕ like $n_\phi \propto a^{-3}$. Therefore, the expansion reduces the total energy of the radiation contained in that volume (*i.e.*, the fluid does work against the rest of the universe with the expansion), but the total entropy will stay constant: we assume an adiabatic regime where the universe evolves following a sequence of states in thermal equilibrium, with no transfer of heat from one comoving volume to another one. Thus, the ratio between the number density of particles of a specie and the total entropy density, known as the *abundance*, is a convenient way to characterise the evolution of the species: it would be constant if no particles of this type were created nor destroyed. In thermodynamic equilibrium we have [42]

$$Y_{\phi,\rm eq} \equiv \frac{n_{\phi,\rm eq}}{s} = \frac{45}{4\pi^2}\frac{g_\phi}{g_{*s}}x^2\,K_2(x), \tag{1.18}$$

where $x = m_\phi/T$, g_ϕ accounts for the degrees of freedom of ϕ, g_{*s} is the effective number of massless degrees of freedom in the thermal bath [43, 44] and $K_{i=1,2}(x)$ are the modified Bessel functions of the second kind.

[1] Although we consider the value of the Hubble constant obtained in Ref. [39], there is a tension between direct observations of distant galaxies (around 73 (km/s)/Mpc) and the ones preferred by CMB data (for example, $H_0 = 67.0 \pm 3.6$ (km/s)/Mpc in Ref [40]). This anomaly is known as the *Hubble tension*.

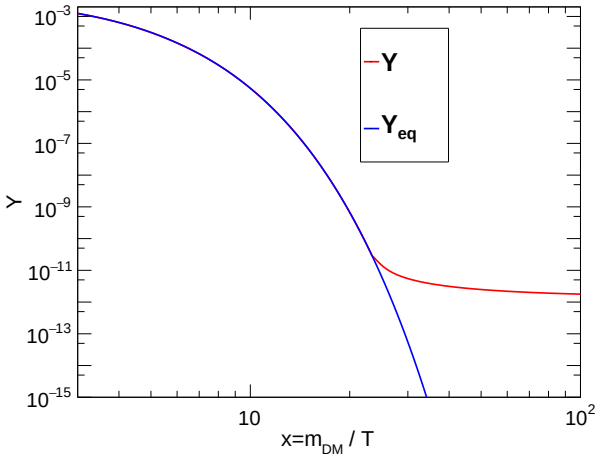

Figure 1.9: Abundance Y of a DM particle in the equilibrium during freeze-out. The blue line represents the equilibrium abundance and the red line the real one, that freezes-out at $T \approx m_\chi/20$. This plot corresponds to the WIMP model that we propose in Sec. §3.2.

In the WIMP paradigm, at temperatures larger than m_χ the DM particles χ are in equilibrium. This means that the reactions

$$\chi\bar{\chi} \leftrightarrow \gamma\gamma \tag{1.19}$$

go with the same frequency in both directions and the equilibrium abundance $Y_{\chi,eq}$ is of order $1/g_{*s}$. As the universe expands and the temperature becomes $T < m_\chi$, however, the equilibrium abundance decreases exponentially (see Fig. 1.9), as just the photons in the tail of the thermal distribution have enough energy to produce DM pairs. However at some point the species χ will depart from the equilibrium, and its abundance will eventually *freeze-out*. The evolution of the abundance with T or $x = m_\chi/T$ can be estimated using

$$\frac{\mathrm{d}Y_\chi}{\mathrm{d}x} = -\frac{x\,\langle\sigma_{\mathrm{ann}}|v|\rangle s}{H(m)}\left(Y_\chi^2 - Y_{\chi,\mathrm{eq}}^2\right), \tag{1.20}$$

where $\langle\sigma_{\mathrm{ann}}|v|\rangle$ is the thermal average of the cross section times the velocity [45]:

$$\langle\sigma_{\mathrm{ann}}|v|\rangle = \frac{1}{8Tm_\chi^4 K_2^2(x)}\int_{4m_\chi^2}^{\infty}\sqrt{s}\left(s-4m_\chi^2\right)K_1(\sqrt{s}/T)\sigma_{\mathrm{ann}}\,\mathrm{d}s. \tag{1.21}$$

The equations above express that the smaller the annihilation cross section, the earlier χ decouples and the larger its final *relic abundance*. Today, the contribution of the relic to the critical energy density would just be

$$\Omega_\chi h^2 = 2.75 \times 10^8 \, \frac{m_\chi}{\text{GeV}} Y_\infty, \tag{1.22}$$

where Y_∞ is the abundance today.

Part I

Phenomenology

2

Background for dark matter searches with neutrinos

> Not only is the universe stranger than we think, it is stranger than we can think.
>
> W. Heisenberg.

In this thesis we are interested in the high-energy neutrinos produced by the annihilations of WIMPs in the Sun. As it happens in any search for new physics, it will be crucial to understand and to characterise the neutrino fluxes that we expect as a background in these searches. All cosmic neutrinos of energy above 1 GeV appear as secondaries produced in the hadronic collisions of cosmic rays. In particular, when observing the Sun the two main sources of high energy neutrinos are the *cascades* produced by CRs in the Earth's atmosphere (these are commonly called *atmospheric neutrinos*) and in the surface of the Sun. In this chapter we discuss these neutrino backgrounds using both Monte Carlo simulators (the air shower simulator CORSIKA) and cascade equations.

2.1 Cosmic rays

The discovery of CRs opened a new channel for the observation of the universe. In 1912, Austrian physicist Victor Hess performed a series of balloon experiments [46, 47] to measure the ionization of the atmosphere at different altitudes. He found that it increases with altitude and that there are no differences between day or night or even during eclipses, and he concluded that it should be produced by some ionizing radiation coming from beyond the Earth and beyond the Solar System. Hess' discovery was met with scepticism, as it was believed that the Earth's atmosphere, with a depth equivalent to 10 metres of water if crossed vertically, was too thick to allow extraterrestrial radiation to penetrate. However, several experiments confirmed the existence of what soon was known as *cosmic rays*. The study of CRs during more than a century has had a profound impact on physics and astronomy, providing a better understanding of the universe both at short and long distances. On one hand, it has brought the discovery of antimatter or new particles produced by the cosmic radiation; on the other hand, it has revealed a large number of astrophysical objects that before could only be seen with light (or not seen at all). Indeed, CRs and their secondary gamma rays and neutrinos, together with gravitational waves, provide alternative channels that allow for a more complete picture of the cosmos.

CRs are high-energy particles, primarily protons and atomic nuclei, that travel through space at near-light speed. They originate from a variety of sources, including supernovae, active galactic nuclei or pulsars. They have been used to study the composition of the interstellar medium, the dynamics of supernova explosions or the structure of magnetic fields in different environments. Nowadays CRs continue to be an active area of research. Let us briefly review some aspects that will be relevant in the calculation of the neutrino background in DM searches.

Origin and composition

The origin of CRs includes:

i. Supernovae remnants: When a very massive star dies, it explodes into a supernova. It produces a shock wave of energy that, through a diffusive cycle that may repeat many times, can accelerate protons up to $\sim 10^6$ GeV.

ii. Pulsars (neutron stars): The stellar remnant of the massive star is small but incredibly dense, and it may be spinning very rapidly. When the rotation and

the magnetic axes do not coincide, the star generates strong electric fields that can accelerate protons up to $\sim 10^9$ GeV with a single push.

iii. Active galactic nuclei (AGN): An active galaxy has a supermassive black hole with accreting matter in its center. The accretion disk produces perpendicular shock fronts that can accelerate diffusively a charged particle up to 10^{12} GeV, whereas the intensive electromagnetic fields near the center may work up to the same energies with a single push. The first mechanism would be favoured if the CRs of highest energy (above 10^{10} GeV, see below) are iron, whereas the second mechanism involves a more dense medium (iron nuclei should fragment) and would favor proton primaries.

The CR energy spectrum is a simple power law that extends up to 10^{11} GeV, as shown in Fig. 2.1 – events with energy higher than 10^{11} GeV are still seen, but they are extremely uncommon.

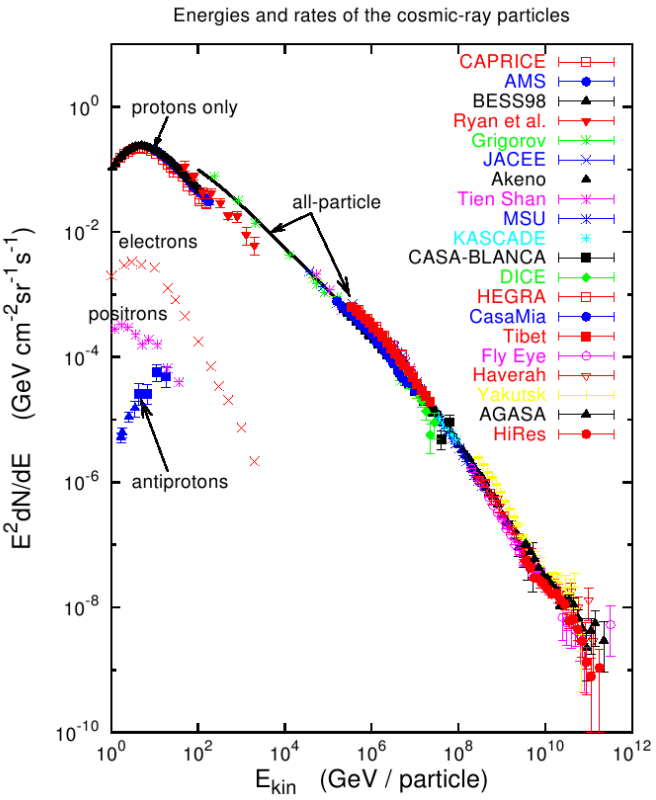

Figure 2.1: Energy spectrum of the CRs. From [48].

The number of CRs crossing the unit area orthogonal to a given direction, per unit of energy and unit of solid angle can be expressed as

$$\Phi(E) = K\,E^{-\gamma}, \tag{2.1}$$

with a spectral index $\gamma \approx 2.7$ that changes slightly with the energy. More precisely, there are three features distinguishable in the CR spectrum: the *knee* at $10^{6.5}$ GeV, the *ankle* at $10^{9.5}$ GeV, and the GZK cut-off around $10^{10.5}$ GeV. In these points the spectral index clearly changes. The causes of these changes are thought to be related to the dominant acceleration mechanism and the dominant composition at different energies. CRs of energy below E_{knee} would have been produced predominantly at supernova remnants in our own galaxy, with a maximum energy that slightly grows with the atomic number: the knee seems to appear first for protons and He, then C, and then heavier nuclei [49, 50]. Between E_{knee} and E_{ankle} the spectrum would be also dominated by galactic CRs, but from a different source: pulsars. We know that CRs of energy above E_{ankle} are mostly extragalactic, since a galactic source would imply directional anisotropies much larger than the ones observed. At these energies up to E_{GZK} the dominant sources are probably AGNs. The GZK (for Greisen-Zatsepin-Kuzmin) cut-off appears then when collisions of CRs with the CMB photons become inelastic, although its precise position depends strongly on the CR composition.

The composition of CRs is well known at lower energies, as experiments in balloons and satellites carry detectors that are large enough to access energies below 1 TeV. At higher energies the fluxes are so small that only very large surface detectors can register a few events, and the composition becomes much more difficult to determine. Although CRs are dominated by protons and helium nuclei, we can also find all the nuclei in the Solar System, as shown in Fig. 2.2.

In our analysis we will be interested in neutrinos of energy between 10 GeV and 10 TeV. We will take a CR flux dominated by hydrogen and ^{4}He, with slightly different spectral indexes below E_{knee}:

$$\begin{aligned} \Phi_p &= 1.3 \left(\frac{E}{\text{GeV}}\right)^{-2.7} \text{particles/(GeV cm}^2\text{s sr)}, \\ \Phi_{\text{He}} &= 0.54 \left(\frac{E}{\text{GeV}}\right)^{-2.6} \text{particles/(GeV cm}^2\text{s sr)}. \end{aligned} \tag{2.2}$$

The contribution of heavier nuclei has been taken into account by slightly increasing the flux of He, so that we correctly reproduce the total *all nucleon* flux,

$$\Phi_N(E) = \Phi_p(E) + 4^2\,\Phi_{\text{He}}(4E). \tag{2.3}$$

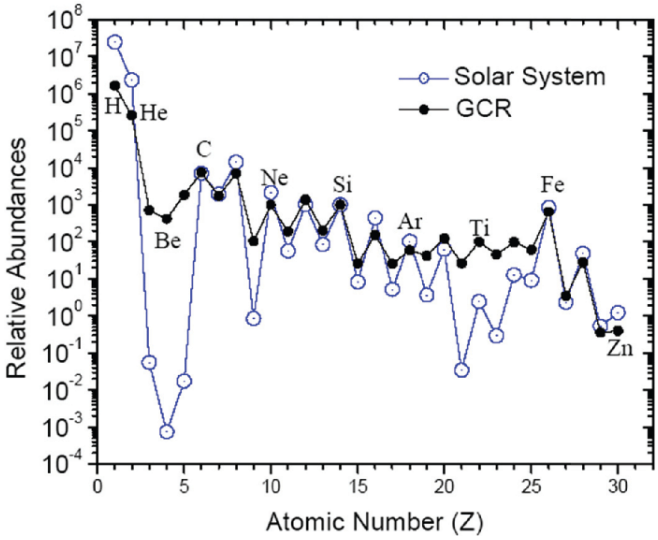

Figure 2.2: Composition of the galactic CRs compared to the composition of the Solar System. From [51].

The expressions in Eq. (2.2) imply a similar amount of hydrogen and helium nuclei at $E \approx 10\,\text{TeV}$.

The CR composition between the knee and the ankle is still uncertain, whereas the total CR flux in this region follows a power law with a larger spectral index, $\gamma \approx 3$:

$$\Phi = 330 \left(\frac{E}{\text{GeV}}\right)^{-3} \text{particles}/(\text{GeV cm}^2\text{s sr}). \tag{2.4}$$

At energies above the ankle, $E > 10^{9.5}$ GeV, the spectral index goes back to 2.7 until the CR flux hits the GZK limit. As mentioned before, when a CR of energy above $10^{10.5}$ GeV interacts with a CMB photon the center of mass energy is enough to produce a pion,

$$p + \gamma_{CMB} \to \Delta^+ \to p + \pi^0, \;\; n + \pi^+. \tag{2.5}$$

The decay of the charged pions will produce a *cosmogenic* neutrino flux at $E \approx 10^9$ GeV. Although this is a very interesting flux that is actively searched for in astroparticle observatories, in this work we will focus on neutrinos of lower energies, mostly generated by the CRs below E_{knee}, using expression (2.4) to describe the region around the ankle as well.

2.2 Air showers

Air showers are cascades with millions of secondary particles produced when a high-energy CR enters the Earth's atmosphere. Let us describe qualitatively their development for a primary CR proton of very high energy. It will initially collide with an air nucleus (78% of nitrogen and 21% oxygen, with smaller amounts of xenon, water vapor and CO_2) in the upper atmosphere. The collision will fragment the proton into a *leading baryon* carrying a significant fraction (*e.g.*, 20%) of the initial energy, plus a number of secondary hadrons, mostly pions and kaons, sharing the rest of the energy. The leading baryon will keep interacting every hadronic interaction length $\lambda_{\rm int}$ and producing more light mesons, whereas charged pions and kaons may interact and produce more pions of lower energy or they may decay producing leptons. The probability of an interaction or a decay of these light mesons will depend on the relative value of the interaction and the decay lengths: charged pions of energy above 30 GeV or kaons above 50 GeV will most likely interact in the air instead of decaying, whereas at lower energies they tend to decay. Therefore, very energetic light mesons will keep colliding and developing the hadronic shower until their energy is much smaller than the initial energy of the primary.

In turn, neutral pions produced in the collisions of the primary and secondary hadrons will decay instantly into two photons,

$$\pi^0 \to \gamma\gamma\,, \tag{2.6}$$

feeding the electromagnetic (EM) component of the hadronic air shower. In the atmosphere, photons will typically convert into e^+e^- pairs after a radiation length X_0, whereas electrons and positrons will radiate photons after a similar length. The hadronic collisions of photons have a typical length 200 times longer than the conversion to pairs, so most of the hadronic energy tends to be transferred through π^0's to electrons and photons and never comes back.

The final result is a shower that increases fast the number of particles, mostly electrons and photons, until it reaches a maximum at $X_{\rm max}$. At deeper depths the atmosphere is able to absorb most of these EM energy and only a small fraction of energy (depending on the initial one) reaches the surface. In turn, the production of muons and neutrinos grows as the shower develops; muons are much more penetrating than electrons and define a component of the air shower also detectable at the surface or in a neutrino telescope.

As we will see in Sec. §2.4, a similar development would also be expected when a CR reaches the surface of the Sun, but not when it penetrates the surface of the

Moon. There, the medium is much more dense, and secondary pions and kaons would not decay and produce leptons until their energy is much lower. The key here is that the atmosphere behaves like a hadronic calorimeter but extremely thin, so that a fraction of charged pions and kaons of GeV and even some at TeV energies can decay before they lose their energy.

Notice also that, if the primary was a He nucleus of energy E, the initial collision would break it and its constituents would be sharing its energy: a He air shower of energy E would be indistinguishable from the superposition of 4 nucleon showers each one of energy $E/4$. Only the all-nucleon flux is relevant in an estimate of the atmospheric neutrino background.

The secondary particles created in the air shower then collide with other atoms and molecules, creating even more particles. This process continues until the energy of the particles is too low to produce additional particles. The resulting shower of particles can spread over a surface area of several square kilometres, lasting for several milliseconds. Fig. 2.3 shows an schematic development of an air shower.

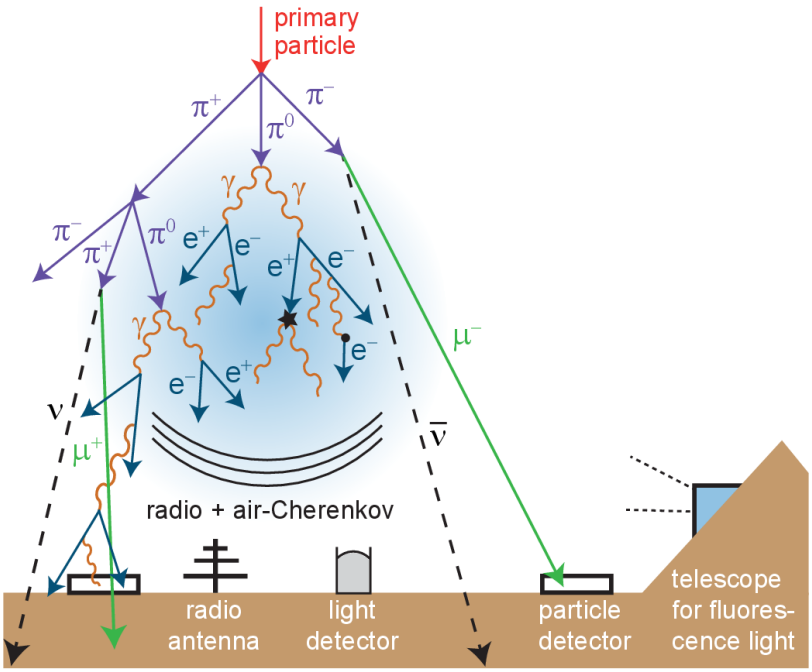

Figure 2.3: Scheme of the development of an air shower and the detection of the particles produced in it. From Ref. [52].

Cascade equations

We can obtain a precise estimate of the muon and neutrino fluxes resulting from an initial CR flux using cascade equations. These are coupled differential equations for all the especies in a shower: hadrons h, electrons and photons, muons and neutrinos. The equations describe how these fluxes evolve as they cross a depth t of matter in a medium of density ρ and a given compositon. The longitudinal development of the flux of particles type i satisfies

$$\frac{\mathrm{d}\Phi_i(E,t)}{\mathrm{d}t} = -\frac{\Phi_i(E,t)}{\lambda_i^{\mathrm{int}}(E)} - \frac{\Phi_i(E,t)}{\lambda_i^{\mathrm{dec}}(E,t)} + \sum_{j=h,\gamma,e}\int_0^1 \mathrm{d}x\,\frac{f_{ji}(x,E/x)}{x}\,\frac{\Phi_j(E/x,t)}{\lambda_j^{\mathrm{int}}(E/x)} + \sum_{k=h,\mu}\int_0^1 \mathrm{d}x\,\frac{f_{ki}^{\mathrm{dec}}(x,E/x)}{x}\,\frac{\Phi_k(E/x,t)}{\lambda_j^{\mathrm{dec}}(E/x,t)}\,, \tag{2.7}$$

where Φ_i is the differential flux (particles per unit energy, time and surface), t is the slant depth (defined in Eq. (1.9)) in g/cm^2, and $h = (p,\ n,\ \bar{p},\ \bar{n},\ \pi^{\pm},\ K^{\pm},\ K_L)$. The interaction and decay lengths λ_i^{int} and λ_i^{dec} of the species i, respectively, are expressed in g/cm^2:

$$\lambda_i^{\mathrm{int}} = \frac{m}{\sigma_i}, \tag{2.8}$$

$$\lambda_i^{\mathrm{dec}} = \rho\, c\, \beta_i\, \tau_i\, \gamma, \tag{2.9}$$

where m is the mass of the target, τ_i is the lifetime of the particle, σ_i the cross section for the interaction and ρ the medium density. Notice that for stable particles $\lambda^{\mathrm{dec}} \to \infty$ and for a non-interacting particle like a neutrino $\lambda^{\mathrm{int}} \to \infty$.

The interpretation of Eq. (2.7) is clear: the first two terms represent the loss of particles per unit depth due to interactions or decays. The structure of this terms can be deduced considering that the differential probability of interaction (or decay) is $\mathrm{d}t/\lambda_i^{\mathrm{int\,(dec)}}$. The third term represents the production of particles type i due to interactions of particles type j of higher energy, while the last term corresponds to their production in hadron and muon decays. Again, the interaction and decay lengths parametrise the interaction or decay probabilities, while the interaction (or decay) yields $f_{ji}^{(\mathrm{dec})}(x,E)$ express the number of particles type i carrying a fraction $x = E_i/E$ of the incident energy produced per unit x in one annihilation (or decay) of a particle type j and energy E.

We have parametrised all the yields of secondary particles produced in the interactions and decays of nucleons, charged pions and kaons of energy between 10 and 10^{11} GeV. To do that we have used the hadronic Monte Carlo SIBYLL

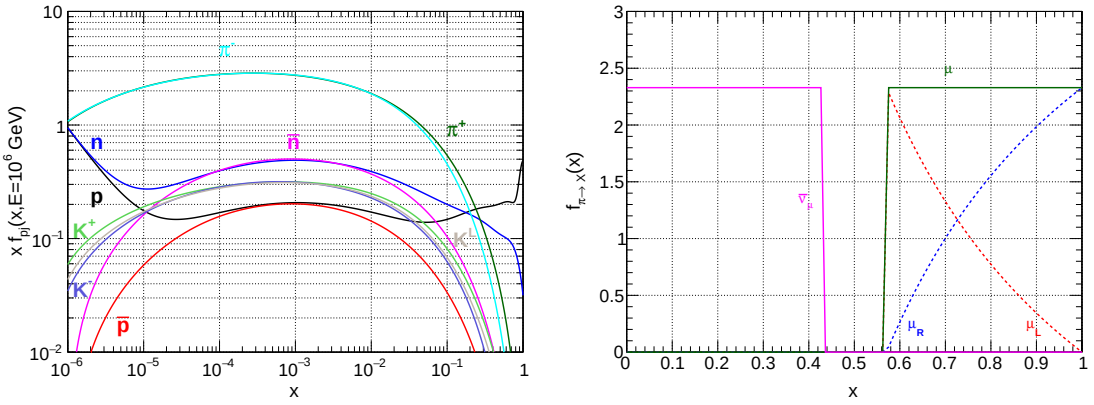

Figure 2.4: Left: yields for the collision of a proton with $E_p = 10^6$ GeV with a nucleus at rest as a function of the fraction of the energy carried by the particles, x. Right: pion decay yields.

[53]. Basically, we have simulated 10^4 proton, π^+ and K^+ collisions with a proton at rest and have fitted the distributions of the 9 secondary hadron species and gammas produced at 3 different energies (10^2, 10^6 and 10^{10} GeV). Then we have used interpolations between the fits, redefining the normalization of the fits at all energies between 1 and 10^{11} GeV to ensure energy conservation:

$$\sum_i \int_0^1 \mathrm{d}x \; x f_{hi}(x, E) = 1 \,. \tag{2.10}$$

Finally, we have used isospin symmetry to compute the yields in all hadronic collisions (*e.g.*, $f_{p\pi^+} = f_{n\pi^-} = f_{\bar{p}\pi^-} = f_{\bar{n}\pi^+}$).

In Fig. 2.4-left we illustrate our results: we plot all the yields for a proton primary of 10^6 GeV. Analogously, we have obtained the decay yields in pion and kaon decays [54] in the ultrarelativistic limit. In particular, we distinguish between the π^+ decays into muons of positive (right) and negative (left) helicity [55], as these muons give different neutrino distributions when they decay (see Fig. 2.4-right).

For the muon flux, an extra term has been included in the equations to account for energy loss,

$$\frac{\mathrm{d}\Phi_\mu(E,t)}{\mathrm{d}t} \subset -\left\langle \frac{\mathrm{d}E_\mu}{\mathrm{d}t} \right\rangle \frac{\mathrm{d}\Phi_\mu(E,t)}{\mathrm{d}E} - \Phi_\mu(E,t) \frac{\mathrm{d}}{\mathrm{d}E_\mu} \left\langle \frac{\mathrm{d}E_\mu}{\mathrm{d}t} \right\rangle \,. \tag{2.11}$$

The equations for the EM component in the atmospheric flux includes both the photons produced in hadronic collisions and decays via neutral pions and etas and

through electron bremsstrahlung, whereas electrons are produced in pairs by photon conversion and also in some kaon decays (*e.g.*, $K_L \to \pi^+ e\,\bar{\nu}_e$):

$$\frac{\mathrm{d}\Phi_\gamma(E,t)}{\mathrm{d}t} \supset \sum_{j=h} \int_0^1 \mathrm{d}x\, \frac{f_{j\gamma}(x,E/x)}{x}\, \frac{\Phi_j(E/x,t)}{\lambda_j^{\mathrm{int}}(E/x)} + \int_{x_{\min}}^1 \mathrm{d}x\, \frac{f_{e\gamma}(x,E/x)}{x}\, \frac{\Phi_e(E/x,t)}{\lambda_e^{\mathrm{int}}(E/x)}\,, \tag{2.12}$$

$$\frac{\mathrm{d}\Phi_e(E,t)}{\mathrm{d}t} \supset \int_0^1 \mathrm{d}x\, \frac{2\, f_{\gamma e}(x,E/x)}{x}\, \frac{\Phi_\gamma(E/x,t)}{\lambda_\gamma^{\mathrm{int}}(E/x)} + \int_0^{1-x_{\min}} \mathrm{d}x\, \frac{f_{e\gamma}(1-x,E/x)}{x}\, \frac{\Phi_e(E/x,t)}{\lambda_e^{\mathrm{int}}(E/x)}\,, \tag{2.13}$$

where $x_{\min}(E) = E^\gamma_{\min}/E$ and $f_{ee}(x,E) = f_{e\gamma}(1-x,E)$ (notice that in a bremsstrahlung the electron and photon exit with complementary energies). Including photo-hadronic collisions, the interaction lengths are:

$$\begin{aligned} \frac{1}{\lambda_\gamma^{\mathrm{int}}} &= \frac{7-3b}{9X_0} + \frac{\sigma_\gamma^{\mathrm{had}}}{m}, \\ \frac{1}{\lambda_e^{\mathrm{int}}} &= \frac{\int_{x_{\min}}^1 \mathrm{d}x\, \phi(x)}{X_0}, \end{aligned} \tag{2.14}$$

being $X_0 = 37.1\,\mathrm{g/cm}^2$ in the atmosphere and [56]:

$$\begin{aligned} f_{\gamma e}(x,E) &= \frac{\lambda_\gamma^{\mathrm{int}}(E)}{X_0}\,\psi(x); \qquad \psi(x) = \frac{2}{3} - \frac{b}{2} + \left(\frac{4}{3}+2b\right)\left(x-\frac{1}{2}\right)^2, \\ f_{e\gamma}(x,E) &= \frac{\lambda_e^{\mathrm{int}}(E)}{X_0}\,\phi(x); \qquad \phi(x) = x + \frac{1-x}{x}\,\left(\frac{4}{3}+2b\right). \end{aligned} \tag{2.15}$$

Later on we will apply these equations to find the flux of neutrinos produced by CR showers in the surface of the Sun. In the next section, however, we will obtain the neutrino flux from CR showers in the atmosphere using a publicly available Monte Carlo simulator, CORSIKA [57], which provides more precise results.

2.3 Atmospheric neutrino flux

The main background in any search for astrophysical neutrinos at telescopes is the flux of atmospheric neutrinos [58]. This flux is produced inside CR showers through leptonic (*e.g.*, $\pi^+ \to \mu^+\nu_\mu$) and semileptonic (*e.g.*, $K_L^0 \to \pi^- e^+ \nu_e$) decays of charged pions and kaons. At high energies, however, this *conventional* source of atmospheric neutrinos is strongly suppressed because light mesons tend to collide before they can decay. More precisely, these processes imply a spectral index in the neutrino flux one unit larger than the one in the parent CR flux, $E^{-2.7} \to E^{-3.7}$. This effect is softer at higher zenith angles, where secondary mesons travel longer distances in a thinner atmosphere, resulting in a 7 times larger atmospheric flux from horizontal than from vertical directions at $E \geq 1$ TeV.

At very high energies ($E_\nu \geq 100$ TeV) the dominant origin of the atmospheric neutrino flux is not the conventional one but the decay of charmed hadrons. D mesons and Λ_c baryons also have semileptonic decay modes (*e.g.*, $BR(D^+ \to \bar{K}^0 \mu^+ \nu) = 8.76\%$) and they decay promptly, with a much shorter lifetime than light mesons: up to $E \approx 10^7$ GeV their interaction length in air is longer than their decay length.

To estimate the atmospheric neutrino flux we have used the Monte Carlo simulator CORSIKA [57]. In particular, we have simulated 10^4 cascades with proton primaries of several energies ($E_p = 10^{2,3,\ldots,8}$ GeV) and have obtained the total neutrino yields $(\nu_i + \bar{\nu}_i)$,

$$f_{p\,\nu_i}(x, E) = \frac{\mathrm{d}N_{\nu_i}}{\mathrm{d}x}, \tag{2.16}$$

where x is the fraction of the primary proton energy carried by the neutrinos and $i = e, \mu$ (the flux of ν_τ from only D_s decays is negligible). We have then separated the conventional and charm components in the yields, $f_{p\nu_i}(x, E) = f^{(1)}_{p\nu_i}(x, E) + f^{(2)}_{p\nu_i}(x, E)$, and have performed a fit.

i. The first component, describing the flux from pion, kaon and muon decays, is different for the electron and the muon flavors:

$$f^{(1)}_{p\nu_i}(x, E) = A_i \, \frac{x^{B_i} \, (1-x)^{C_i} \, e^{-D_i x}}{E} \left(1 + \sqrt{\frac{m_\mu}{xE - m_\mu}}\right)^{-4}. \tag{2.17}$$

We provide the value of the parameters at the given energies in Table 2.1 (we use a logarithmic interpolation at intermediate energies).

ii. The second component accounts for the neutrinos from charm hadron decays:

$$f^{(2)}_{p\nu_i}(x, E) = A \, x^B \, (1-x)^C \, e^{-Dx}, \tag{2.18}$$

	10^3	10^4	10^5	10^6	10^7	10^8
E [GeV] $\times$ A_{ν_e}	10.0	37.7	38.8	29.5	26.9	27.2
B_{ν_e}	2.40	2.30	2.50	2.65	2.70	2.70
C_{ν_e}	2.0	2.2	2.4	2.7	4.0	8.0
D_{ν_e}	3.7	3.8	4.0	4.0	4.0	4.0
E [GeV] $\times$ A_{ν_μ}	0.55	1.14	2.18	1.40	1.35	1.75
B_{ν_μ}	2.60	2.50	2.50	2.65	2.70	2.70
C_{ν_μ}	3.0	3.0	4.0	4.5	5.0	5.0
D_{ν_μ}	4.6	4.7	5.0	5.0	5.0	5.0

Table 2.1: Values for the parameters used to fit the conventional atmospheric neutrino yield for a zenith angle of $\theta = \pi/4$.

being $A = 1.0 \times 10^{-4}$, $B = 1.8$, $C = 10.0$ and $D = 5.0$ independent of the energy and the flavour.

The fit is performed to reproduce the 3 lowest moments of the distributions for the analysed energies. For illustration, Fig. 2.5 gives the atmospheric neutrino yields in a proton shower of 10^4 and 10^6 GeV. We can observe the increasing relevance of neutrinos from charm decays with the energy.

Once we have these yields at all energies of interest we take the primary all-nucleon

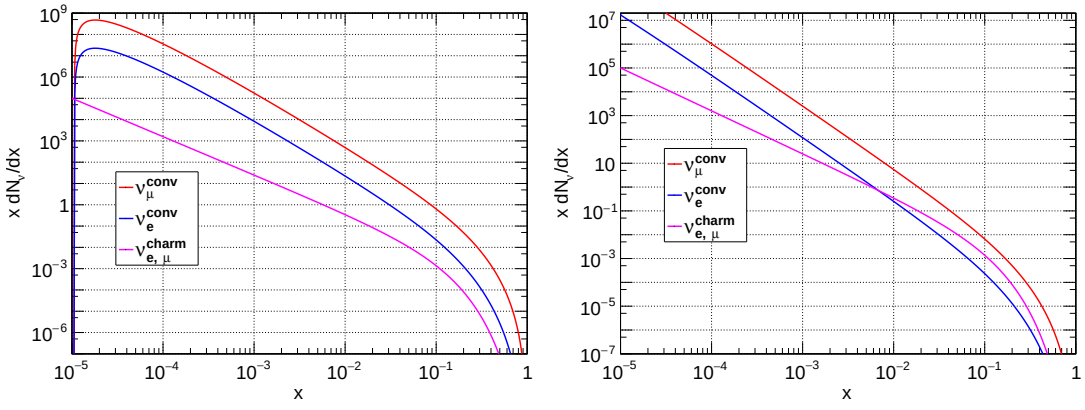

Figure 2.5: Yields of the atmospheric neutrino flux in a proton shower of energy $E_p = 10^4$ GeV (left) and $E_p = 10^6$ GeV (right).

flux Φ_N and deduce atmospheric neutrino flux[1]:

$$\Phi_i(E) = \int_{\frac{E}{10^8\,\mathrm{GeV}}}^{1} \mathrm{d}x\, x^{-1}\, f_{p\nu_i}(x, E/x)\; \Phi_{\mathrm{N}}(E/x)\,, \tag{2.19}$$

where we have taken CR primaries of energy up to 10^8 GeV.

For the CRs of energy above the ankle we have considered several compositions, which can give us an idea of how uncertain the atmospheric neutrino is at higher energies. Namely, we have assumed that the total flux in Eq. (2.4) is composed by only protons, only iron, or that both protons and helium fluxes are continuous at the knee. Fig. 2.6a shows the atmospheric flux of neutrinos at $\theta = 45^\circ$ for the three different hypothesis. We see that the low energy region is not affected by the choice of composition above E_{knee}, but that a flux with only proton primaries would give 10 times more neutrinos than iron primaries at 10^6 GeV. However, in the energy region up to 10 TeV the difference is negligible, so in the rest of this thesis we will just assume continuity of the proton and helium fluxes at E_{knee} (the black line in Fig. 2.6a). All the fluxes shown in Fig. 2.6 are multiplied by the angular size of the Sun, $\Delta\Omega_{\mathrm{Sun}}$.

Fig. 2.6b shows the contribution of the ν_μ and the ν_e flavours to the total neutrino flux, whereas Fig. 2.6c reveals the conventional or charm origin of the neutrinos at different energies. The conventional component dominates at low energies, specially for the muon flavor. It should be noticed, however, that the production of forward (non-perturbative) charm in hadronic collisions introduces a large uncertainty that could easily multiply by a factor 3 the charm contribution at 10^6 GeV [59].

The dependence of the flux with the zenith angle can be expressed as a function of the angle of the line of sight at $h = 30$ km [55, 60],

$$\theta^*(\theta) = \arctan\left(\frac{R_T \sin\theta}{\sqrt{R_T^2\cos^2\theta + (2R_T + h)h}}\right). \tag{2.20}$$

We fit [61]

$$\Phi_{\nu_i}(E,\theta) = \Phi_{\nu_i}(E)\,\frac{\left(\frac{E_c^i}{1.7E}\right)^{a_i} + \cos\theta^*(\pi/4)}{\left(\frac{E_c^i}{1.7E}\right)^{a_i} + \cos\theta^*(\theta)}, \tag{2.21}$$

with $a_e = 0.21$, $a_\mu = 0.6$, $E_c^\mu = 300\,\mathrm{GeV}$ and $E_c^e = 1.27\times10^{-3}\,\mathrm{GeV}$. In Fig. 2.6d we plot the total atmospheric neutrino flux for 3 different zenith inclinations.

[1]Since we do not separate neutrinos from antineutrinos of a given flavour, we will not distinguish between the proton and neutron yields.

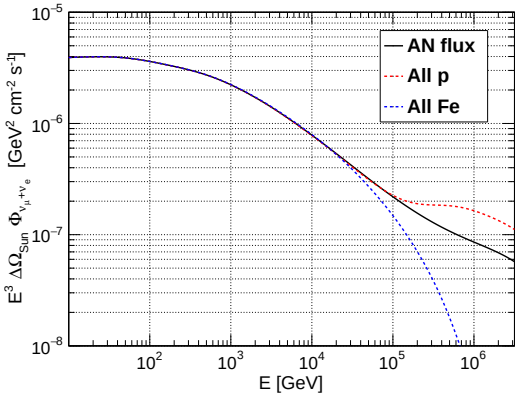

(a) Atmospheric neutrino flux for a continuous all-nucleon flux at the knee, a pure proton flux or a pure iron flux above the knee.

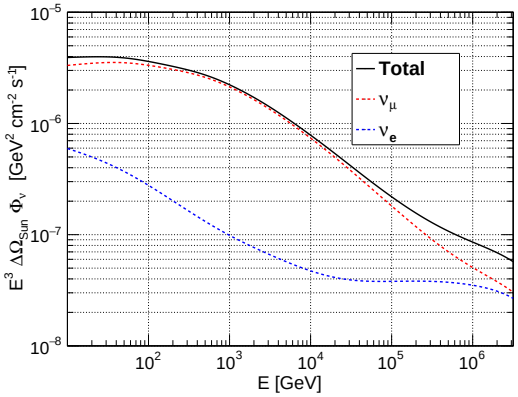

(b) Atmospheric neutrino flux for $\theta_z = 45°$.

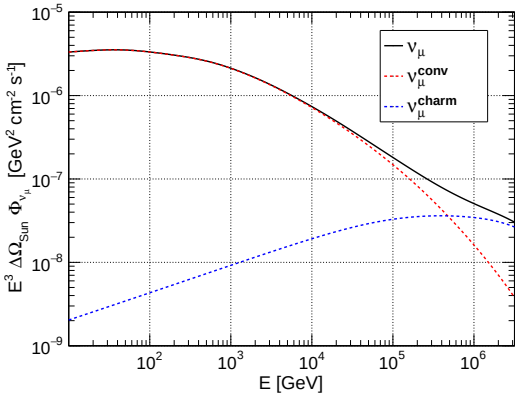

(c) Components of the $\nu_\mu^{\text{conv}} + \nu_\mu^{\text{charm}}$ atmospheric flux for $\theta = 45°$.

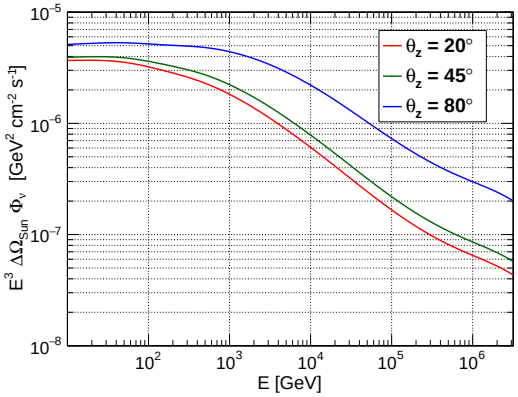

(d) Atmospheric neutrino flux at different zenith angles.

Figure 2.6: Atmospheric neutrino flux.

2.4 High energy solar neutrino flux

The second source of high-energy neutrinos that define a background in DM searches is the Sun itself. If a CR reaches the Sun it will collide with a nucleus of hydrogen or He and produce secondary particles. As we will see, there are several important differences between the solar and the atmospheric CR showers. If one neglects magnetic effects (which is a good approximation at CR energies above 50 TeV), CRs may enter the solar surface vertically from the side of the Sun not facing the Earth, shower there and produce neutrinos that can cross the Sun and emerge on the other side, possibly reaching the Earth. If one includes magnetic effect (CRs below 50 TeV) then the trajectory of the primary and secondary particles are very far from being straight lines, and the emission of neutrinos may be directed in any direction. This defines an *albedo* flux of secondaries emitted isotropically from the surface of the Sun [62]. Neutrinos, gammas and neutrons, being neutral particles, may then reach the Earth directly from there. In this chapter we use data from HAWC and Fermi-LAT and solve cascade equations to deduce these solar fluxes.

Solar model

We will assume the solar model proposed in [63] and [64]. Although to calculate the flux of neutrinos we will just need a few elements, namely, the density profile and

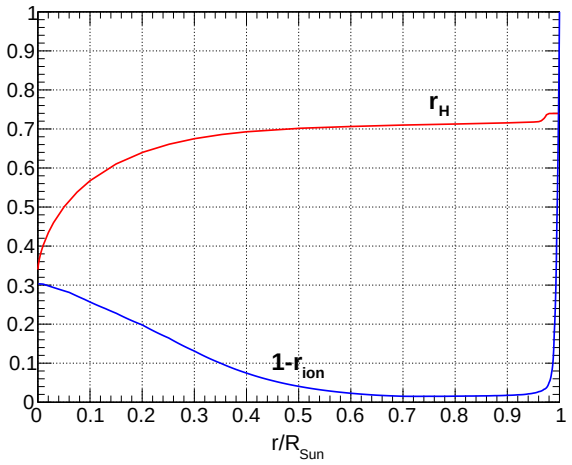

Figure 2.7: Fraction of the solar mass for hydrogen, r_{H}, and fraction of non-ionised matter.

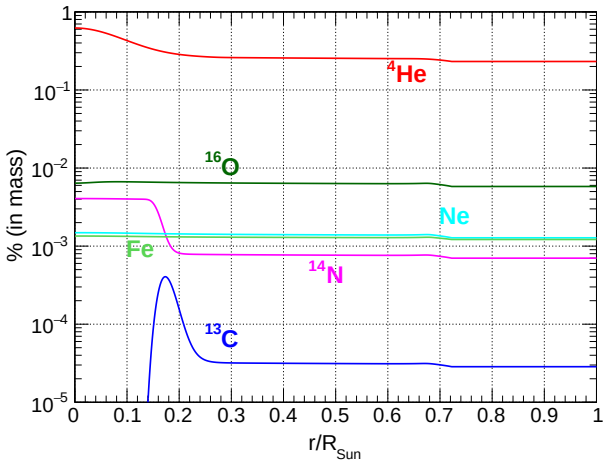

Figure 2.8: Composition of the Sun in fraction of mass. The hydrogen fraction is not shown in this plot.

the fraction of ionised matter, we will provide some details (like the frequency of the different solar nuclei) that will be necessary to calculate the capture rate of DM later on.

Fig. 2.7 shows the relative abundance of hydrogen as a function of the solar radius, as well as the fraction of non-ionised matter $(1-r_{\rm ion})$, which is necessary to determine the muon energy loss by ionization and radiative processes. These energy losses will be lower than in the Earth because nuclei are lighter and because a fraction of them are already ionised. In particular, the energy loss of muons in the Sun is given by Eq. (1.8).

Fig. 2.8 shows the relative abundance (in mass) of some of the more relevant elements in the so-called AGSS09 model [65]. In our analysis of the capture rate of DM by the Sun we will include ^{4}He, ^{14}N, ^{16}O, Ne and Fe together with ^{1}H, which is shown in Fig. 2.7, and we will neglect other less abundant nuclei.

As mentioned, a key parameter in the development of solar showers is the density profile, that can be found together with the temperature in Fig. 2.9. We see that the solar medium is, during many kilometres, much thinner than the air in the Earth's atmosphere. The photosphere, extending up to 500 km above the Sun's optical surface, has a density between 3×10^{-9} and 2×10^{-7} g/cm^3. A CR that crosses it vertically will face a total depth (column density) of just 2.7 g/cm^2, whereas if the CR enters with an impact parameter $r = 0.9$ (in $R_\odot$ units) the total depth of the

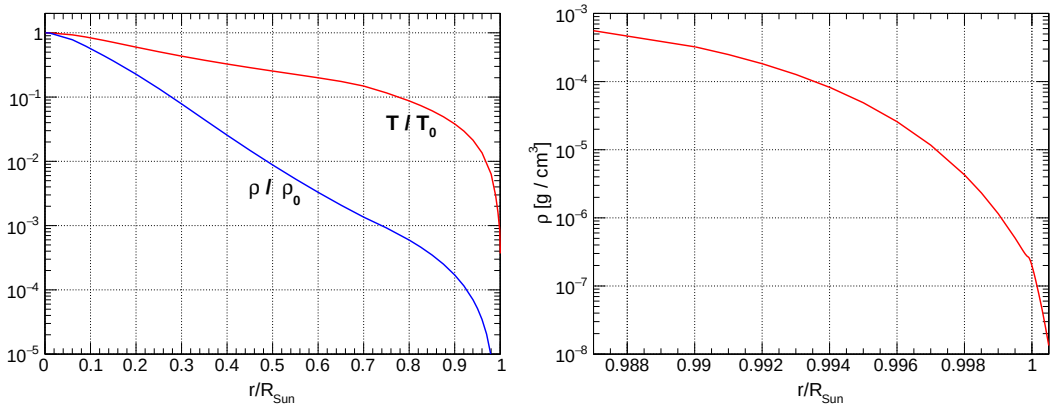

Figure 2.9: Left: Temperature and density in the Sun as a function of the normalised radius, r/R_{Sun}. Both are normalised to their values in the core, $T_0 = 1.54 \times 10^7$ K and $\rho_0 = 148.9$ g/cm^3. Right: Density in the vicinity of the solar surface.

photosphere increases to 6.2 g/cm^2. Moreover, when the CR goes deeper it will not find a sharp change in the Sun's density. For example, it takes 1500 km to cross 100 g/cm^2 from $r = 0$ or up to 2600 km from $r = 0.9$, where r is the normalised impact parameter of the CR entering the Sun ($r = 0$ corresponds to a CR entering the Sun radially and $r = 1$ to a CR just skimming its surface). The decay length of a 10 TeV charged pion is 557 km, so most mesons and even muons produced there will have plenty of time to decay and give high-energy neutrinos.

The shadow of the Sun

If we point with a detector of CRs to the Sun, we will observe its shadow: the CR shadow of the Sun [66, 67, 68]. Let's suppose there were no solar magnetism and CRs follow straight lines. Then the trajectories aiming to the Earth but absorbed by the Sun would define a black disk of radius 0.26°, the angular size of the Sun as seen from the Earth. Indeed, this is what we will see at very high energies, when the deflection of CRs by the solar magnetic field is negligible, but not at lower energies. CRs of $E < 100$ TeV are very much affected by a magnetic field that is very involved. First of all, it has a radial component (open lines that define the Parker interplanetary field [69, 70]) that grows like $1/R^2$ as CRs approach the surface. This gradient may induce a magnetic mirror effect: CRs going towards the Sun tend to bounce back. In addition, the solar wind induces convection, *i.e.*, CRs are propagating in a

plasma that moves away from the Sun and makes it more difficult to reach the surface. Finally, closer to the Sun the magnetic turbulence increases and there appears a type of field lines that start and end on the solar surface. Although the absorption of CRs by the Sun and the emission of high energy particles that it induces was already discussed 30 years ago [71], a precise calculation from first principles is plagued by the uncertainties introduced by the solar magnetism [72]. Hopefully, we can get the *right* result with no need to solve these details, just by using the data on its CR shadow together with Liouville's theorem.

The data is provided by the HAWC experiment [73], that has studied the energy-dependence of the CR shadow during a solar maximum (years 2013–2014). The shadow appears at 2 TeV; it is not a black disk of $\theta_\odot = 0.26^\circ$ but a deficit that HAWC fits with

$$\mathrm{d}(\theta) = -A \exp\left(-\frac{\theta^2}{2\sigma^2}\right) , \tag{2.22}$$

providing the parameters A and σ at 3 different energies. By integrating it we find that at 2 TeV it accounts for a 6% of a black disk, the deficit grows to a 27% at 8 TeV, and at 50 TeV it becomes a 100% deficit, *i.e.*, a complete solar black disk diluted in a larger circle or 2° radius.

HAWC's data suggest a simple interpretation based on Liouville's theorem. The theorem implies that when the isotropic CR flux crosses the solar magnetic field, it stays isotropic, and that the only possible effect of the Sun is to interrupt some of the trajectories that were aiming to the Earth. As we illustrate in Fig. 2.10, the solar magnetic field deflects some of the trajectories directed to the Earth, but other trajectories will now reach us and the net effect should be zero: an isotropic

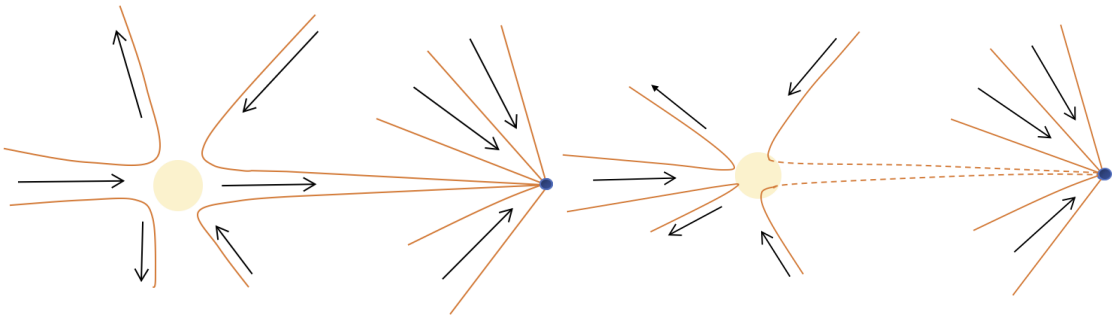

Figure 2.10: Schematic CR trajectories in the vicinity of the Sun. As the energy grows trajectories that were supposed to reach the Earth cross a larger depth of solar matter, increasing the probability that CRs are absorbed and define a shadow. The solid lines are the trajectories of CRs, while the dashed lines are the CR shadow.

flux crossing a static magnetic lens, including a mirror, will stay isotropic, and the only possible effect is to create a shadow. At low energies HAWC sees no shadow, meaning that a negligible fraction of the CR flux reaches the solar surface. At higher energies, however, CRs that were supposed to reach the detector hit before the Sun and are absorbed (Fig. 2.10-right). Therefore, studying the shadow we may deduce the average depth of solar matter crossed by CR's of different energy in their way to the Earth.

If a CR proton crosses an average depth of $\Delta X_{\rm H}(E)$ the probability that it is absorbed is

$$p^{\rm H}_{\rm abs} = 1 - \exp\left(-\frac{\Delta X_{\rm H}}{\lambda^{\rm H}_{\rm int}}\right) . \tag{2.23}$$

To explain the data we take

$$\frac{\Delta X_{\rm H}}{\lambda^{\rm H}_{\rm int}} = b_H\, E^{1.1} , \tag{2.24}$$

with E in GeV and a time dependent parameter b_H that changes from 1.6×10^{-5} during a solar maximum to 4.8×10^{-5} during a minimum. Since the trajectory of a CR only depends on its rigidity, He nuclei of twice the energy cross the same average depth and

$$b_{\rm He} = \frac{b_{\rm H}}{2^{1.1}} \frac{\sigma_{\rm He}(E)}{\sigma_H(E/2)} . \tag{2.25}$$

Eq. (2.24) is then the first and key hypothesis in this framework. It implies the absorption of CR primaries given in Fig. 2.11-left, where we have considered the CR composition with only proton and He nuclei discussed in Sec. §2.1. This absorption determines whether the CR shadow that we see at different energies is partial or complete. At low energies CRs are unable to reach the solar surface: the depth of solar matter that they cross is small, they are not absorbed and we see no shadow. At very high energies CRs that were supposed to reach the Earth find before a large column density of solar matter and are absorbed, thus we see a complete shadow. Our choice for the 1.1 spectral index and for the value of b_H during an active phase of the Sun is based only on HAWCs observations, whereas the value of b_H during a quiet Sun provides our best fit for the Fermi-LAT data (described in the next subsection).

Cascade equations in the Sun

The next step is to model the showering of these absorbed fluxes. A numerical simulation of CR trajectories shows that at TeV energies only trajectories very aligned with the open field lines are able to reach the Sun's surface. Once there, CRs will

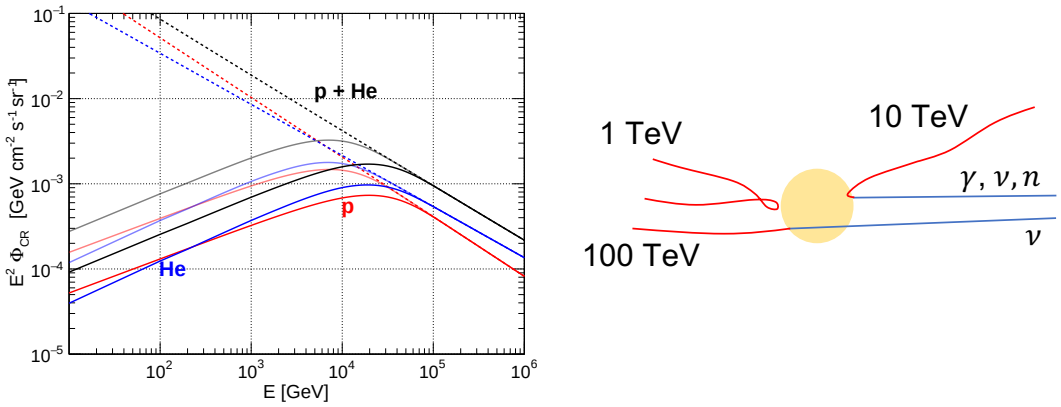

Figure 2.11: Left: absorbed proton and He fluxes during a solar maximum (thick) and a solar minimum (thin). The dashed lines are the total fluxes. Right: Typical CR trajectories at different energies. When the magnetic field is weaker CRs are more likely to reach the surface of the Sun.

shower; some of the secondaries will be emitted inwards, towards the Sun, but others will be emitted outwards and may eventually reach the Earth. The probability that a secondary particle contributes to the solar albedo flux will depend on how deep it is produced and in which direction it is emitted.

We assume that secondaries produced by a parent of energy E above some critical energy $E_{\rm c} = 5$ TeV will most likely be emitted towards the Sun, whereas lower energy primaries will exit in a random direction:[1]

$$p_{\rm out} = \frac{1}{2}\, e^{-(E/E_{\rm c})^2}. \tag{2.26}$$

Accordingly, we also assume that charged particles of energy below E_c are unable to keep penetrating the Sun: they are trapped by closed magnetic lines at the depth where they are produced and shower horizontally. Eq. (2.26) is then the second basic hypothesis in our framework; the precise value of E_c has been chosen to reproduce the drop in the gamma ray flux observed by Fermi-LAT at energies above 200 GeV (see also [74]).

Under the two assumptions expressed in Eqs. (2.24) and (2.26), we use the cascade equations described in Section §2.2 adapted to the Sun. For example, the interaction lengths within the Sun are deduced based on the total (inelastic) cross

[1]Notice that $E_{\rm c}$ is a factor of 2 larger when the parent particle is a He nucleus.

sections of protons, pions, and kaons colliding with hydrogen and helium nuclei, provided by SYBILL. In particular:

$$\lambda_i^{\rm int} = \frac{m_p}{r_H\,\sigma_{ip} + \frac{1-r_h}{4}\,\sigma_{i\rm He}}. \tag{2.27}$$

As mentioned before, the key difference with the usual showers in the Earth's atmosphere is due to the thin environment where these solar showers develop: TeV pions and muons decay before they lose energy, defining a neutrino flux well above the atmospheric one. In addition to the albedo flux, for neutrinos we must add the ones produced in the opposite side of the Sun [75, 76, 77]. Our results for the signal in the different channels are the following.

Gamma rays

Fig. 2.12 shows the flux of gamma rays at $E > 10$ GeV obtained by our model together with the Fermi-LAT data. Here, $\Delta\Omega_{\rm SD}$ is the angular size of the solar disk from the Earth. The normalization of the red line is a direct consequence of the value of b_H dictated by HAWC's data on the CR shadow during a solar maximum (thick lines in Fig. 2.11-left), whereas the blue line is controlled by the value of b_H chosen for a quiet Sun, which implies the CR shadow given by the thin lines in Figure 2.11-left.

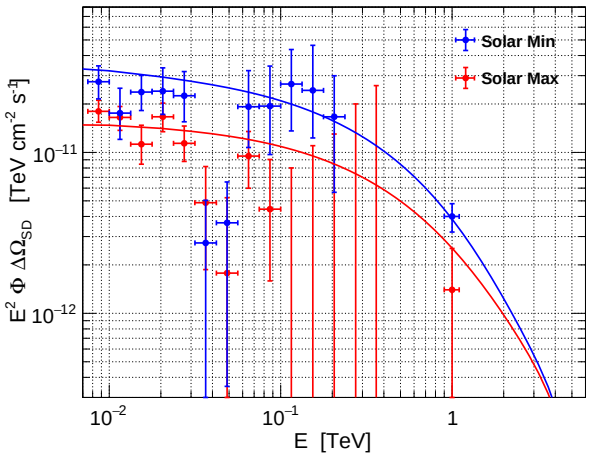

Figure 2.12: Gamma ray flux from the solar disk (data at $E \leq 200$ GeV from Fermi-LAT [78] and at 1 TeV from HAWC [79]). The flux is lower during the solar maximum since the magnetic field is stronger and, consequently, less CRs reach the surface of the Sun.

The value $E_c = 5$ TeV (versus 3–6 TeV in our previous analysis in [61]) has been tuned to obtain a better fit of the very recent HAWC observation at 1 TeV [79].

The spectrum of gamma rays exhibits two main features. At low energies it is reduced because primary CRs do not reach the Sun; notice that during a solar minimum it is easier for CRs to reach the solar surface, implying a more complete shadow and a larger gamma ray flux. At higher energies the gamma flux is reduced as well, but because of a different reason: all CRs reach the surface in their way to the Earth through the solar magnetic field and shower there, but most photons are emitted towards the Sun. Although the set up does not provide a reason for the possible *dip* at 40 GeV [78, 80], the 400–800 photons per squared metre and year that we obtain seem an acceptable fit of the data.

Neutrons, CR shadow and muon shadow

Our analysis implies an average of 240 neutrons of energy above 10 GeV reaching the Earth from the solar disk per squared metre and year, with the flux during a solar minimum a factor of 2 larger than during an active phase of the Sun. Most of these neutrons come from the spallation of He nuclei (see Fig. 2.13-left), resulting in a very characteristic spectrum that peaks at 1 TeV. The flux is interesting because neutrons are unstable and they can reach us from the Sun but not from outside the

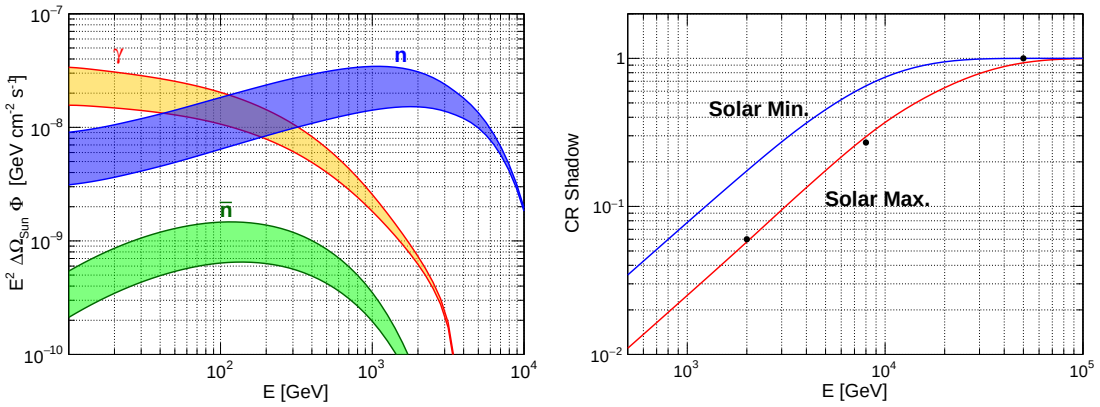

Figure 2.13: Left: Gamma and neutron fluxes. The upper lines in the bands are the fluxes during solar minimums, while the lower lines are the fluxes during solar maximums. Right: Integrated CR shadow from the solar disk; the dots correspond to the HAWC observations [73].

Solar System. In a satellite experiment the background to this solar flux would be the albedo flux from CRs entering the atmosphere, which seems easily avoidable. Unfortunately, space observatories do not carry hadronic calorimeters and are thus unable to detect neutrons.

The solar neutron flux, in turn, has another effect as it enters the atmosphere: it *reduces* the CR shadow of the Sun measured by HAWC. In Figure 2.13-right we give the total shadow (fraction of CRs absorbed by the Sun minus the relative number of neutrons reaching the Earth) predicted by our framework together with HAWC's data, which was obtained near a solar maximum.

In addition to the CR shadow and the gamma and neutron signals, another interesting channel observable at neutrino telescopes (already detected at ANTARES [67], IceCube [81, 82] and KM3NeT [68]) is the muon shadow of the Sun when it is above the horizon: down-going muons pointing to the solar disk. These muons are produced when both the partial shadow of the Sun and these solar neutrons shower in the atmosphere. In Figure 2.14 we plot our results as a function of the muon energy (left) or the slant depth at the point of entry in the telescope (right).

The plot for the muon shadow of the Sun at different slant depths is specially revealing. It compares the number of tracks from the solar disk (smeared into a larger angular region) and from a *fake* Sun at the same zenith inclination. To observe it in a telescope, one should bin the slant depth of the muon tracks when they enter the detector and then determine the deficit (integrated to the whole angular region)

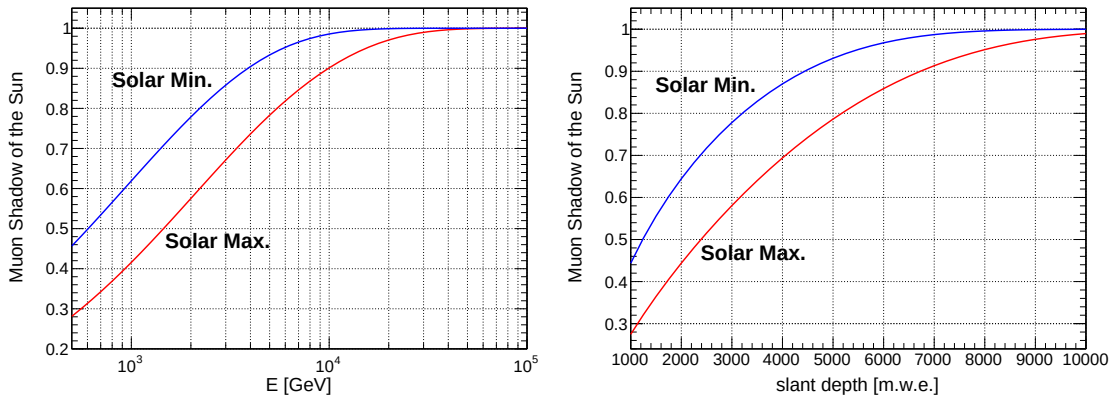

Figure 2.14: Muon shadow of the Sun at different muon energies (left) or slant depths (right).

relative to the fake Sun, finding the fraction of a black disk of $r_\odot = 0.26^\circ$ that it represents. In IceCube [83] the Sun is always very low in the horizon, implying that most muon tracks arrive after crossing a large slant depth and had to be very energetic. As a consequence, IceCube should see a more complete muon shadow than, for example, KM3NeT [84]. This second telescope will be able to access the Sun more vertically and thus from smaller slant depths (down to 3500 m.w.e.), which could establish a more clear energy dependence of this muon shadow. In any case, the data published by IceCube [82] exhibits two qualitative features that are fully consistent with our framework: a more complete shadow at higher energies[1] and a more complete shadow during a quiet Sun.

Neutrinos from the solar disk

This final flux from solar CR showers is an irreducible background in indirect DM searches. The flux reaching a neutrino telescope includes three different components:

i. Neutrinos produced in the Earth's atmosphere by the partial CR shadow of the Sun. At CR energies above 50 TeV the shadow is complete and this component vanishes, but at lower energies the shadow disappears and this component should coincide with the atmospheric ν flux.

ii. Neutrinos produced in the atmosphere by the solar neutrons reaching the Earth.

iii. The neutrinos produced in the solar surface, both the albedo flux and the flux from the opposite side that reaches the Earth after crossing the Sun.

The first two components were first considered in [61]. As for the third one, several groups [75, 76, 77] have obtained the neutrino flux produced by CRs unaffected by the solar magnetic field and showering in the opposite side of the Sun (see Fig. 2.11). Their results tend to be larger than ours at energies $E < 500$ GeV (in our set up low-energy CRs do not reach the Sun), a 30% smaller at $E \approx 1$ TeV (our albedo flux is not partially absorbed by the Sun in its way to the Earth) and similar at $E > 10$ TeV (at high energies neutrinos are produced always inwards). In Figure 2.15-left we plot the flux of neutrinos produced in the solar surface together with the albedo flux of gammas and neutrons for comparison. We see that at low energies neutrinos more than *double* the number of gammas, whereas at $E > 5$ TeV all albedo fluxes vanish but we still get the neutrinos produced in the opposite side of the Sun.

[1] Notice that they give the results in terms of the primary CR energy, which is typically 10 times larger than the energy of the muons in our Figure 2.14.

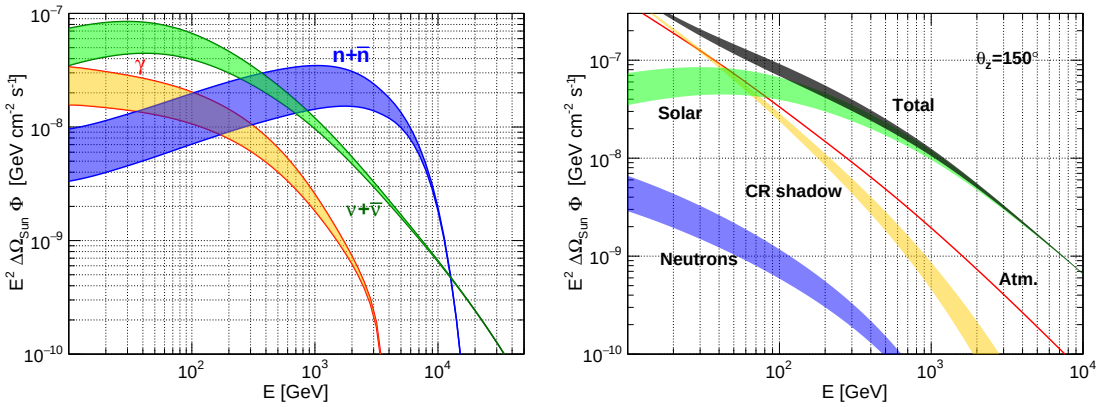

Figure 2.15: Left: solar neutrino flux with gammas and neutrons for comparison. Right: components defining the neutrino flux observed in a telescope from the solar disk at $\theta_z = 150°$ and atmospheric background at the same zenith inclination. For both plots, the upper lines in the bands are the fluxes during solar minimums; while the lower lines are the fluxes during solar maximums.

In Figure 2.15-right we plot the three neutrino components when the Sun is at $\theta_z = 150°$, *i.e.*, 60° below the horizon (notice that the fluxes produced by the partial shadow and by the solar neutrons depend on the zenith angle), together with the atmospheric background. The bands express the variation during a solar cycle; the solar and neutron components are larger during a quiet Sun, whereas the ν component from the partial shadow is larger during a solar maximum. These variations tend to cancel and the total neutrino flux (the black band in the plot) changes little during the 11 year solar cycle (the maximum variation is a 25% at 200 GeV).

An important effect to take into account is flavor oscillations. As shown in [85], matter effects are suppressed when averaged over the production region and over the ν and $\bar{\nu}$ components, and the final effect is dominated by oscillations in vacuum between the Sun and the Earth. In particular, muon and electron neutrinos will experience multiple oscillations into the ν_τ flavor at energies $E < 70$ GeV and $E < 2$ TeV, respectively. The final result is a flux of neutrinos from CR showers in the sun with an almost identical frequency of the three neutrino flavors [31].

We see that the total neutrino flux from the solar disk is well above the atmospheric background at $E > 100$ GeV. In Figure 2.16-left we compare the two fluxes when the Sun is 60° or 30° below the horizon (*i.e.*, $\theta_z = 150°$ and 120°, respectively). We see that the neutrino flux from the solar disk changes little with the zenith angle, whereas

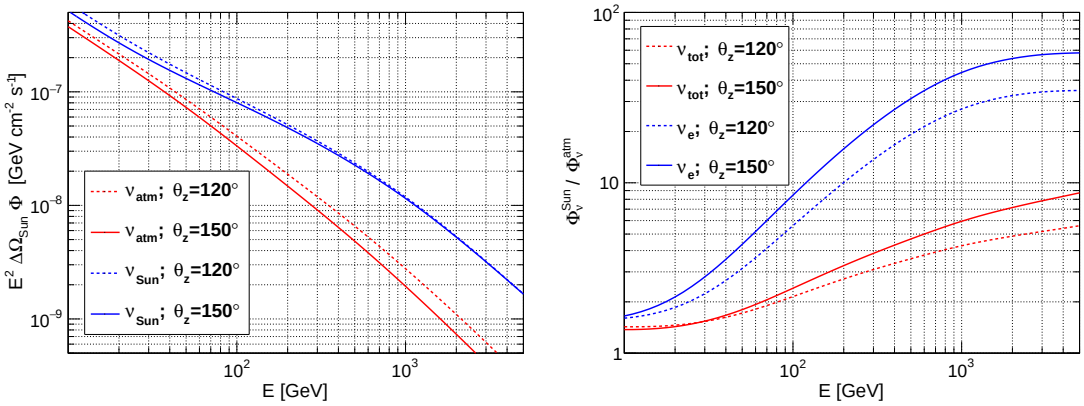

Figure 2.16: Left: Total neutrino flux from the solar disk versus atmospheric background for the Sun in two different zenith inclinations. Right: Signal to background ratio for ν_e and for the sum of all flavors .

the atmospheric background from a fake Sun at the same inclination is significantly larger when the Sun is near the horizon. In Figure 2.16-right we plot the ratio between both neutrino fluxes. Since the neutrinos produced in the Sun reach the Earth with the same frequency for the three flavors, the ratio is obviously much larger for ν_e than for ν_μ, and it grows with the energy and with the zenith inclination.

2.5 Discussion

TeV CRs induce an indirect solar emission discussed more than 30 years ago and just recently detected in gamma rays. In this chapter we have discussed a set up [31, 61, 86] that uses the energy dependence of the CR shadow of the Sun at HAWC to define very definite fluxes of gammas, neutrons and neutrinos. The set up is very simple, it is based on Eq. (2.24), that describes the average depth of solar matter crossed by protons at different energies, and in Eq. (2.26), that estimates the probability that a secondary particle is emitted inwards or outwards depending on the energy of the parent particle. Our framework explains the peculiar spectrum of solar gammas observed at Fermi-LAT's: low energy CRs do not contribute to the albedo flux as they do not reach the solar surface, whereas high energy CRs reach the Sun, but the secondary gammas are emitted mostly inwards and never reach the Earth. It also explains the TeV gamma flux recently observed at HAWC.

The framework could be confirmed if HAWC completed their analysis of the shadow to the full solar cycle or if KM3NeT and IceCube established a clear slant-depth dependence in the muon shadow of the Sun. Of course, new channels and a higher precision in the channels already observed would also test it. The framework may also have implications on the data (at much lower energies) provided by the IS⊙IS experiment [87, 88] at the Parker Solar Probe. It seems clear that the combined analysis of the five different signals discussed here would draw a more complete picture of the solar magnetism and of the propagation of CRs near the surface.

Most important for our objective of indirect DM searches with neutrino telescopes [89, 90, 91, 92, 93] is the consistency of the data in several channels that gives us confidence in the estimate of this background. We have shown that the neutrino fluxes reaching a telescope from the solar disk include three components: *(i)* the solar emission from both sides of the Sun, *(ii)* neutrinos produced when the partial CR shadow of the Sun enters the atmosphere, and *(iii)* neutrinos produced also in the atmosphere by the albedo flux of solar neutrons.

In the Appendix A we provide fits for these components, giving their explicit dependence on the zenith angle and the period of the 11 year solar cycle. The uncertainty in the fluxes is mainly correlated with the uncertainty in HAWC's data on the CR shadow of the Sun, and we estimate it at the 30% level. One should keep in mind, however, that the solar magnetism is not stable at all; if we quantify the activity in terms of the number Sunspots, the one year periods of solar activity present fluctuations of order 50%, which could be a fair estimate of the total uncertainty in the annual fluxes that we obtain.

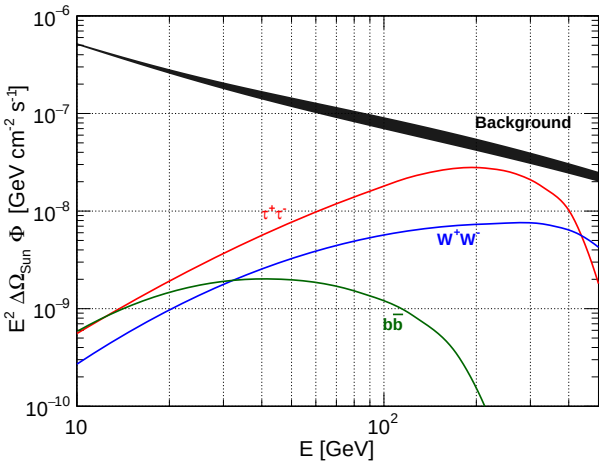

Figure 2.17: Expected signal from a WIMP with mass $m_\chi = 500$ GeV assuming a 100% annihilation BR in each case.

The neutrinos produced in the solar surface that we have obtained define a floor in DM searches to be compared with the neutrino signal in particular DM models (see next chapter). To illustrate at this point the relevance of this floor, we would like to show the results that we obtain [61] for the simple DM models that are usually considered in experimental searches. If we take the maximum spin independent elastic cross section consistent with the bounds from XENON1T [94], and we assume a 500 GeV DM that annihilates with a 100% branching ratio into $\tau^+\tau^-$, $b\bar{b}$ or W^+W^-, in an stationary regime where the rate of DM annihilations is half the capture rate the expected signal from the Sun is already below this background (see Fig. 2.17). Therefore, a precise characterization of the ν fluxes from the solar disk induced by CRs is essential both to decide the optimal detection strategy and to establish the reach of indirect DM searches at each neutrino telescope.

We conclude that the high energy emission of the Sun is a paradigmatic example of multimessenger physics accessible through different channels. Its exploration in the near future will provide a more complete picture of the solar magnetism, of the propagation of CRs, and of the flux of cosmic neutrinos reaching the Earth.

3

Monochromatic neutrinos from dark matter in the Sun

Energy is liberated matter, matter is energy waiting to happen.

Bill Bryson.

In this section, we propose a simple model for DM that is consistent with the bounds from direct searches, that provides the observed relic abundance and, most remarkable, that may also imply an observable signal in neutrino telescopes from its annihilation in the Sun. First we detail how the same elastic scattering that is probed in direct-search experiments also determines the capture rate of DM by the Sun. We show, in particular, that in the usual models where the interaction of a WIMP with the visible matter is spin-independent, the maximum signal that can be expected in neutrino telescopes is below the CR background discussed in the previous section. Then we define a model where the mediator of the DM interactions with the visible matter is the Higgs boson. It is an effective model that includes dimension-5 and 6 operators (we explain how these operators may be generated) and adds to the SM particles just a stable Majorana singlet χ and a heavy Dirac singlet N. The Yukawa interaction of N to the Higgs and the lepton doublets implies then an annihilation channel $\chi\chi \to h \to \nu\bar{N}$ giving monochromatic neutrinos. Finally, we obtain the neutrino signal from the Sun produced by this WIMP. We think that this model is a canonical example of DM scenario that can be probed in a complementary way in direct, indirect and collider experiments.

3.1 Capture of dark matter

As the Sun moves across the galaxy, it faces a wind of DM particles. Some of these particles may collide with the nuclei present in the solar medium. After the collision, the DM particle may lose enough energy so that its velocity is lower than the escape velocity of the Sun at that point:

$$v_{\rm esc}^2(r) = 2\int_r^\infty \frac{G\,M(r')}{r'^2}\,{\rm d}r', \tag{3.1}$$

with

$$M(r') = \begin{cases} 4\pi\int_0^{r'} r^2\rho_{\rm Sun}(r){\rm d}r & \text{if} \quad r' < R_{\rm Sun}\,, \\ \\ M_{\rm Sun} & \text{if} \quad r' \geq R_{\rm Sun}\,, \end{cases} \tag{3.2}$$

where G is the gravitational constant, $\rho_{\rm Sun}$ is the density of the Sun, $M_{\rm Sun}$ the total mass of the Sun and $R_{\rm Sun}$ its radius. In that case, the DM particle is trapped by the gravitational field of the star: it will keep colliding until, eventually, it falls inside and stays there, with a kinetic energy similar to the solar temperature. Fig. 3.1 shows the scape velocity inside the Sun as a function of the normalised radius.

Therefore, to obtain the rate of DM capture by the Sun it is necessary to characterise both the velocity distribution of the DM particles before (and after) they reach the Sun and the elastic collisions with the nuclei that they experience there.

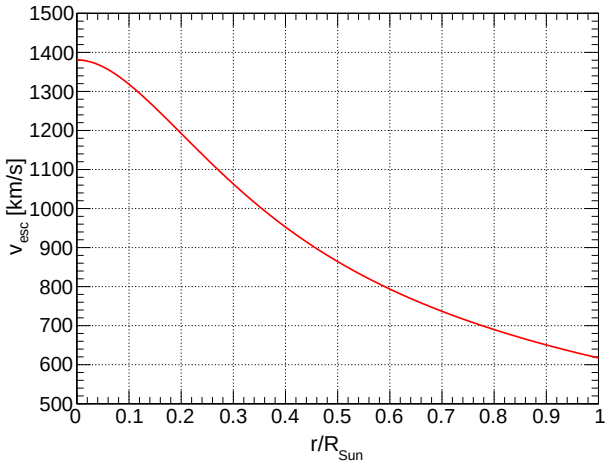

Figure 3.1: Escape velocity in the Sun.

Dark matter velocity distribution

The Sun is moving around the centre of our galaxy with a velocity $v_0 \approx 230$ km/s. In contrast, the DM in the same region of the galaxy is moving in random directions, with a velocity that is similar in modulus (otherwise it would fall towards the center of the galaxy) but zero when it is averaged over all directions. We will assume the velocity distribution of DM in the vicinity of the Sun given by the two-component model known as Standard Halo Model ++ (SHM++) [95].

The first of these components corresponds to the simple SHM proposed in 1939 [96], with and spherical and isotropic structure deduced from observation of metal-poor stars moving out of the galactic plane. This component, $f_R(\vec{u})$, is expressed as

$$f_R(\vec{u}) = \frac{1}{(2\pi\sigma_u^2)^{3/2}\, N_{\rm R}} \exp\left(-\frac{u^2}{2\sigma_u^2}\right) \Theta(\tilde{v}_{\rm esc} - u), \tag{3.3}$$

being $u = |\vec{u}|$, $\tilde{v}_{\rm esc}$ the escape velocity from the galaxy and $\sigma_u = v_0/\sqrt{2}$ with $v_0 = 230$ km/s the velocity of the Sun around the galaxy. The Heaviside function, Θ, ensures that the DM particles are trapped in the galaxy, whereas the factor

$$N_{\rm R} = \text{erf}\left(\frac{\tilde{v}_{\rm esc}}{\sqrt{2}\sigma_u}\right) - \sqrt{\frac{2}{\pi}}\frac{\tilde{v}_{\rm esc}}{\sigma_u} \exp\left(-\frac{\tilde{v}_{\rm esc}^2}{2\sigma_u^2}\right), \tag{3.4}$$

with erf the error function, normalises the distribution to 1.

The second component has been inferred from the observation of stars with high metallicity that form a population radially anisotropic with very eccentric orbits. It is believed that they were trapped by the Milky Way after its collision with another galaxy, known as the Sausage Galaxy. This *sausage component* [95] is given by:

$$f_S(\vec{u}) = \frac{1}{(2\pi)^{3/2}\sigma_r\sigma_\theta\, N_{\rm S}} \exp\left(-\frac{u_r^2}{2\sigma_r^2} - \frac{u_\phi^2}{2\sigma_\phi^2} - \frac{u_\theta^2}{2\sigma_\theta^2}\right) \Theta(\tilde{v}_{\rm esc} - u), \tag{3.5}$$

with $\theta = 0$ orthogonal to the galactic plane,

$$N_{\rm S} = \text{erf}\left(\frac{\tilde{v}_{\rm esc}}{\sqrt{2}\sigma_r}\right) - \exp\left(-\frac{\tilde{v}_{\rm esc}^2}{2\sigma_\theta^2}\right) \text{erfi}\left(\frac{\tilde{v}_{\rm esc}^2}{2\sigma_r^2}\left(\frac{\beta}{1-\beta}\right)^{1/2}\right), \tag{3.6}$$

where erfi is the complex error function and

$$\sigma_r^2 = \frac{3v_0^2}{2(3-2\beta)}, \quad \sigma_\theta^2 = \sigma_\phi^2 = \frac{3v_0^2(1-\beta)}{2(3-2\beta)}. \tag{3.7}$$

The parameter β describes the anisotropy in the velocity of the DM particles assuming that it coincides with the one of the stars in the Sausage galaxy.

Local density of DM	ρ_{DM}	$0.55 \pm 0.17\,\mathrm{GeV/cm^3}$
Rotation velocity around the galaxy	v_0	233 ± 3 km/s
Escape velocity from the galaxy	$\tilde{v}_{\mathrm{esc}}$	528^{+24}_{-25} km/s
Sausage anisotropy	β	0.90 ± 0.05
Sausage mixing	η	0.2 ± 0.1

Table 3.1: Parameters used to characterise the Standard Halo Model (SHM++).

The final velocity distribution in the SHM++ model is then

$$f_T(\vec{u}) = \eta f_R(\vec{u}) + (1-\eta) f_S(\vec{u}), \tag{3.8}$$

where η expresses the contribution of the sausage component (see the value of all the parameters in Table 3.1). We can also obtain the distribution of u (the modulus of the DM velocity) by integrating over all directions:

$$f_T(u) = \int_{-1}^{1} \mathrm{d}\cos\theta \int_0^{2\pi} \mathrm{d}\phi\, f_T(\vec{u})\,. \tag{3.9}$$

Fig. 3.2 shows this distribution in the SHM++ and SHM models[1]. The drops at

[1]The parameters shown in Table 3.1 are slightly modified in the SHM model. In particular, the best fit in that case is obtained for $\rho_{DM} = 0.3\,\mathrm{GeV/cm^3}$, $v_0 = 220$ km/s and $\tilde{v}_{\mathrm{esc}} = 544$ km/s.

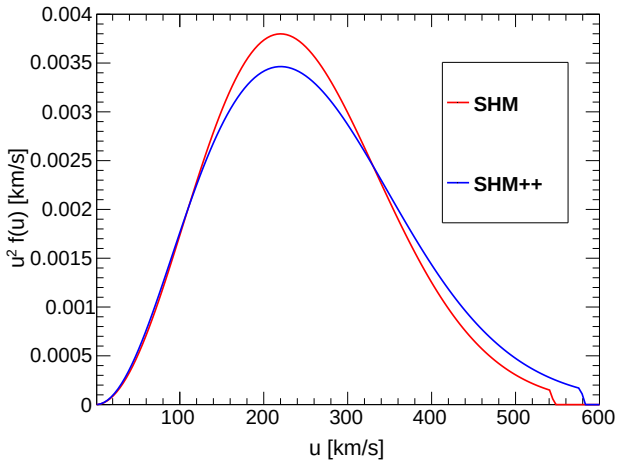

Figure 3.2: Distribution of DM velocity in the vicinity of the Sun in the galactic reference frame.

the end of the distributions indicate the maximum velocity of a DM particle in the vicinity of the Sun trapped in our galaxy.

The distributions given above are in the galactic reference frame, but to obtain the capture rate it will be convenient to express them in the rest frame of the Sun. With the shift $\vec{u} \to \vec{u} + \vec{v}_0$ the SHM component becomes:

$$f_R^{\rm Sun}(\vec{u}) = \frac{1}{N_{\rm R}} \exp\left[-\frac{u^2 + v_0^2 + 2u\, v_0 \cos\theta}{2\sigma_u^2}\right] \Theta\left(\tilde{v}_{\rm esc} - |\vec{u} + \vec{v}_0|^2\right) \tag{3.10}$$

where now the Heaviside function implies $u \in [0, v_0 + \tilde{v}_{\rm esc}]$. As for the sausage component, it can be written

$$\begin{aligned} f_S^{\rm Sun}(\vec{u}) = \frac{1}{N_S} \exp\left(-\frac{u^2 \sin^2\theta \cos^2\phi}{2\sigma_r^2}\right) \Theta\left(\tilde{v}_{\rm esc} - |\vec{u} + \vec{v}_0|^2\right) \times \\ \times \exp\left[-\frac{1}{2\sigma_\theta^2}\left(u^2 \sin^2\theta \sin^2\phi + u^2 \cos^2\theta + v_0^2 + 2v_0\, u \cos\theta\right)\right]. \end{aligned} \tag{3.11}$$

Integrating over all directions we obtain the distribution $f_T^{\rm Sun}(u)$ of DM velocities in the rest frame of the Sun given in Fig. 3.3. However, this is *not* the final distribution of DM velocity in collisions with solar nuclei, as one has to add the acceleration produced by the solar gravitational field. The velocity $\vec{u}$ of the DM particles in the vicinity of the Sun before they fall is changed to $\vec{w}(r)$, with

$$w(r) = \sqrt{u^2 + v_{\rm esc}(r)^2}. \tag{3.12}$$

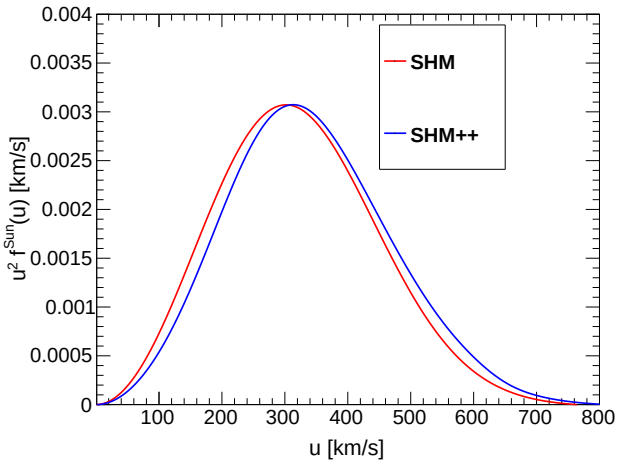

Figure 3.3: Distribution of DM velocity in the vicinity of the Sun in the Sun reference frame.

Kinematics of the collision with a nucleus at rest

Consider the elastic collision of a DM particle χ of mass m_χ and velocity w with a nucleus of mass m_A at rest. The energy lost by the projectile will be transferred as a recoil energy E_r to the nucleus. This kinematical variable can be related to the scattering angle θ in the center of mass frame:

$$E_r = \frac{m_\chi^2\, m_A\, \tilde{\gamma}^2}{m_A^2 + m_\chi^2 + 2\, m_A\, m_\chi\, \tilde{\gamma}}\, w^2(1-\cos\theta), \tag{3.13}$$

being $\tilde{\gamma} = 1/\sqrt{1-w^2}$. In the non-relativistic limit ($w \ll 1$), Eq. (3.13) becomes

$$E_r = \frac{E_{\max}}{2}(1-\cos\theta), \tag{3.14}$$

where the maximum energy lost by χ in the collision with the nucleus is

$$E_{\max} = \frac{2m_\chi^2\, m_A}{(m_A+m_\chi)^2}\, w^2. \tag{3.15}$$

As already mentioned, the distributions detailed in the previous section (see Fig. 3.3) provide the velocity $\vec{u}$ of DM particles in the vicinity of the Sun before they fall. The velocity w in the collision can be simply related to u using the scape velocity $v_{\rm esc}^2$ at the point where the collision takes place (see Eq. (3.12)).

Collisions with a moving nucleus

The temperature of the Sun is between $T \approx 0.5$ eV in the surface and $T \approx 1$ keV in the core. As a consequence, the nuclei present in the solar medium are not static but have a thermal velocity v_A. Assuming a Maxwell-Boltzmann distribution, their average kinetic energy is

$$\frac{1}{2} m_A v_A^2 = \frac{3}{2} T, \tag{3.16}$$

implying a velocity

$$\langle v_A \rangle = \sqrt{\frac{3T}{m_A}}. \tag{3.17}$$

This corresponds to $\langle v_A \rangle \approx 176$ km/s for a He nucleus at the solar core. Although this thermal velocity is usually neglected in the literature, we would like to estimate its effect on the capture rate of DM by the Sun.

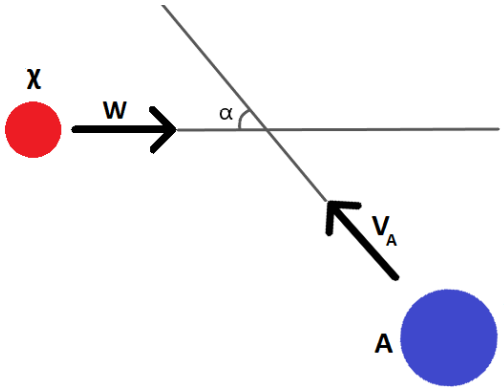

Figure 3.4: Scheme of the collision between a DM particle χ with velocity $\vec{w}$ with a moving nucleus with velocity v_A.

Let α be the angle before the collision between the DM particle with velocity $\vec{w} = w\hat{x}$ and a nucleus with velocity $\vec{v}_A$, both in the XY plane (see Fig. 3.4). The velocity of the centre of mass (CM) is given by

$$\vec{v}_x^{\,\mathrm{CM}} = \left(\frac{m_\chi\, w - m_A v_A \cos\alpha}{m_\chi + m_A}, \frac{m_A v_A \sin\alpha}{m_\chi + m_A} \right). \tag{3.18}$$

In the CM frame the DM velocity is just

$$\vec{w}_x^{\,\mathrm{CM}} = \left(\frac{m_A(w + v_A \cos\alpha)}{m_\chi + m_A}, -\frac{m_A\, v_A \sin\alpha}{m_\chi + m_A} \right), \tag{3.19}$$

with

$$w^{\mathrm{CM}} = \frac{m_A}{m_\chi + m_A} \sqrt{w^2 + v_A^2 + 2\, w\, v_A\, \cos\alpha}. \tag{3.20}$$

Then, the velocity of the DM particle after the collision in the center of mass frame is just

$$\vec{w}_f^{\,\mathrm{CM}} = w^{\mathrm{CM}} (\cos\theta, \cos\phi \sin\theta, \sin\phi \sin\theta), \tag{3.21}$$

whereas in the rest frame of the Sun this velocity is $\vec{w}_f = \vec{w}_f^{\,\mathrm{CM}} + \vec{v}^{\,\mathrm{CM}}$.

DM-nucleus cross section

We will consider the elastic collisions of a fermionic (spin 1/2) WIMP χ with matter in a non-relativistic regime. These collisions are relevant both in direct-search experiments and in the capture of DM particles by the Sun. Since the velocity of χ in these processes is of order $\beta \approx 0.001$, the typical exchanged momentum

($q^2 = 2\,m_A E_r$) will be below 1 MeV, much smaller than $\Lambda_{\rm QCD}$, and the nucleon can be taken as a point-like object. Therefore, we will characterise the collision of χ with a nucleon $\mathcal{N}$ and then deduce the cross sections for the elastic collisions with different nuclei. We will not consider inelastic collisions where χ may produce nuclear excitations[1].

The χ-nucleon interaction is then described by point-like *contact* potentials, being the dominant ones the so-called *spin-independent* (SI) and *spin-dependent* (SD) interactions:

$$\begin{aligned} V_{SI}(\vec{r}) &= c_1^i\,\delta^3(\vec{r}), \\ V_{SD}(\vec{r}) &= c_4^i\,\delta^3(\vec{r})\,\vec{S}_i\cdot\vec{S}_\chi, \end{aligned} \tag{3.22}$$

with $i = p, n$, c_1^i and c_4^i the coupling of χ to protons and neutrons, respectively, and $\vec{S}_i$ and $\vec{S}_\chi$ the two spins. Other interactions will involve the relative velocities ($\beta \approx 10^{-3}$) and are in principle subleading (they are in the model to be presented in next section). In the Born approximation the amplitude is

$$\begin{aligned} f_{SI}(\vec{q}) &= -\frac{\mu}{2\pi}\int \mathrm{d}^3 r\, V_{SI}(\vec{r})\, e^{-i\vec{q}\cdot\vec{r}}, \\ f_{SD}(\vec{q}) &= \langle\omega_\beta| - \frac{\mu}{2\pi}\int \mathrm{d}^3 r\, V_{SI}(\vec{r})\, e^{-i\vec{q}\cdot\vec{r}}|\omega_\alpha\rangle, \end{aligned} \tag{3.23}$$

where $m_{\mathcal{N}}$ is the mass of the nucleon, $\mu = m_{\mathcal{N}}\,m_{DM}/(m_{\mathcal{N}} + m_{DM})$ is the reduced mass of the system $|\omega_{\alpha(\beta)}\rangle$ the initial (final) states of spin. In an unpolarised collision we obtain [97]

$$\begin{aligned} \frac{\mathrm{d}\sigma_{SI}^i}{\mathrm{d}\Omega} &= \frac{\mu^2}{4\pi^2}\left|c_1^i\right|^2; \\ \frac{\mathrm{d}\sigma_{SD}^i}{\mathrm{d}\Omega} &= \frac{3\mu^2}{64\pi^2}\left|c_4^i\right|^2, \end{aligned} \tag{3.24}$$

or, in terms of the recoil energy,

$$\begin{aligned} \frac{\mathrm{d}\sigma_{SI}^i}{\mathrm{d}E_r} &= \frac{m_i}{2\pi w^2}\left|c_1^i\right|^2; \\ \frac{\mathrm{d}\sigma_{SD}^i}{\mathrm{d}E_r} &= \frac{2m_i}{32\pi w^2}\left|c_4^i\right|^2, \end{aligned} \tag{3.25}$$

where w is the incident velocity of the DM particle.

[1] They could have some relevance in the collisions of heavy DM (with a mass above 1 TeV) with certain nuclei.

Given the cross sections with protons and nucleons, the collisions with nuclei can be expressed in terms of the so-called nuclear form factors [98]:

$$\begin{aligned}\frac{\mathrm{d}\sigma^i_{SI}}{\mathrm{d}E_r} &= \frac{M_i}{2\pi w^2}\frac{1}{2J+1}\frac{1}{2}\sum_{\tau=0,1}\sum_{\tau'=0,1} 8\pi c_1^\tau c_1^{\tau'} W_M(y)\,;\\ \frac{\mathrm{d}\sigma^i_{SD}}{\mathrm{d}E_r} &= \frac{M_i}{2\pi w^2}\frac{1}{2J+1}\frac{1}{32}\sum_{\tau=0,1}\sum_{\tau'=0,1} 8\pi c_4^\tau c_4^{\tau'}\left(W^{\tau\tau'}_{\Sigma'}(y)+W^{\tau\tau'}_{\Sigma''}(y)\right)\,,\end{aligned} \tag{3.26}$$

where m_i is the mass of the nucleus i and $W^{\tau\tau'}_M(y)$, $W^{\tau\tau'}_{\Sigma'}(y)$ and $W^{\tau\tau'}_{\Sigma''}(y)$ are the so-called *nuclei response functions*, that are tabulated in [98]. These form factors depend on $y=(q\,b/2)^2$, with

$$q^2 = 2M_A E_r \tag{3.27}$$

and

$$b = \sqrt{\frac{2}{3}}\left(0.91\left(\frac{M_i}{\mathrm{GeV}}\right)^{1/3}+0.3\right)\frac{1}{0.197\,\mathrm{GeV}}, \tag{3.28}$$

whereas the constants c_i^τ, with $\tau=0,1$ are defined from the couplings of χ to protons and neutrons,

$$c^0_{1(4)} = c^p_{1(4)} + c^n_{1(4)}, \qquad c^1_{1(4)} = c^p_{1(4)} - c^n_{1(4)}. \tag{3.29}$$

Different direct-search experiments use different target nuclei, but they present deduced limits on the χ-nucleon cross section.

For the SI interaction they assume $c_1^n = c_1^p \equiv c_1$ and provide the bound on the total cross section (see Eq. ((3.24)):

$$\sigma_{SI} = \frac{\mu^2}{\pi}|c_1|^2. \tag{3.30}$$

The strongest bounds are currently given by XENON1T [94].

On the other hand, for the SD interaction they assume that only one type of nucleon couples to χ, *i.e.*, they give bounds on

$$\sigma^i_{SD} = \frac{3\mu^2}{16\pi}|c^i_4|^2 \tag{3.31}$$

for c_1^p with $c_1^n=0$ or viceversa. In this case PICO-60 [99] gives the most stringent limits. We have obtained fits of those results for different masses of the DM particle:

$$\begin{aligned}\sigma_{SI} &< 2.313\times10^{-21}\, m_\chi^{1+\left(\frac{13}{m_\chi}\right)^2}\,[\mathrm{GeV}^{-2}]\,;\\ \sigma^n_{SD} &< 3.855\times10^{-16}\, m_\chi^{1+\left(\frac{13}{m_\chi}\right)^2}\,[\mathrm{GeV}^{-2}]\,;\\ \sigma^p_{SD} &< 1.4649\times10^{-15}\, m_\chi^{0.93+\left(\frac{13}{2+m_\chi}\right)^2}\,[\mathrm{GeV}^{-2}]\,.\end{aligned} \tag{3.32}$$

where m_χ is in GeV. These expressions give the maximum value of the couplings compatible with direct searches, and they will be used in the next section to compute the maximum capture rate of DM by the Sun.

Capture rate: $K_A = 0$

Let us deduce the capture rate if we neglect the kinetic energy of the solar nuclei. The differential cross section $\mathrm{d}\sigma_{\chi i}/\mathrm{d}E_r$ is

$$\frac{\mathrm{d}\sigma_{\chi i}}{\mathrm{d}E_r} \equiv \frac{m_i}{2\pi w^2}\, c_i^2\,, \tag{3.33}$$

where the DM velocity $w(r)$ in the Sun is related to the velocity u before the fall, and the scape velocity $v(r)$ at the point of the collision by $w = \sqrt{v^2+u^2}$. The total cross section for a capture would then be

$$\sigma_{\chi i}(r,w) = \int_{m_\chi u^2/2}^{E_r^{\max}} \mathrm{d}E_r\, \frac{\mathrm{d}\sigma_{\chi i}}{\mathrm{d}E_r}, \tag{3.34}$$

where $E_r^{\max} = \epsilon\, m_\chi w^2/2$ with $\epsilon = 4m_\chi m_i/(m_\chi+m_i)^2$. The capture rate is

$$\begin{aligned}
\frac{\mathrm{d}N_\chi^{(i)}}{\mathrm{d}t} =& \int_0^{R_\odot} \mathrm{d}r\, r^2\, n_i \int \mathrm{d}\Omega_r \int_v^{\sqrt{v^2+v_{\rm esc}}} \mathrm{d}w\, w^3 \int_{m_\chi u^2/2}^{E_r^{\max}} \mathrm{d}E_r\, \frac{\mathrm{d}\sigma_{\chi i}}{\mathrm{d}E_r} \int \mathrm{d}\Omega_w\, f(\vec{u}[\vec{w},\vec{r}]) \\
=& \frac{4\pi\,\rho_\chi}{m_\chi} \int_0^{R_\odot} \mathrm{d}r\, r^2\, n_i \int_0^{v_{\rm esc}} \mathrm{d}u\, \tilde{f}(u)\, u\,(u^2+v^2) \int_{m_\chi u^2/2}^{\epsilon\, m_\chi (u^2+v^2)/2} \mathrm{d}E_r\, \frac{m_i}{2\pi w^2}\, c_i^2 \\
=& \frac{2\rho_\chi m_i}{m_\chi} \int_0^{R_\odot} \mathrm{d}r\, r^2\, n_i \int_0^{v_{\rm esc}} \mathrm{d}u\, \tilde{f}(u)\, u \int_{m_\chi u^2/2}^{\epsilon\, m_\chi (u^2+v^2)/2} \mathrm{d}E_r\, c_i^2\,,
\end{aligned} \tag{3.35}$$

where $v_{\rm esc}$ is the scape velocity from the galaxy. Notice that c_i depends on E_r (or $q^2 = 2m_i E_r$), that the $\Theta[\epsilon(u^2+v^2)-u^2]$ factor inside the last integral is implicit, and that

$$\int_0^{v_{\rm esc}+v_{\rm rot}} \mathrm{d}u\, u^2\, \tilde{f}(u) = 1\,. \tag{3.36}$$

Capture rate: $K_A = \frac{3}{2}\,T$

Let us assume that all nuclei have a thermal energy of $3T(r)/2$. The relative velocity in the collision depends now on the parameter α introduced before ($\alpha = 0$ in a head

on collision):

$$v_{\,\mathrm{rel}} = \sqrt{w^2 + v_i^2 + 2wv_i\cos\alpha}\,. \tag{3.37}$$

The energy E_r lost by χ in the frame with i at rest is not a good kinematical variable to describe the collision in this case, and we use instead the scattering angle in the center of mass frame:

$$\frac{\mathrm{d}\sigma_{\chi i}}{\mathrm{d}\phi\ \mathrm{d}(\cos\theta)} = \frac{v_{\,\mathrm{rel}}^2}{2\pi}\,\frac{m_i m_\chi^2}{(m_i+m_\chi)^2}\,\frac{\mathrm{d}\sigma_{\chi i}}{\mathrm{d}E_r} \tag{3.38}$$

$$= \frac{c_i^2}{4\pi^2}\,\frac{m_i^2 m_\chi^2}{(m_i+m_\chi)^2}\,, \tag{3.39}$$

where the form factors in the coupling c_i with the nucleus type i depend now on

$$q^2 = \frac{2\,m_\chi^2 m_i^2\,v_{\,\mathrm{rel}}^2}{(m_i+m_\chi)^2}\,(1-\cos\theta)\,. \tag{3.40}$$

For a given value of $v_{\,\mathrm{rel}}$ and w, the kinetic energy K'_χ of χ in the lab frame after the collision depends on the two angles θ and ϕ:

$$\begin{aligned} K'_\chi =& \frac{m_\chi}{2(m_i+m_\chi)^2}\Big(\big(m_\chi w - m_i v_i c_\alpha + m_i v_{\,\mathrm{rel}} c_\theta\big)^2 \\ &+ m_i^2\,v_{\,\mathrm{rel}}^2 s_\phi^2 s_\theta^2 + \big(m_i v_i s_\alpha + m_i v_{\,\mathrm{rel}} c_\phi s_\theta\big)^2\Big)\,, \end{aligned} \tag{3.41}$$

and for χ to be captured K'_χ must be below $m_\chi v_{\mathrm{esc}}^2/2$:

$$\begin{aligned} v_{\mathrm{esc}}^2 <& \frac{1}{(m_i+m_\chi)^2}\Big(\big(m_\chi w - m_i v_i\cos\alpha + m_i v_{\,\mathrm{rel}}\cos\theta\big)^2 + m_i^2\,v_{\,\mathrm{rel}}^2\sin^2\phi\sin^2\theta \\ &+ \big(m_i v_i\sin\alpha + m_i v_{\,\mathrm{rel}}\cos\phi\sin\theta\big)^2\Big) \equiv v_{\mathrm{f}}^2(w, v_i, \alpha, \theta, \phi). \end{aligned} \tag{3.42}$$

The capture rate is then

$$\begin{aligned} \frac{\mathrm{d}N_\chi^{(i)}}{\mathrm{d}t} =& \int_0^{R_\odot}\mathrm{d}r\,r^2\,\frac{n_i}{2}\int_{-1}^{+1}\mathrm{d}(\cos\alpha)\int\mathrm{d}\Omega_r\int_v^{\sqrt{v^2+v_{\mathrm{esc}}^2}}\mathrm{d}w\,w^2\,v_{\,\mathrm{rel}}\int_0^{2\pi}\mathrm{d}\phi \\ &\int_{-1}^{+1}\mathrm{d}(\cos\theta)\ \frac{\mathrm{d}\sigma_{\chi i}}{\mathrm{d}\phi\ \mathrm{d}(\cos\theta)}\,\Theta[v_{\mathrm{esc}}^2 - v_{\mathrm{f}}^2]\int\mathrm{d}\Omega_w\ f\,(\vec{u}[\vec{w},\vec{r}])\,. \end{aligned} \tag{3.43}$$

We obtain

$$\begin{aligned} \frac{\mathrm{d}N_\chi^{(i)}}{\mathrm{d}t} =& \frac{\rho_\chi m_i^2 m_\chi}{2\pi(m_i+m_\chi)^2}\int_0^{R_\odot}\mathrm{d}r\,r^2\,n_i\int_0^{v_{\mathrm{esc}}}\mathrm{d}u\,\tilde{f}(u)\,u\,\sqrt{u^2+v^2} \\ &\int_{-1}^{+1}\mathrm{d}(\cos\alpha)\ v_{\,\mathrm{rel}}\int_0^{2\pi}\mathrm{d}\phi\int_{-1}^{+1}\mathrm{d}(\cos\theta)\ c_i^2\ \Theta[v_{\mathrm{esc}}^2 - v_{\mathrm{f}}^2]\,. \end{aligned} \tag{3.44}$$

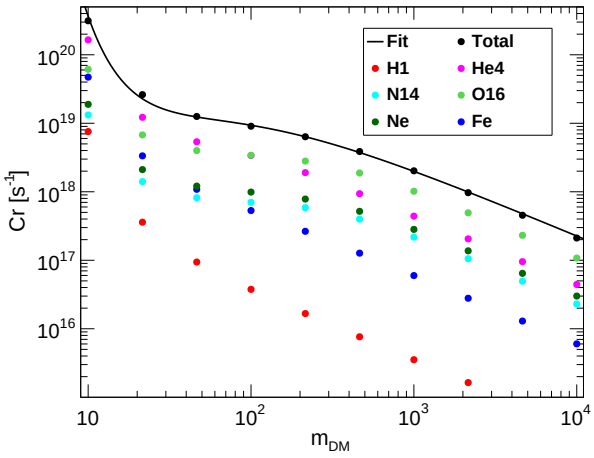

Figure 3.5: Total capture rate in the Sun, together with the contribution of the most relevant nuclei.

Solving this last expression for a large number of points involves a significant computing time. The fit to the total capture rate calculated for several masses fives the following result:

$$C_r(m_\chi) = 10^{21.363} \cdot m_\chi^{-\left(1+\frac{22}{m_\chi}-\frac{240}{m_\chi^2}\right)}, \tag{3.45}$$

with m_χ in GeV. Fig. 3.5 shows the total capture rate as a function of the WIMP mass in the Sun, together with the fit and the contribution of the most relevant nuclei (^{1}H, ^{4}He, ^{14}N, ^{16}O, Ne, Fe). It can be observed that the most relevant nuclei are helium (due to its higher abundance in the solar medium) and ^{16}O.

We have also compared the capture rate with and without the thermal velocity for the solar nuclei. We find that H nuclei increase the capture rate of 100 GeV DM in a 7%, whereas the solar Fe nuclei reduce it in a 20%. The total effect of all nuclei tends to cancel and is completely negligible (below 2%).

3.2 A dark matter model through the Higgs portal

Matter content and free parameters

Let us use a notation with 2-component spinors of left-handed chirality (or *undotted*) in the definition of the model, as we think that it is more transparent to establish the quantum numbers of the fields. In this notation e_α and e^c_α denote the electron left and the positron also left, with lepton numbers $+1$ and -1, respectively. In turn, their conjugate-contravariant, $\bar{e}^{\dot\alpha}$ and $\bar{e^c}^{\dot\alpha}$, are right-handed spinors (or *dotted*) with the opposite lepton number. The usual 4-component spinors in the chiral representation of γ^μ can then be easily defined as $\Psi_e = \begin{pmatrix} e_\alpha \\ \bar{e^c}^{\dot\alpha} \end{pmatrix}$ [being $\bar\Psi_e = (e^{c\,\alpha}\ \bar{e}_{\dot\alpha})$], while $\Psi_\chi = \begin{pmatrix} \chi_\alpha \\ \bar\chi^{\dot\alpha} \end{pmatrix}$ is a Majorana fermion (from this point we omit the Lorentz indexes α and $\dot\alpha$).

To the SM matter content we add a Majorana singlet χ that will constitute the DM particle.[1] We assign -1 matter parity to χ and $+1$ to the rest of fields, so that this parity forbids χ decays. The Majorana nature of χ is not essential, very similar results would be obtained for a Dirac fermion. In addition to χ, we add two fermion singlets (N, N^c) with lepton number $+1$ and -1, respectively, that define a vector-like Dirac fermion Ψ_N of mass m_N. We will assume that these extra fields are heavy but not far from the EW scale, $m_N \sim m_\chi \leq 1$ TeV.

We will then assume that this is an effective theory valid at energies below Λ. The dominant operators of dimension ≤ 6 allowed by the symmetries are

$$\begin{aligned} -\mathcal{L} \supset & \frac{1}{2}\, m_\chi\, \chi\chi + \frac{c_s}{\Lambda}\, H^\dagger H\, \chi\chi + i\, \frac{c_a}{\Lambda}\, H^\dagger H\, \chi\chi + \ m_N\, N N^c \\ & + \ y_N\, H L N^c + i\, \frac{c_N}{\Lambda^2} \left(N N^c + \bar N \bar N^c\right) (\chi\chi) + \text{h.c.}\,, \end{aligned} \tag{3.46}$$

being $H = (h^+\ h^0)$ the SM Higgs and $L = (\nu\ \ell)$ a SM lepton doublet assumed mainly along the τ flavor (collider bounds on the Yukawa for the other two lepton flavors are stronger). The six parameters in the effective Lagrangian above (m_χ, c_s/Λ, c_a/Λ, m_N, y_N and c_N/Λ^2) are taken (after field redefinitions) as real, and we assume that the rest of dim-5,6 operators give subleading effects and can be neglected (later on we will comment on the possible effect of $H^\dagger H N N^c$). Notice also that in the usual 4-spinor notation the operators connecting χ with H plus their conjugate are just

[1] For consistency with other sections of this thesis, the DM candidate is referred to indistinguishably as DM or χ.

$(c_s/\Lambda)\, H^\dagger H\, \bar{\Psi}_\chi \Psi_\chi - (ic_a/\Lambda)\, H^\dagger H\, \bar{\Psi}_\chi \gamma_5 \Psi_\chi$, whereas the dim-6 operator would read $(-ic_N/\Lambda^2)\, (\bar{\Psi}_N \Psi_N)(\bar{\Psi}_\chi \gamma_5 \Psi_\chi)$.

The higher dimensional operators in this model may appear as the result of integrating out heavier fields. In particular, the simplest possibilities are

i. **A real scalar singlet** $[s]$ even under the matter parity. Its interactions should include the trilinear term $sH^\dagger H$ with the Higgs boson and also a Yukawa interaction with the DM particle, $s\chi\chi$. The real and imaginary parts of this last coupling would contribute to c_s and c_a, respectively. Finally, the scalar singlet should also be connected to the heavy neutrinos through sNN^c. Notice that in such UV complete scenario the SM Higgs will necessarily mix with s, resulting in a Higgs mass eigenstate with a small singlet component [100].

ii. **A vectorlike lepton doublet** $[(D, D^c)]$ odd under the matter parity. Interaction terms $HD\chi$ and $H^\dagger D^c \chi$ would induce values of c_s and c_a, with c_s/c_a proportional to the relative complex phase in these two Yukawa couplings. In this scenario it is not the SM Higgs doublet who mixes with the heavy field, but the DM particle χ: it will acquire a small doublet component through mixing with the neutral components in (D, D^c).

To simplify our DM model we will assume a regime where s and (D, D^c) are heavier than χ and N, so that the effect of the mixing with the heavy fields can be neglected and the effective approach is a good approximation.

At the EW minimum, $\langle H \rangle = (0\ v/\sqrt{2})$, the Lagrangian in the unitary gauge becomes (we use prime to denote mass eigenstates)

$$\begin{aligned} -\mathcal{L} \supset & \frac{1}{2}\, m'_\chi\, \chi\chi + m'_N\, N' N^c + \frac{\tilde{y}_N}{\sqrt{2}}\, h\, \nu' N^c + \frac{c_s + ic_a}{2\Lambda}\, (hh\, \chi\chi + 2h\, \chi\chi) \\ & + \frac{ic_N}{\Lambda^2}\, (c_\alpha\, N' N^c + s_\alpha\, \nu' N^c + c_\alpha\, \bar{N}' \bar{N}^c + s_\alpha\, \bar{\nu}' \bar{N}^c)\, (\chi\chi) + \text{h.c.}\,, \end{aligned} \tag{3.47}$$

where $N' = c_\alpha\, N + s_\alpha\, \nu$ and N^c combine into a heavy Dirac neutrino of mass

$$m'_N = \sqrt{\left(\frac{y_N v}{\sqrt{2}}\right)^2 + m_N^2}. \tag{3.48}$$

Notice that the orthogonal combination $\nu' = c_\alpha\, \nu - s_\alpha\, N$ still remains massless. The active-sterile mixing parameter s_α is given by $s_\alpha = y_N\, v/(\sqrt{2}\, m'_N)$, while the Yukawa coupling $\tilde{y}_N$ can be expressed as

$$\tilde{y}_N = y_N\, c_\alpha = \frac{\sqrt{2}\, m'_N}{v}\, c_\alpha\, s_\alpha\,. \tag{3.49}$$

This coupling may receive a contribution from the dim-5 operator $H^\dagger H\, N N^c$ that could be relevant when $m'_N \leq v$.

In this scenario the masses of the SM neutrinos ν' would appear through an inverse see-saw mechanism [101, 102]. A specific model along this line has been proposed in [103, 104] as a solution to the so-called H_0 tension.

Cross sections

Our objective is to define a model with a significant production of monochromatic neutrinos via the annihilation channel $\chi\chi \to N\nu$ in the Sun (we use $N\nu$ to express $\bar{N}\nu + N\bar{\nu}$), so that the signal at neutrino telescopes may be above the CR background. Therefore, we will consider relatively large values of the couplings $\tilde{y}_N$ and/or c_N. Notice, in particular, that the Yukawa coupling $\tilde{y}_N$ does not give mass to the active neutrino: it is only constrained by collider limits on the heavy-light mixing, which are weaker for the tau flavor ($s_\alpha \leq 0.1$) [105, 106, 107]. Since $s_\alpha = m_N/(174\,\text{GeV})$, only values of m_N greater than 1 TeV will allow for top-like Yukawa couplings. For heavy neutrinos lighter than the Z^0 and $W^\pm$ gauge bosons, however, we have stronger LEP bounds on $Z \to N\nu$ and then $N \to \tau W^*, \nu Z^*$. For this reason, we will consider models with $m_N > M_Z$. On the other hand, if we want that the annihilation channel $\chi\chi \to N\nu$ is open, it is required that $m_\chi > M_Z/2$. Therefore, in this analysis we will consider a DM mass $m_\chi \geq 50$ GeV along with $m_N \geq 100$ GeV, $s_\alpha = 0.1$ (to optimise the monochromatic signal) and $c_i/\Lambda < 1/(2m_\chi), 1/v$ (so that the effective theory approach is valid).

The annihilation channels for χ in both the early universe and astrophysical environments are shown in Fig. 3.6. When the contribution from c_N (corresponding to the last two diagrams in the figure) can be neglected, the cross section can be written as follows:

$$\sigma^{(1)}_{\text{ann}} = \frac{c_s^2\left(1-\frac{4m_\chi^2}{s}\right)+c_a^2}{4\pi\Lambda^2\left(1-\frac{4m_\chi^2}{s}\right)^{1/2}} f(m_\chi) \approx \frac{c_s^2\,\beta^2+c_a^2}{4\pi\Lambda^2\,\beta} f(m_\chi)\,, \tag{3.50}$$

being β the velocity of χ in the centre of mass frame and $f(m_\chi) = \sum_i f_i$ the

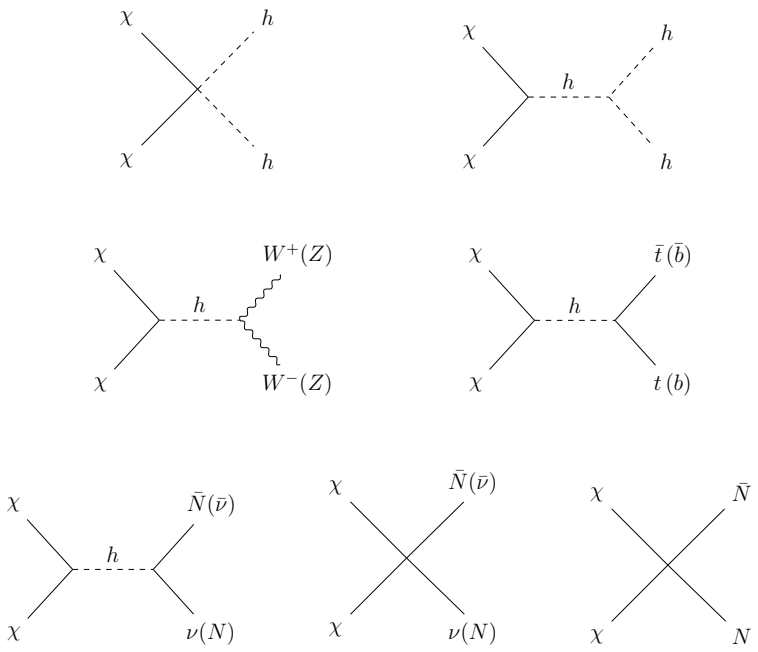

Figure 3.6: Leading diagrams in the DM annihilation. The third row produces heavy neutrinos.

contribution of the different channels. In particular:

$$
\begin{aligned}
f_{hh} &= \left(1+\frac{3m_h^2}{s-m_h^2}\right)\sqrt{1-\frac{4m_h^2}{s}},\\
f_{QQ} &= \frac{3m_Q^2\left(s-4m_Q^2\right)}{\left(s-m_h^2\right)^2}\sqrt{1-\frac{4m_Q^2}{s}},\\
f_{VV} &= \frac{2m_V^4}{\left(s-m_h\right)^2}\left[2+\left(1-\frac{s}{2m_V^2}\right)^2\right]\sqrt{1-\frac{4m_V^2}{s}},\\
f_{N\nu}^{(1)} &= \frac{\tilde{y}_N^2 v^2\left(s-m_N^2\right)}{2\left(s-m_h^2\right)^2}\left(1-\frac{m_N^2}{s}\right),
\end{aligned}
\tag{3.51}
$$

being $Q = t, b$ and $V = Z, W$.

For sizeable values of c_N, the two last diagrams introduce two more terms:

$$
\sigma_{\text{ann}}^{(2)} = \frac{c_N^2}{4\pi\Lambda^2\left(1-\frac{4m_\chi^2}{s}\right)^{1/2}}\left(f_{NN}+f_{N\nu}^{(2)}\right), \tag{3.52}
$$

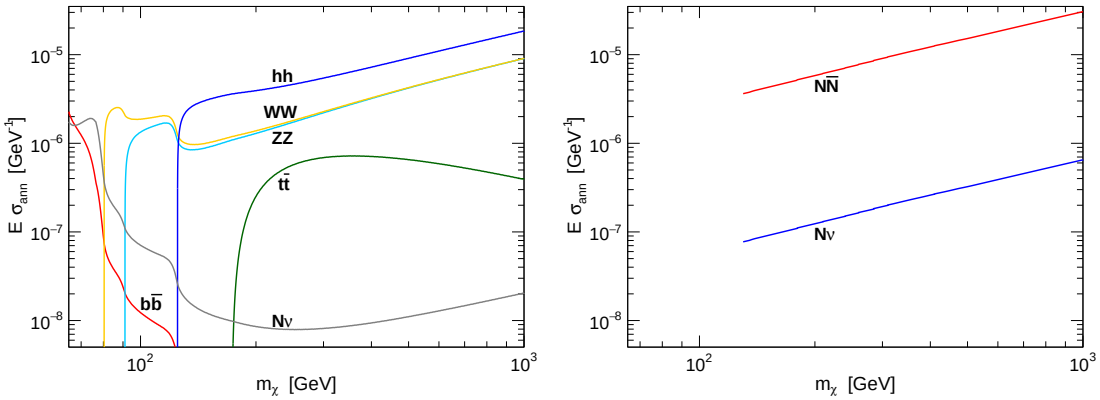

Figure 3.7: Different contributions to σ_{ann} for $s_\alpha = 0.1$ and $\beta = 1/20$. Left: $c_N \to 0$, $m_N = 1.4\, m_\chi$. Right: $c_a \to 0$, $m_N = 0.7\, m_\chi$.

where

$$f_{NN} = \frac{c_\alpha^2\,(s - 4m_N^2)}{\Lambda^2}\sqrt{1 - \frac{4m_N^2}{s}},$$
$$f_{N\nu}^{(2)} = \left(\frac{s_\alpha^2}{\Lambda^2} - \frac{\sqrt{2}\,c_a\,\tilde{y}_N v}{c_N \Lambda\,(s - m_h^2)}\right)(s - m_N^2)\left(1 - \frac{m_N^2}{s}\right). \tag{3.53}$$

Fig. 3.7 shows the contribution of the different considered channels in the limits $c_N \to 0$ and $c_a \to 0$. Notice that for $s \approx 4m_\chi^2$ the channel $\chi\chi \to N\nu$ produces an active neutrino of energy

$$E_\nu = m_\chi\left(1 - \frac{m_N^2}{4m_\chi^2}\right). \tag{3.54}$$

As mentioned before, we impose the condition $m_N > M_{W,Z}$, but not $m_N > m_h$. In the cases where $m_N < m_h$ and the Higgs is able to decay $h \to N\nu$, we will assume a value of y_N giving a 10% branching ratio for this Higgs decay channel.

In addition to the annihilation cross section, to characterise the phenomenology of this DM model we also need to determine the elastic cross section of a DM particle χ off a nucleon $\mathcal{N}$. This interaction will be mediated by a Higgs in the t channel: our model uses the so called Higgs portal. In the SM the Higgs boson interacts with the quarks and, through heavy quark loops, also with the gluons in a nucleon. At lower energies, this interaction defines an effective Higgs-nucleon Yukawa coupling denoted as $g_{h\mathcal{N}}$, which is usually parametrised as $g_{h\mathcal{N}} = f_{\mathcal{N}} m_{\mathcal{N}}/v$ [108, 109]. We take $m_{\mathcal{N}} = 0.94$ GeV and $f_{\mathcal{N}} = 0.30$ [110, 111]. The calculation of the cross section

gives then

$$\sigma(\chi\mathcal{N}\to\chi\mathcal{N}) = \frac{4}{\pi}\,\frac{c_s^2 + c_a^2\,\beta^2}{\Lambda^2}\left(\frac{\mu_{\mathcal{N}}\,m_{\mathcal{N}} f_{\mathcal{N}}}{m_h^2}\right)^2, \tag{3.55}$$

with $\mu_{\mathcal{N}} = m_{\mathcal{N}} m_\chi/(m_{\mathcal{N}} + m_\chi)$.

Direct searches and relic abundance

Direct searches are designed to detect the recoil of a nucleus hit by a DM particle travelling in our galaxy at a velocity $\beta \approx 10^{-3}$. Therefore, these experiments do not significantly constrain the coupling c_a in Eq. (3.55), as its contribution to the cross section is suppressed by a factor of β^2. These experiments do not constrain the coupling c_N neither, since this couplings affects the interaction of χ only to neutrinos. As a consequence, in our model the parameters c_a and c_N can be adjusted to reproduce the relic abundance for each value of m_χ unconstrained by direct searches.

The coupling c_s leads to an unsuppressed spin-independent scattering cross section with nucleons that must respect XENON1T bounds [94]. For DM masses m_χ ranging from 10 GeV to 10 TeV, we fit the maximum cross section consistent with these bounds to

$$\sigma^{\rm SI}_{\chi\mathcal{N}} \leq 0.9\times 10^{-48}\, m_\chi^{1+169/m_\chi^2}\ {\rm cm}^2, \tag{3.56}$$

where m_χ must be expressed in GeV. This implies a maximum value for c_s/Λ from direct searches,

$$\frac{c_s}{\Lambda} \leq \frac{c_s^{\rm max}}{\Lambda} \approx 2.5\times 10^{-6}\,\frac{0.94 + m_\chi}{\sqrt{m_\chi^{1-169/m_\chi^2}}}\ {\rm GeV}^{-1}, \tag{3.57}$$

a result that we plot in Fig. 3.8.

Once the value of c_s is fixed, it is straightforward to obtain the DM relic abundance. In the annihilation cross section (in Eq. (3.50)), we see that the contribution of c_s (which is dominant in elastic scatterings) undergoes suppression by a factor of β^2. During freeze-out the DM particles have a $\beta \approx 1/20$, so its contribution will be subleading. The dominant contributions to DM annihilation will then come from c_a and/or c_N. In order to determine the values of these couplings that yield the observed DM relic abundance $\Omega_c h^2 \approx 0.12$ for each m_χ, we will consider two cases (see Fig. 3.8):

I. In scenarios where $c_N \to 0$, we obtain a specific value of c_a/Λ that yields $\Omega_c h^2 \approx 0.12$. In this case the dominant annihilation channel is into a pair of

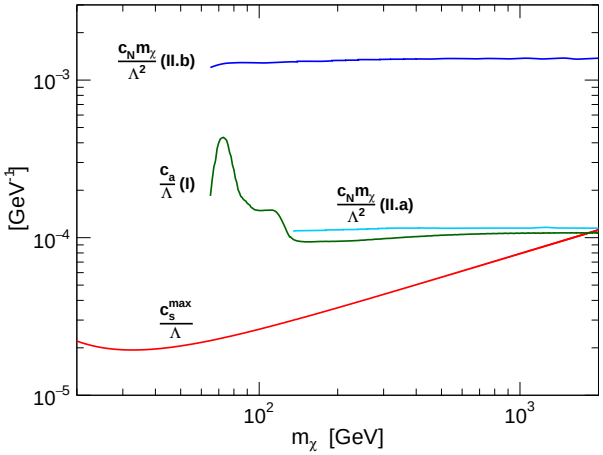

Figure 3.8: Maximum coupling c_s/Λ allowed by direct searches data in XENON1T together with the value of c_a/Λ for $m_N = 1.4\, m_\chi$ (case I) or $c_N m_\chi/\Lambda^2$ with $m_N = 0.7\, m_\chi$ (case II.a) and $1.4\, m_\chi$ (II.b) implying $\Omega_c h^2 = 0.12$.

Higgs bosons, while $\chi\chi \to N\nu$ is subleading. The dependence of c_a/Λ on m_N can then be neglected. We illustrate this case in Fig. 3.8, where we show the result for $m_N = 1.4\, m_\chi$.

II. If $c_a \to 0$ a suitable value of c_N/Λ^2 can also achieve the correct relic abundance. However, we have to distinguish two possibilities:

- Case II.a: When $m_N < m_\chi$, the channel $\chi\bar{\chi} \to N\bar{N}$ is open. We plot in Fig. 3.8 the value of the coupling for $m_N = 0.7 m_\chi$ and different values of m_χ.
- Case II.b: In scenarios where $m_N > m_\chi$, the DM particle predominantly annihilates into $N\nu$. This case optimises the production of monochromatic neutrinos. We plot in Fig. 3.8 the value of c_N/Λ^2 giving the *right* relic abundance for $m_N = 1.4 m_\chi$.

In a general model we may have a combination of both cases with weights $\omega_a = c_a^2/\tilde{c}_a^2$ and $\omega_N = c_N^2/\tilde{c}_N^2$, where $\tilde{c}_a$ and $\tilde{c}_N$ represent the values of the couplings in the two corresponding limiting cases. Varying these weights we obtain a comprehensive representation of the model's implications.

3.3 Signal at neutrino telescopes

We will finally study the signal predicted by this model at neutrino telescopes. More specifically, we would like to test whether the signal from DM annihilation in the Sun could be larger than the background of atmospheric neutrinos and neutrinos produced in the showering of CRs in the solar surface [31, 61, 71, 75, 86] (see Secs. §2.3 and §2.4).

Notice, first of all, that the capture rate $C = \mathrm{d}N_\chi^{\mathrm{cap}}/\mathrm{d}t$ of DM by the Sun depends on the same elastic cross section that is constrained in direct searches. Therefore, we will take the maximum coupling $c_s^{\max}/\Lambda$ consistent with the bounds from XENON1T. As explained in Sec. §2.1 for a generic model, a maximum spin-independent coupling implies a maximum capture rate that (for $m_\chi \geq 10$ GeV) can be fitted with the expression in Eq. (3.45). This result includes collisions with the seven most abundant nuclei in the Sun (^{1}H, ^{4}He, ^{13}C, ^{14}N, ^{16}O, Ne, Fe) in the AGSS09 solar model for the SHM^{++} DM velocity distribution.

The captured DM will then accumulate in the Sun, as its evaporation through collisions with the solar nuclei is negligible at $m_\chi \geq 3$ GeV [112, 113]. Its concentration will increase until the probability to annihilate with another DM particle may be significant. Eventually, the system will evolve to a stationary regime where the annihilation rate Γ_A is half the capture rate, *i.e.*, $\Gamma_A = C_r/2$. The usual analyses for the DM signal at telescopes are *optimistic*, in the sense that they assume that the stationary regime has been achieved. Here, however, both the capture and the annihilation processes in the Sun have well defined rates and this issue can be explicitly studied. While our model implies a relatively large annihilation cross section to account for the observed relic abundance, the bounds on the capture rate from direct searches are also strong, and it is unclear whether the age of the Sun, approximately $t_\odot \approx 4.5$ Gyr, has been long enough. Specifically, if we express $\Gamma_A \equiv \frac{1}{2} C_A N_\chi^2$ [114], the time scale τ needed for capture and annihilation to achieve equilibrium is given by $\tau = (C_r C_A)^{-1/2}$, and [41]

$$\frac{t_\odot}{\tau} \approx 330 \left(\frac{C_r}{\mathrm{s}^{-1}}\right)^{1/2} \left(\frac{\langle \sigma_{\mathrm{ann}} \beta \rangle}{\mathrm{cm}^3\,\mathrm{s}^{-1}}\right)^{1/2} \left(\frac{m_\chi}{10\,\mathrm{GeV}}\right)^{3/4} . \tag{3.58}$$

When $t_\odot/\tau \gg 1$, then $\Gamma_A \approx C/2$. Otherwise, the annihilation rate can be expressed as

$$\Gamma_A = \frac{C}{2} \tanh^2 \frac{t_\odot}{\tau} . \tag{3.59}$$

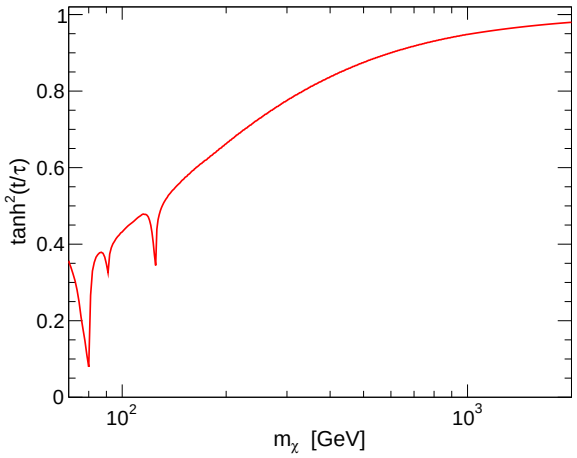

Figure 3.9: Suppression factor $\tanh^2(t_\odot/\tau)$ for different values of m_χ.

Fig. 3.9 shows the suppression factor in our model as a function of the mass of the WIMP, m_χ. We see that, although the stationary regime can not be assumed (specially for low masses of the WIMP), the suppression is not very strong.

Once produced, neutrinos must escape the Sun and propagate from the Sun to

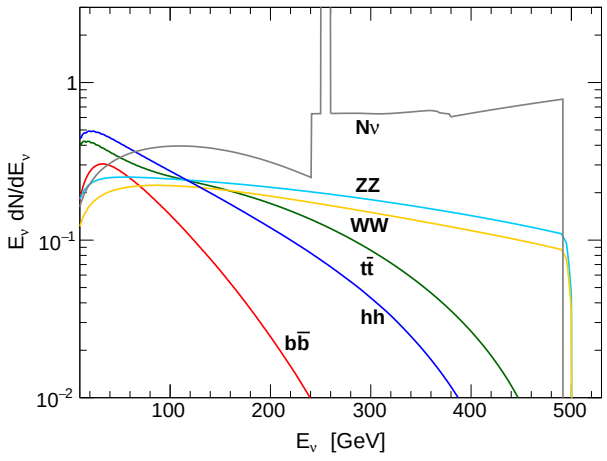

Figure 3.10: Neutrino yield per one annihilation through each channel for $m_\chi = 500$ GeV, $m_N = 700$ GeV.

the Earth. In our estimate we have used the Monte Carlo simulator χaroν [115]. For illustration, Fig. 3.10 shows the total neutrino yield (both ν and $\bar{\nu}$ of all flavors combined) per annihilation through each channel for a specific scenario with $m_\chi = 500$ GeV and $m_N = 1.4\, m_\chi$. Let us briefly discuss two different scenarios that can be used to calibrate the possible relevance of this model at neutrino telescopes.

$\mathbf{m_{DM} = 300\ GeV,\ m_N = 105\ GeV}$

The condition $m_N > m_Z$ has been imposed in order to avoid the decays of weak bosons into the heavy neutrino: $Z \to N\nu$, $W \to N\ell$, with ℓ being typically the τ lepton. Such decays would have been noticed at LEP [116], an e^+e^- collider that produced 17 million Z^0 bosons in the 90's. However, we have allowed the possibility that N is produced in Higgs decays ($h \to N\nu$) as long as this Higgs branching ratio is below 10%. At the LHC an event where the Higgs produces a heavy neutrino that subsequently decays $N \to \ell W$ would look very similar to $h \to W^*W$ and then $W^* \to \nu\ell$, with two leptons of opposite charge in the final state. This process still remains unobserved for $\ell = \tau$ [117, 118], whereas for $\ell = e, \mu$ it would introduce a small correction in $h \to W^*W$ searches. The 10% increase in the total Higgs width introduced by the new channel would also be experimentally allowed. Similar arguments apply to $h \to N\nu$ with $N \to Z\nu$, which would change $h \to Z^*Z$ plus one (or both [119]) of the Z bosons decaying into neutrinos [120].

As a specific case we consider $m_\chi = 300$ GeV, $m_N = 105$ GeV, and a Yukawa coupling $\tilde{y}_N = 0.11$ resulting into BR$(h \to N\nu) = 0.1$. We take the maximum coupling consistent with direct limits, $c_s^{\max}/\Lambda = 4.37 \times 10^{-5}$ GeV^{-1}, plus the values of c_a/Λ and c_N/Λ^2 that yield $\omega_a = 0.5 = \omega_N$. This means that DM annihilates with equal frequency to $(N\bar{N} + N\bar{\nu} + \bar{N}\nu)$ or to any of the six channels in Fig. 3.7 left.

For these values of m_χ and m_N, the dominant annihilation channels are into Higgs boson pairs and heavy neutrinos. The neutrinos ν resulting from $\chi\chi \to hh$ plus $h \to N\nu$ are not monochromatic; their energy is distributed between

$$E_\nu^{\min} = \frac{1}{2}\left(m_\chi - \sqrt{m_\chi^2 - m_h^2} - \frac{m_N^2}{m_\chi + \sqrt{m_\chi^2 - m_h^2}} \right) \tag{3.60}$$

and

$$E_\nu^{\max} = \frac{1}{2}\left(m_\chi + \sqrt{m_\chi^2 - m_h^2} - \frac{m_N^2}{m_\chi - \sqrt{m_\chi^2 - m_h^2}} \right) . \tag{3.61}$$

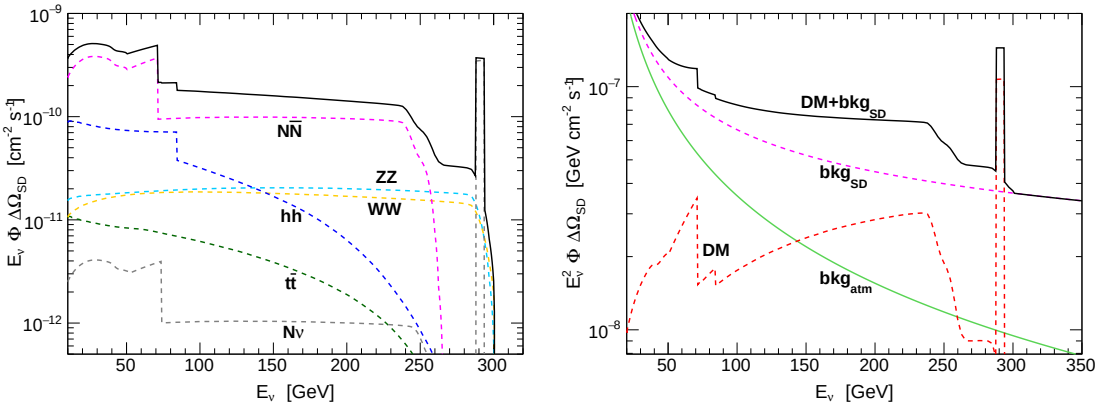

Figure 3.11: Solar neutrino flux for $m_\chi = 300$ GeV, $m_N = 105$ GeV, $\omega_a = 0.5 = \omega_N$. The left plot shows the contribution of the different annihilation channels, while the right plot shows the total flux coming from the solar disk including the CR background (bkg_{SD}). The bin containing the monochromatic neutrinos has a width of 6 GeV.

However, as m_χ approaches m_h this energy interval narrows down. In the particular case that we have chosen it ranges from 4 GeV to 84 GeV, while the monochromatic channel $\chi\chi \to N\nu$ produces neutrinos with an energy of $E_\nu = 290$ GeV.

Fig. 3.11 left shows the contribution of each annihilation channel to the neutrino flux from DM annihilation in the Sun, whereas Fig. 3.11 right shows the signal and the background from the solar disk for $\theta_z = 45°$. We have included the atmospheric flux from a *fake* Sun at the same zenith angle for comparison.

$\mathbf{m_{DM} = 1\ TeV,\ m_N = 1.4\ TeV}$

In this case the DM is very heavy and all annihilation channels into standard particles are open, but N is also heavy and the $\chi\chi \to N\bar{N}$ channel is closed. We have taken the maximum value of c_s/Λ that is consistent with direct bounds and have assumed that the channels in Fig. 3.7 left contribute 50% to σ_{ann}, with $\chi\chi \to N\nu$ providing the other half of annihilations. In this scenario the Higgs decays remain unaffected by the heavy neutrino, which may only manifest in the anomalous couplings of the light neutrinos [105, 106, 107].

The DM signal (see Fig. 3.12) in this case significantly surpasses the CR background from the solar disk: 2.28 neutrinos per km^2 and second in the 500–1000 GeV range from DM annihilation (with 1.62 of them in the 500–520 GeV energy bin),

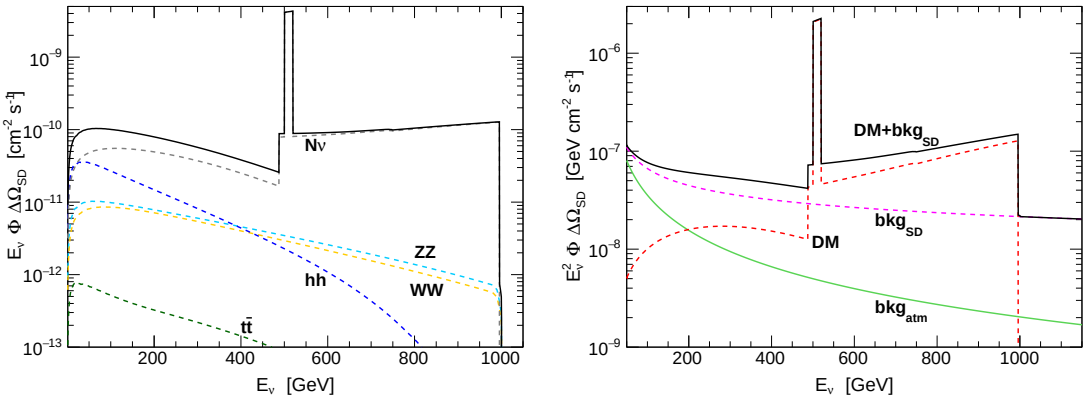

Figure 3.12: Solar neutrino flux for $m_\chi = 1$ TeV, $m_N = 1.4$ TeV, $\omega_a = 0.5 = \omega_N$. The left plot shows the contribution of the different annihilation channels, while the right plot shows the total flux coming from the solar disk including the CR background ($\mathrm{bkg_{SD}}$). The bin containing the monochromatic neutrinos has a width of 20 GeV.

while only 0.25 neutrinos originate from CR showers in the solar surface or from the partial CR shadow of the Sun. The atmospheric background from a simulated Sun at the same zenith inclination amounts to 0.03 $\mathrm{km^{-2}\ s^{-1}}$ in the same energy interval.

3.4 Discussion

The WIMP paradigm has been studied for decades, and currently a variety of experiments severely constrains the different models. In particular, the absence of a signal in direct searches and of missing E_T at the LHC discard the Z and W gauge bosons as viable mediators of its interactions with the visible sector, as suggested by the so-called *WIMP miracle*. The Higgs portal appears then as a *minimal* and appealing possibility as well. Although the Higgs boson has stronger couplings to the heavier SM particles (*i.e.*, to itself, the top quark and the weak gauge bosons), it also admits large Yukawa couplings with the active neutrinos in the presence of heavy Dirac neutrinos. These couplings introduce heavy-light mixings that can be sizeable ($s_\alpha \approx 0.1$) and are actually required if the origin of neutrino masses is an inverse see-saw scenario at the TeV scale.

In this chapter of the thesis we have analysed such a WIMP scenario: a Majorana fermion interacting through the Higgs portal in a model extended with a heavy Dirac neutrino. First we show that, although the WIMP interactions are all spin independent and are thus severely constrained by direct searches, the model *naturally* implies the observed relic abundance while respecting the current bounds. The question is then whether such a constrained model may provide *any* signal in indirect or collider searches at all.

For the neutrino signal from DM annihilation in the Sun, in particular, the same spin independent elastic cross section probed in direct searches also dictates the capture rate by the Sun. In addition, CRs reaching the solar surface produce the irreducible background of high energy neutrinos studied in the previous chapter that define a floor in DM searches. In particular, we have shown that a capture rate consistent with the current XENON1T bounds implies a neutrino flux from DM annihilations into $\tau^+\tau^-$, $b\bar{b}$ or W^+W^- already below this floor.

The model proposed here, however, is *neutrinophilic*. Most important, it includes an annihilation channel $\chi\chi \to \nu N$ that produces monochromatic neutrinos and can be probed at telescopes. The search there for the astrophysical signal from CRs showering in the solar surface may then also reveal this type of DM signal.

The scenario could also have interesting implications at colliders [121, 122, 123], specially if the heavy neutrino in the model is lighter than the Higgs boson. At the LHC, the decays $h \to N\nu$ with $N \to \ell W$ (with ℓ mostly the τ but possibly also the lighter charged leptons) or $N \to \nu Z$ would appear as a background in $h \to WW^*, ZZ^*$ searches, where 10% deviations are still experimentally allowed [117, 118].

In summary, although the WIMP is a DM candidate certainly constrained by direct searches, we think that the presence of heavy Dirac neutrinos at the TeV scale preserves all the reasons why it is such a phenomenologically interesting scenario.

Part II

Search for Dark Matter with the KM3NeT/ORCA6 data

4

The KM3NeT neutrino telescope

> We are just an advanced breed of monkeys on a minor planet of a very average star. But we can understand the universe. That makes us something very special.
>
> Stephen Hawking.

The Kilometre Cubic Neutrino Telescope (KM3NeT) is a new generation research infrastructure located in the dephts of the Mediterranean sea. Being the heir of the ANTARES neutrino telescope, it aims at opening a new perspective of the universe while also making significant contributions to the study of neutrino properties.

The KM3NeT/ARCA (*Astroparticle Research with Cosmics in the Abyss*) telescope is optimised for the quest of detecting neutrinos originating from remote astrophysical sources, such as supernovae, gamma ray bursts or colliding stars. On the other hand, the KM3NeT/ORCA (*Oscillation Research with Cosmics in the Abyss*) telescope will serve for investigating neutrino properties, using neutrinos produced in atmospheric air showers. KM3NeT is also used for a very ambitious physics research program: multimessenger, DM, nuclearities or magnetic monopoles are among the searches being held by the collaboration.

In this section, the KM3NeT neutrino telescope will be described, including both physical and technical aspects (Sec. §4.1), with a brief description of the Monte Carlo production (Sec. §4.2) and the framework used in the reconstruction of the events (Sec. §4.3).

Figure 4.1: Main facilities of the KM3NeT Research Infrastructure. The KM3NeT-Fr and the KM3NeT-It sites are the locations of the ORCA and ARCA detectors, while the KM3NeT-GR site is the location of the third detector that was planned. The data centre and the headquarters are also shown. From KM3NeT homepage [124].

4.1 Detector description

The KM3NeT neutrino telescope, currently under construction [84], is located 2.5 to 3.5 km undersea. It is composed of two different detectors: KM3NeT/ORCA, located off-shore Toulon (France), and KM3NeT/ARCA, located off-shore Capo Passero (Italy). A third location in Pylos (Greece) was considered as well – but it was finally discarded. Fig. 4.1 shows the three locations described above (also known as KM3NeT-Fr, KM3NeT-It and KM3NeT-Gr, respectively), as well as the data centre in Lyon (also mentioned as KM3NeT-Data Centre) and the headquarters (KM3NeT-HQ) in Amsterdam. Fig. 4.2 shows the location of all the KM3NeT sites.

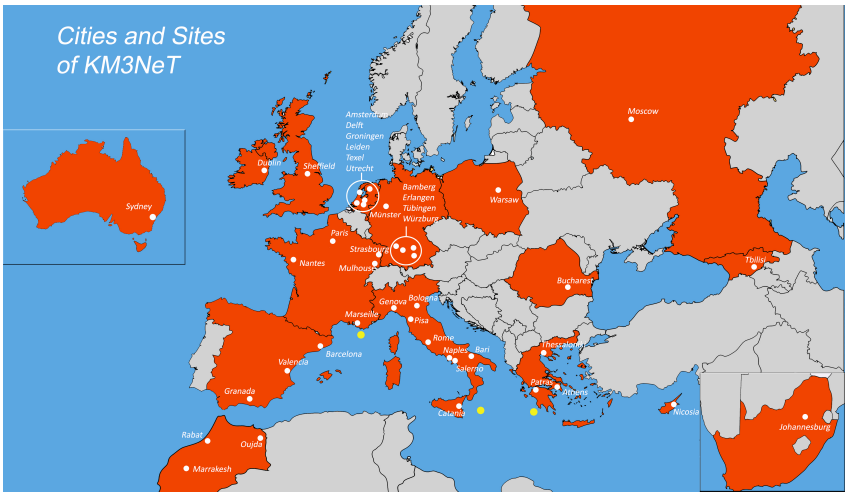

Figure 4.2: Complete map of KM3NeT sites. The white dots represent the cities in which a KM3NeT team is located. The yellow dots represent the KM3NeT-Fr, KM3NeT-It and KM3NeT-Gr sites. From KM3NeT homepage [124].

The deployment of the KM3NeT detector is splitted in phases:

- The **Preparatory Phase**, funded by the European Seventh Framework Programme (EU FP7). The primary aim of this phase was to facilitate the journey towards political and scientific convergence regarding the legal, governance, financial engineering, and siting aspects of the infrastructure, and to be ready for swift and efficient construction once approval was granted.
- The **Phase-1** of construction begun in 2013 at the KM3NeT-Fr and KM3NeT-It sites. The aim of this phase was to achieve a size of $\sim 0.1\,\mathrm{km}^3$, which would lead to the first science results. The estimated cost of this phase was $\sim 31\mathrm{M}\,€$.
- The **Phase-2.0** of construction started on 2017 and it consists on the deployment of two *building blocks* of 115 Detection Units (DUs) each for the ARCA detector and one building block of 115 DUs for the ORCA detector. With an estimated cost of $\sim 125\mathrm{M}\,€$, it is expected to achieve a size between $1\,\mathrm{km}^3$ and $1.6\,\mathrm{km}^3$ during this phase.
- The **Phase-3** (not founded yet) will consist on doubling the number of building blocks, from 3 to 6. The estimated cost for this phase is $\sim 250\mathrm{M}\,€$.

Even though the detector is still under construction, several studies are ongoing or have been already completed using the data recorded by ORCA and ARCA with the

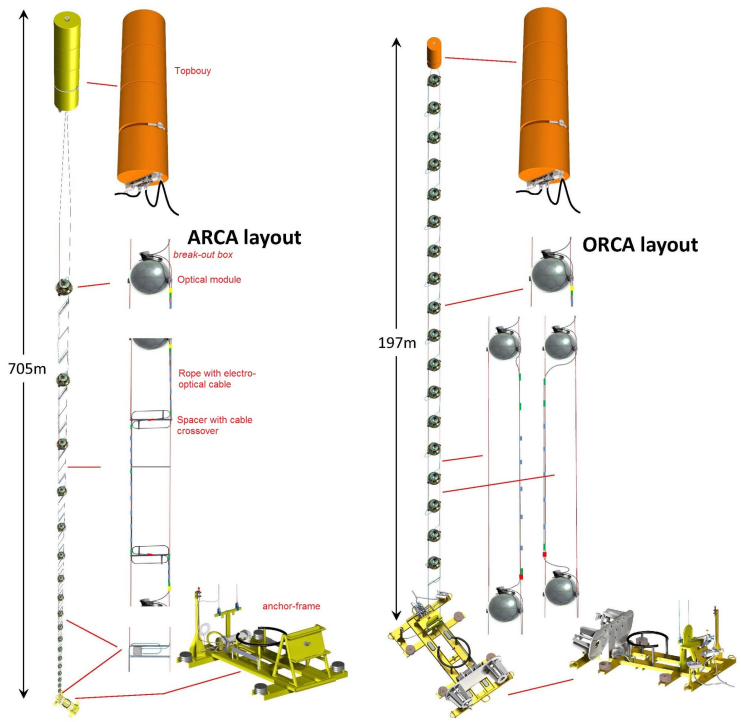

Figure 4.3: Artistic representation of an ARCA Detection Unit (left) and an ORCA Detection Unit (right). The main difference between both configurations lies in the distance between DOMs, which leads to a higher length in the case of the ARCA DUs. From KM3NeT homepage [124].

DUs deployed since 2017. The results of such analyses have been already published in Journals and presented in international conferences, as the ICRC 2023 [125] among others.

The detection units (see Fig. 4.3), also called *strings* or *lines*, are formed by 18 Digital Optical Modules (DOMs), each DOM containing 31 Photo-Multiplier Tubes (PMTs) (see Sec. §4.1 for additional details). These PMTs detect the Cherenkov light emitted by particles produced in neutrino interactions. The use of these independent lines allows the election of different configurations, as the distance between DOMs and lines can be changed, affecting the resolution and other properties of the detectors. ORCA and ARCA share the same technology, and differ on the physical location and on the geometry (vertical distance between DOMs and horizontal spacing between DUs):

- The **ORCA** detector is located at a depth of $\sim$ 2500 m, off-shore Toulon (coordinates 42°41' N, 6°02' E). The ORCA DUs are 200 m long, with a distance of about 20 m between strings. The distance between DOMs inside a string is 9 m. Therefore, the expected volume for the full configuration of the ORCA detector is $\sim 5 \times 10^{-3}\,\mathrm{km}^3$. ORCA is optimised for the detection of neutrinos with energies between 1 GeV to 10 TeV.
- The **ARCA** detector is located at a depth of $\sim$ 3500 m, off-shore Capo Passero (coordinates 36°16' N, 16 °06' E). The ARCA DUs are 700 m long, with a distance of about 95 m between strings. The distance between DOMs inside a string is 36 m. Therefore, the expected volume for the full configuration of the ARCA detector is $\sim 1\,\mathrm{km}^3$. ARCA is optimised for the detection of neutrinos with energies between 100 GeV to 10^3 TeV.

Fig. 4.4 shows a comparison between the topology (footprint) of both detectors, while Fig. 4.5 shows an artistic concept of the KM3NeT detector once finished.

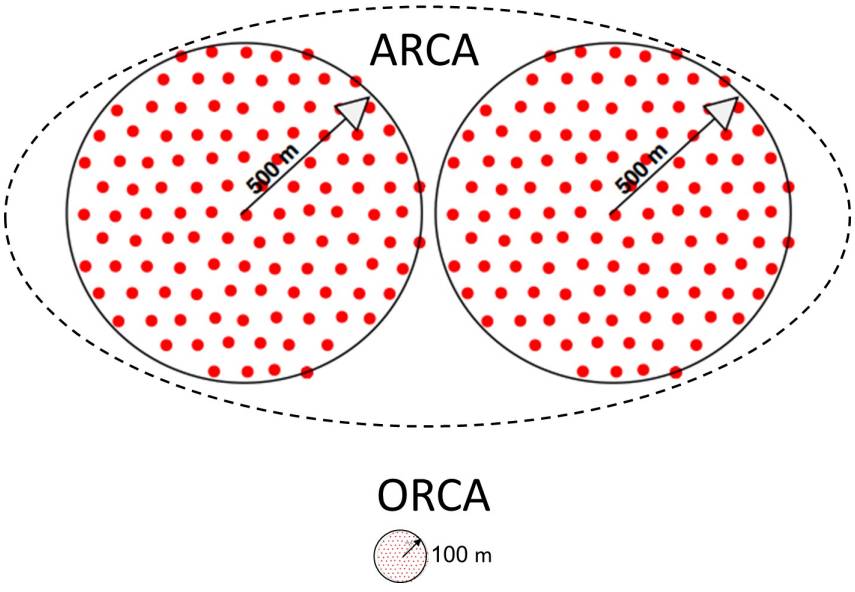

Figure 4.4: Size comparison between the full configuration of the ARCA (top, with two building blocks) and ORCA (bottom, with one building block) detectors. From KM3NeT homepage [124].

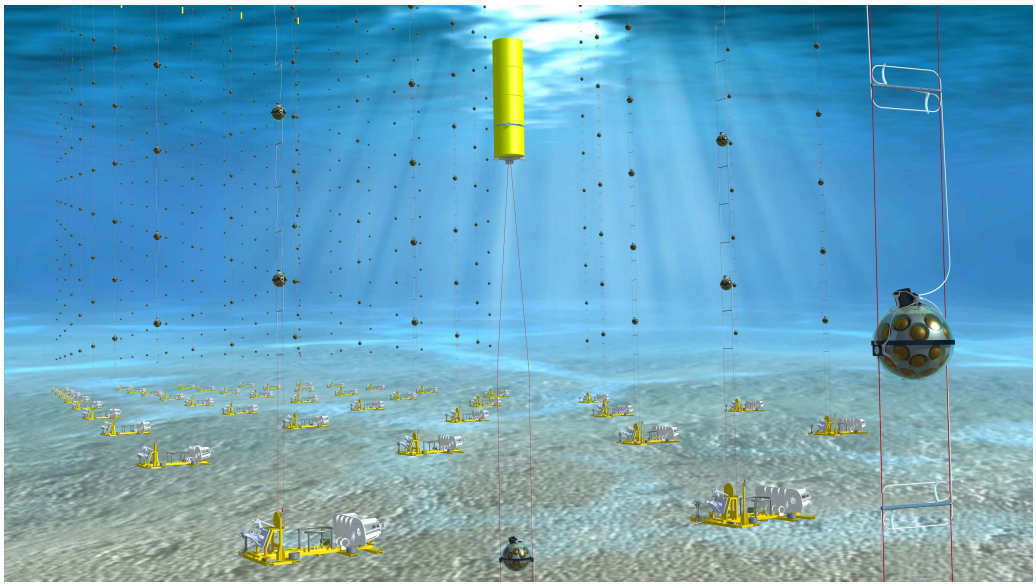

Figure 4.5: Artistic concept of the KM3NeT detector. From KM3NeT homepage [124].

Digital Optical Modules

As described in the previous section, the DOM [126] is the fundamental element of KM3NeT, being able to detect the Cherenkov light emitted by particles produced in neutrino interactions thanks to the PMTs integrated in it. The DOM is a glass sphere of $\sim 40\,\text{cm}$ diameter. Each sphere contains 31 PMTs [127] with a size of 3" ($\sim 7.26\,\text{cm}$) each. The PMTs are arranged in two hemispheres (top and bottom). The bottom hemisphere includes three rings of 6 PMTs each, and an additional single PMT pointing vertically downwards. On the other hand, the top hemisphere contains only two rings of 6 PMTs each. The difference in the number of PMTs between the two hemispheres is explained by an area without PMTs in the top hemisphere called *the mushroom*, whose function is to avoid the deposition of sediments coming from the surface of the sea.

The multi-PMT design provides several advantages: the angular coverage is almost isotropical, the information on the number of photons (by comparing the trigger of a PMT with the hits registered by his neighbours), a good separation between single events and multiple events, and information on the photon direction [128]. Further specifications on the PMTs is given in Table 4.1.

A layer of gel is applied between the PMTs and the glass sphere in order to ensure the thermal conduction of the heat produced by the internal components of the

Radiant blue sensitivity at 404 nm	130 mA W^{-1}
Quantum efficiency (QE)	20% at 470 nm and 28% at 404 nm
Inhomogeneity of cathode response	10%
Supply voltage for a gain of 3×10^6	900–1300 V
Dark count at 15°C and 0.3 photo-electron threshold	1.5 kHz
Transit time spread (TTS)	4.5 ns (FWHM)
Peak to valley ratio	2.5

Table 4.1: Technical specifications of the PMTs. Two models of PMTs are used with the required specifications: the EDEL D792KFL and the Hamatsu R12199-02.

Figure 4.6: Picture of a KM3NeT Digital Optical Module mounted (left) and dismounted (centre), and drawing of a DOM components (right). From KM3NeT homepage [124].

DOMs. In addition, the refractive index of the glass is closer to that of the gel than to that of air, thereby minimizing the refraction suffered by the light when travels from the glass to the medium.

In addition to the PMTs, the DOMs contain three calibration sensors: a) a LED nano-beacon; b) a compass and a tilt-meter used for orientation calibration; and c) an acoustic sensor used for orientation calibration. Fig. 4.6 shows photos of a Digital Optical Module, as well as a picture of its internal structure.

Fibre-optic data transmission system

The KM3NeT fibre-optic data transmission system accomplishes the following functions:

i. **Transfers data collected by the DOMs to shore** with bandwith of 1 Gb s^{-1} per DOM. The contribution of the ^{40}K is about $9 - 12$ Mb s^{-1}, and the bioluminiscence can contribute with a factor of almost 10 compared to the ^{40}K [129, 130].

ii. **Ensures timing stabilization**. Typically, the relative time offsets between any pair of DOMs is ~ 1 ns.

iii. Provides **slow control for the junction boxes.**

iv. Provides **individual control for each base of a DU**.

v. Provides **individual control for each DOM**.

The communication between DOMs and offshore lies on a dense wavelength division multiplexing technique. In each DU, a frequency is assigned to each DOM, with a distance of 200 GHz between one DOM and the next one. In addition, each DOM is assigned to a class: A, B, C or D. The frequency associated to the first DOM of the array depends on the DU class: for each class, the initial frequency is 50 GHz greater than for the previous one. Therefore, the frequency assigned to a DOM is expressed as

$$f = f_0 + i \cdot 50 + j \cdot 200\,(\text{GHz}), \tag{4.1}$$

where f_0 is the initial frequency of the set, $i = 0, 1, 2, 3$ represents the class (A, B, C, D) of the DU and $j = 0, 1, ..., 17$ is the number of the DOM in the DU.

Therefore, one single fibre can manage the signal of a group of 4 DUs (one per class). All the 4×18 signals are mixed together in the fibre by a multiplexer and sent offshore, where they are splitted again by a second multiplexer.

Data acquisition

The Data-acquisition (DAQ) system employed by the KM3NeT detector [131] lies on the *all-data-to-shore* concept. In this approach, all analogue signals exceeding a threshold (usually 0.3 photo-electrons) from the PMTs are digitised, and the resulting digital data transmitted onshore for real-time processing. In order to deal with the overwhelming background – the contribution to the photon flux arriving on the PMTs is utterly dominated by the ^{40}K and the bioluminiscence by a factor of $O(10^7)$, regarding the photons coming from neutrino interactions – specialised software is used to separate physics events from background noise.

The optical data includes the time information for the leading edge and the Time-over-Threshold (ToT) values of each analogue pulse, commonly known as a *hit*. The size of the information of a hit is 6 B: 1 B of information about the PMT that registered the hit, 4 B for the time and 1 B for the ToT. In addition, summary data capturing the single rates of all PMTs in the detector is stored with a frequency of 10 Hz. This information plays a crucial role in the simulation and reconstruction processes, allowing for the consideration of the real-time status and optical background conditions of the detector.

In addition to the optical data, the information from the acoustics positioning system is processed, constituting a data volume approximately one-third of that associated with the optical data.

4.2 Monte Carlo simulations

Many tools available for the KM3NeT Monte Carlo (MC) production were inherited from the ANTARES collaboration [132]. However, these tools were never meant to be used in a large scale detector, so they had to be adapted to the KM3NeT machinery. In addition to the scale issue, some ANTARES tools were hard to mantain due to the fact that they were FORTRAN-based, and some of them were found to be problematic when running in a 64-bit architecture. For these reasons, a significant effort was made to adapt the MC production chain to the KM3NeT project.

Some of the new tools used by the KM3NeT collaboration are already used by other experiments, such as the IceCube neutrino telescope. As an example, the *ANIS* neutrino generator [133], the *CORSIKA* air shower MC code [57] and the *MMC* lepton propagator [134] are found among the software incorporated to the KM3NeT MC chain. However, there are also brand-new tools developed specifically for the KM3NeT neutrino telescope:

- A GEANT4-based particle propagator.
- A LUT-based light propagator.
- An Optical Module simulation tool.
- A Photo-multiplier simulation tool.
- A track reconstruction tool.

Fig. 4.7 shows a schematic drawing of the KM3NeT MC simulation chain. The three first stages of the process are often paired together due to the fact that some of the tools used for the event generation also include resources for the particle propagation and interactions. The resulting generation stage is described in Sec. §4.2. After the interactions nearby the detector are simulated, the light production is generated following the process explained in §4.2. The detector response is simulated from the data production following Sec. §4.2. Finally, the events are reconstructed from the information obtained by the detectors following Sec. §4.3.

Event generation

There are up to five generator tools available for the MC production:

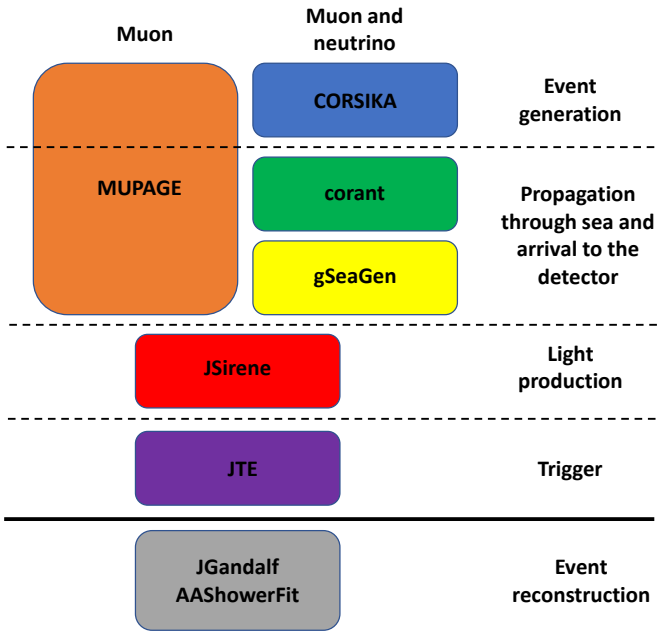

Figure 4.7: Representation of the MC chain in the KM3NeT neutrino telescope. The procedure is divided into 5 steps: the generation of neutrinos and muons, their propagation through the sea and their arrival to the detector, the light production by the muon particles and EM showers, the detector trigger, and, finally, the event reconstruction stage.

i. **MUPAGE** [135]. This acronym stands for *atmospheric MUons from PArametric formulas: a fast GEnerator for neutrino telescopes*. Being able to generate atmospheric muon bundle events in underwater or ice neutrino telescopes, it is the tool used for the muon MC production. The kinematics of each event is generated using a user-defined cylinder surrounding the detector volume.

ii. **CORSIKA** [57] (*COsmic Ray SImulations for KAscade*). This software is a complete MC air shower generator. Being able to select a wide variety of primary particles, the software simulates the interactions and development of the atmospheric cascade. The software package lies on several simulators in order to perform the hadronic interactions, as VENUS [136], QGSJET [137], and DPMJET [138] for high energy interactions or GHEISHA [139], FLUKA [140] or UrQMD [141] for low energy interactions. The electromagnetic interactions are carried out by the EGS4 package [142] and by the analytical NKG formulas.

iii. **GENHEN** [143] (*GENerator of High Energy Neutrinos*). An alternative to the

external tool ANIS, GENHEN is an neutrino event simulator developed for the ANTARES collaboration. The energy range of the neutrino events simulated by GENHEN goes from 10 GeV to 10^9 GeV.

iv. **gSeaGen** [144]. A GENIE-based code developed to generate high statistics samples of events induced by neutrino interactions. It is able to induce track-like and shower-like events of all the three neutrino flavours.

v. **KM3BUU** [145]. This neutrino event generator lies on the Boltzmann-Uehling-Uhlenbeck equation to compute the particle flow.

These tools are used not only for particle generation, but also to propagate the particle fluxes through the Earth and to generate interactions near the detector.

Light generation

A set of tools is available to produce light from particles near the detector, propagate this light through the water and, finally, simulate the hits on the PMTs:

i. **KM3** [146]. This package, inherited from ANTARES, takes the geometry of the detector, the initial particles (muon+neutrino) and the hit histograms as an input, and computes the muon tracks and the electromagnetic showers that result from this initial particles. This software does not compute hadronic showers.

ii. **KM3Sim**. Part of the *Hellenic Open University Reconstruction Simulation* (HOURS) package [147], this package simulates the response of the underwater Cherenkov detectors. By using the GEANT4 toolkit [148], the KM3Sim software generates Cherenkov light emission, tracks the photons in the sea water and simulates their detection taking into account the KM3NeT PMT and DOM properties: the photocatode area, quantum efficiency and angular acceptance of the PMT and the transmission of light in the glass and gel of the DOM.

iii. **JSirene** [149]. This package lies on tabulated Probability Density Functions (PDFs) of the arrival time of light and the interpolation methods that are part of the Jpp package [150, 151] to simulate the detector response to Cherenkov light produced by muons, taus and electromagnetic showers.

iv. **OMGSim** [152]. This GEANT4-based package provides a detailed simulation of the KM3NeT DOM, allowing the study of its response in sea water. It is

designed mainly for the calibration of the DOM based on the characterization of the radioactive background.

Detector response

Once the emitted photons are generated, the simulated hits in the DOMs have to be converted into a signal readable by the DAQ system. For this reason, the Monte Carlo hit is converted into a DAQ signal together with the simulated background coming from ^{40}K and bioluminescence. The data filtering is applied to the simulated data. This process is performed by the ROOT-based KM3NeT software Jpp.

During the simulation of atmospheric muons or neutrino interactions, the optical background is generated based on fixed rates of single hits and coincidences. An optional *run-by-run* simulation can be executed. In this process, summary slice data from a run file is randomly selected to emulate realistic data-taking conditions for each triggered input event. The individual PMT counting rates are used to model the optical background, and non-functional PMTs are not taken into account based on information from the detector description file.

Finally, the resulting data is processed by the same algorithms applied to the real data [153].

4.3 Event reconstruction

The last step in the simulation chain is to reconstruct the events registered by the DAQ system. The information available for each hit (which includes, among others, the charge, the photon arrival time or the PMT position) is used to recover the properties of its parent neutrino. In this section, the algorithm applied for the reconstruction of *track-like* events in the ORCA detector is described [154, 155]. A detailed description of *shower-like* events is provided in Ref. [35].

Track Reconstruction

A muon produced nearby the detector with an energy above $\sim 100\,\text{GeV}$ is able to cross the whole detector. Using the fact that this muon is produced in a direction that is almost colinear with its parent neutrino, the reconstruction of the muon provides information about the charged current (CC) neutrino event that produced the muon. To characterise the muon track, the position of the muon at a given time, the direction of the track – given by the zenith and the azimuth angles –, the arrival time and the position of the hits along its trajectory are needed.

The reconstruction is performed via the JGandalf algorithm. This method lies in the maximization of a **track likelihood function**:

$$\mathcal{L} = \sum_{i=1}^{N_{hits}} \left[\frac{\partial P(\rho_i, \phi_i, \theta_i, t_{res})}{\partial t} \right]. \tag{4.2}$$

The maximization is applied over the hits in the PMTs that are selected by the filters applied in the algorithm. The PDF function, P, depends on the minimum distance of the muon to the i-th PMT (ρ_i), the azimuth (ϕ_i) and zenith (θ_i) of the PMT and the time residual of the hit (t_{res}). The maximization of the likelihood function (Eq. (4.2)) provides the reconstructed vertex of the CC interaction and the muon trajectory [155], together with an estimation of the error in the reconstruction of the track direction, β.

As an example, Fig. 4.8 shows the expected median of the angular error in the reconstruction of the events in the ORCA detector (115 lines).

Energy reconstruction

The neutrino energy reconstruction depends on the position of the interaction vertex. If the neutrino interacts inside the detector, both the energy lost by the track of

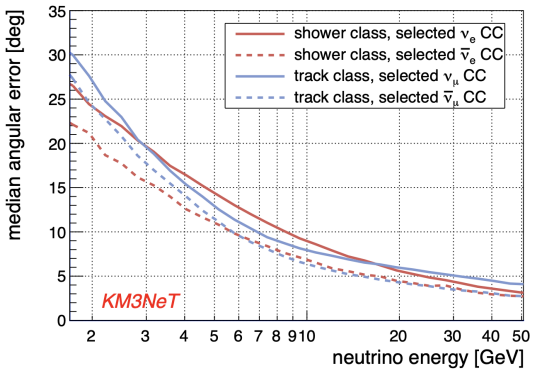

Figure 4.8: Median angular error as a function of the neutrino energy for the full KM3NeT/ORCA detector (expected from MC simulations). From Ref. [156].

the muon and the energy deposited by the induced hadronic shower are used for the reconstruction. However, when the neutrino interacts outside the detector, the hadronic shower is typically absorbed before the produced photons reach the PMTs. In this case, only the energy deposited by the muon is used in the reconstruction, leading to a less reliable result.

As described in Sec. §1.3, the parametrization of the energy lost by the muon in its path along the detector is given by Eq. (1.7), including the ionization, and the stochastic processes: bremsstrahlung, e^+e^- pair production, and photonuclear interactions.

The reconstruction of the neutrino energy is divided into two different steps. In the first step, an estimation of the muon energy is made by reconstructing the muon track length and the interaction vertex. To obtain the muon track length, the distance between the first and last DOM in the track is calculated. The number of hits is obtained as well by integrating the PDF (P) over a time ∂t. In case that the vertex of the neutrino interaction is found inside the detector, the integral accounts for the hits corresponding to the muon track and the hadronic shower produced in the neutrino interaction. Otherwise, only the muon track is included in the integral.

In the second step, the energy of the neutrino is related to the number of hits used in the reconstruction in a certain part of the muon track by fitting the median distribution of the neutrino energy as a function of N_{hits} [157]. In case the vertex is reconstructed outside the detector, the energy of the reconstructed neutrino is increased in order to compensate the fact that the information of the hadronic shower is missing. Fig. 4.9 shows the reconstructed energy of the events in KM3NeT/ORCA

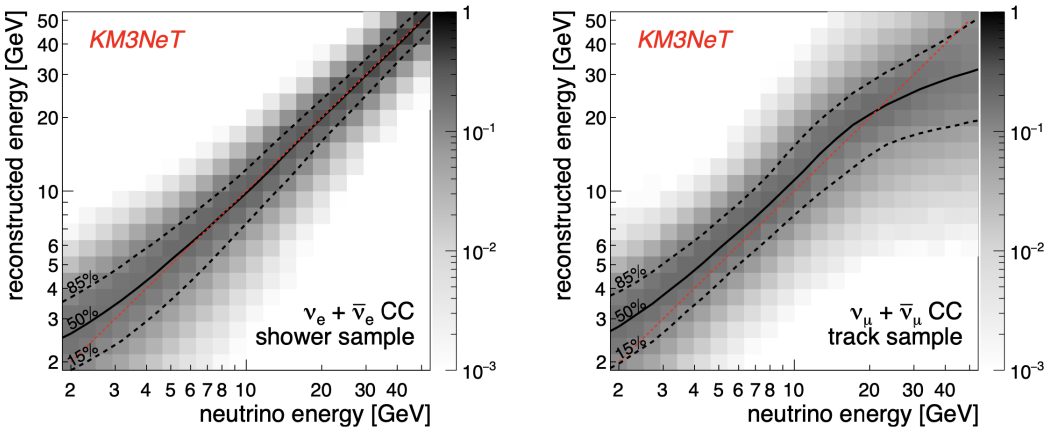

Figure 4.9: Energy reconstruction as a function of the true neutrino energy for the full KM3NeT/ORCA Monte Carlo production for $\nu_e + \bar{\nu}_e$ charged current events classified as shower-like events (left) and $\nu_\mu + \bar{\nu}_\mu$ charged current events classified as track-like events (right). The red line indicates the perfect reconstruction. From Ref. [156].

(115 lines) as a function of the true energy of the events for a shower-like and a track-like sample. The reconstruction of the shower sample is more accurate than the reconstruction of the track sample due to the fact that showers are typically absorbed within a few metres in water, while muons can fly much longer distances before being absorbed. Therefore, while almost all shower-like events are produced inside the detector or in its proximity, a significant part of track-like events may occur far from the detector, and, consequently, in these track-like events the information corresponding to the hadronic shower generated in the event is missing, worsening the energy estimation.

5

Indirect search for a DM signal with ORCA

> All my life I have pursued the mysteries of science, only to discover that it is better to leave some unresolved.
>
> Anonymous.

With an energy threshold of ~ 1 GeV, the KM3NeT/ORCA detector is optimised for the study of atmospheric neutrinos. ORCA may contribute to address two fundamental questions: the measurement of the neutrino oscillation parameters and the Neutrino Mass Ordering (NMO). Additionally, the experiment can be used in the search for neutrinos from SN explosions and other point-like sources.

In addition, The ORCA detector can also be used to look for the neutrinos produced in WIMP-pair annihilations. This signal may be expected from several astrophysical sources, including the Sun and the Galactic Center (GC): the large mass of the GC and the proximity of the Sun to the Earth make them the preferred candidates for DM searches [84]. In particular, the energy range $E_\nu < 1$ TeV explored at ORCA seems adequate for DM serches from the Sun, as at higher energies neutrinos tend to be absorbed before they escape the solar medium.

In this chapter, we discuss the search for a DM annihilation signal coming from the Sun. In Sec. §5.1 we introduce several simplified DM models that are usually considered in experimental searches – we leave for future work the analysis of the DM model proposed in the first part of the thesis. Then in Sec. §5.2 we describe the criteria used in the event selection, and in Sec. §5.3 we present the analysis of the data and the results obtained.

5.1 Dark matter model

In this analysis we select three simplified DM models that are usual in experimental searches. It is assumed that the model is able to reach the stationary regime with the annihilation rate equal to half the capture rate (see discussion in Chap. §3), and then each model is defined by a given channel in all the WIMP-pair annihilation. Namely, we consider the possibility that the DM annihilates into $b\bar{b}$, $\tau^+\tau^-$ or W^+W^-.

We will use the WimpSim package [158] to estimate the neutrino yield for each model, *i.e.*, the number of neutrinos at 1 Astronomic Unit (AU) per unit of energy that are produced in one WIMP-pair annihilation. Then we use DarkSUSY [159] to establish the bounds on the cross section implied by those yields. The package, that relies in other simulation codes like Pythia [160] and Nusigma [161], provides effects like the absorption of neutrinos by the Sun or their flavor oscillations in their way to the Earth. More specifically, the scheme includes

- **Input selection**:
  - The *dark matter density* around the Solar System, $\rho = 0.3\,\mathrm{GeV/cm}^3$ [162].
  - The *halo profile model*. The NFW model [163] is used in this thesis.
  - The *velocity distribution* for the DM particles. For the galactic halo, a Maxwellian velocity distribution with a mean of 220 km/s is typically used. However, in the vicinity of the Sun, the gravitational attraction modifies the DM velocity, leading to a Maxwellian distribution with a mean of 270 km/s [164].
  - The *solar density profile*. In this analysis, the Standard Solar Model is used.
  - The *neutrino oscillation and neutrino mass parameters*. The world best-fit values are used (see Eq. (1.5) in Sec. §1.2 for additional details).
- **WIMP-WIMP annihilation process**. As mentioned, we use simple models with just one annihilation mode: quark, lepton or gauge boson pairs. The package uses Pythia to simulate the collision, hadronization and/or decay of all the particles produced, and the final result of this process is the flux of neutrinos produced in one annihilation.
- **Neutrino propagation throught the Sun**. Neutrinos may then interact with the solar medium in their way to the Earth. Neutral current (NC) interactions result in an energy loss by the neutrino. Charged current (CC) interactions

WIMP-pair annihilation channels	$\tau^+\tau^-$ and $b\bar{b}$	W^+W^-
Lowest mass	10 GeV	90 GeV
Highest mass	10 TeV	10 TeV
Number of explored masses	37	30

Table 5.1: WIMP masses and annihilation channels explored in this analysis.

are flavour-dependent: ν_τ CC interactions produce a τ lepton that will decay in a secondary ν_τ, while ν_μ and ν_e CC interactions result in the neutrino disappearance. All of these processes are performed by Pythia and the Nusigma package.

- **Neutrino propagation in space to Earth**. Once neutrinos leave the solar medium, the WimpSim package propagates them to the Earth, including the oscillations to other flavours.

Further information about the WimpSim code can be found in [158, 159, 160, 161, 165]. Table 5.1 shows the details of WIMP masses and annihilation channels explored in this analysis.

Fig. 5.1 shows, as an example, the number of muon neutrinos per unit of energy at 1 AU per WIMP-pair annihilation (*i.e.*, the *neutrino yield* or *neutrino spectra*) for the three WIMP-pair annihilation channels and a WIMP mass of 100 GeV and 1 TeV. Fig. 5.2 illustrates the neutrino and antineutrino yield for the $\tau^+\tau^-$ annihilation channel for a WIMP mass of 100 GeV, 1 TeV and 10 TeV.

In order to calibrate the efficiency of a DM model to produce a neutrino signal, the yield is commonly expressed in the literature in units of $Z = E/m_{DM}$ instead of E. These yields are just

$$\frac{\mathrm{d}N}{\mathrm{d}Z} = m_{DM}\frac{\mathrm{d}N}{\mathrm{d}E}. \tag{5.1}$$

Fig. 5.3 shows the number of neutrinos per unit of Z at 1 AU produced in one WIMP-pair annihilation ($\tau^+\tau^-$ channel) for WIMP masses of 10 GeV, 100 GeV, 1 TeV and 10 TeV. The spectra of the high masses go to 0 at lower values of Z due two main reasons. The first reason is that very high-energy pions and kaons do not decay inside the Sun, leading to a drop in the neutrino production. The second reason is that, although a fraction of them may decay, the neutrinos produced with energy greater than ~ 2 TeV are absorbed in their way out [31].

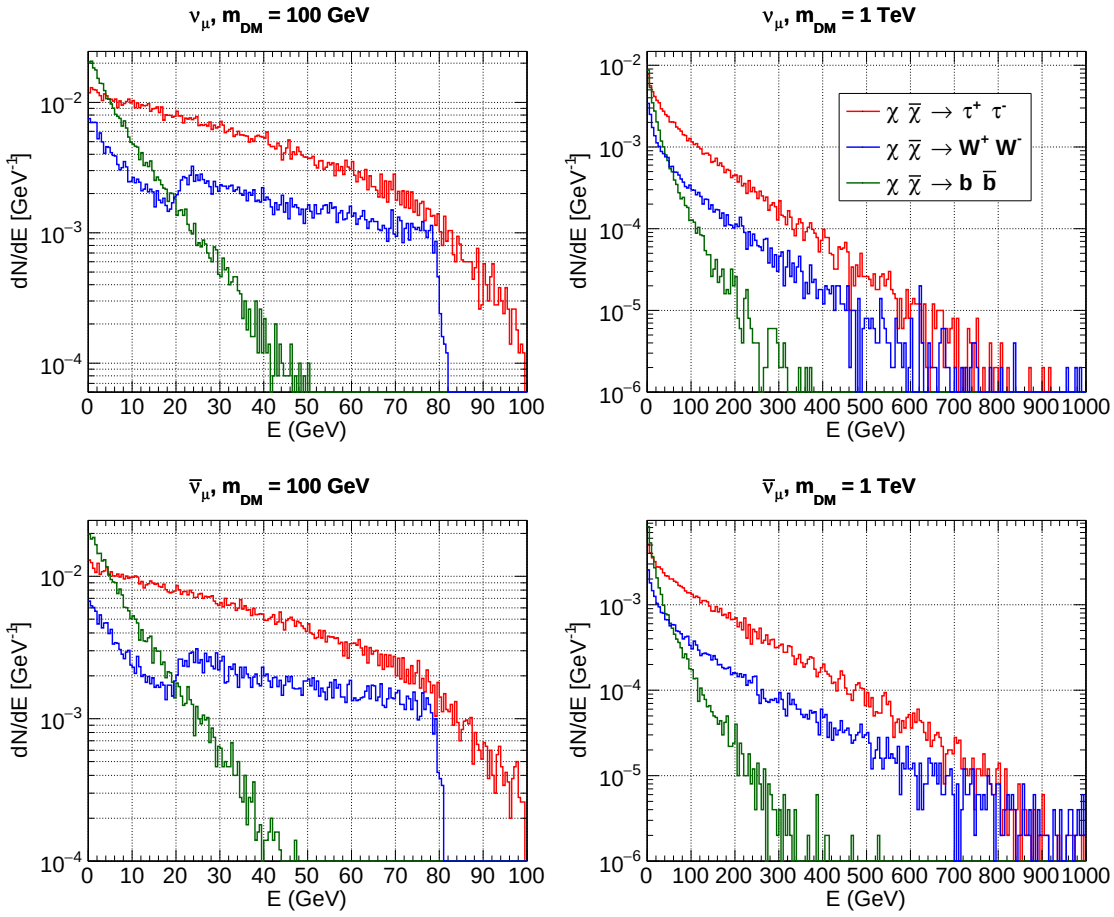

Figure 5.1: Neutrino (top) and antineutrino (bottom) WIMP-pair annihilation spectra ($\mathrm{d}N/\mathrm{d}E$) for the $\tau^+\tau^-$, W^+W^- and $b\bar{b}$ channels. The spectra are shown for a WIMP mass of 100 GeV (left) and 1 TeV (right) at 1 AU from the Sun.

5.2 Event selection

In this thesis we analyse the data obtained by the KM3NeT/ORCA detector in the 6 DUs configuration (ORCA6 hereafter). The data sample has a total livetime of 543 days, from 26/01/2020 to 18/11/2021, with a total of $\sim$ 119 days of data taking rejected due to technical issues, and our objective is the detection of high energy neutrinos coming from WIMP-pair annihilations in the Sun.

In order to reduce the number of misresconstructed events and the contamination from atmospheric muons in the sample, we apply the following set of selection cuts:

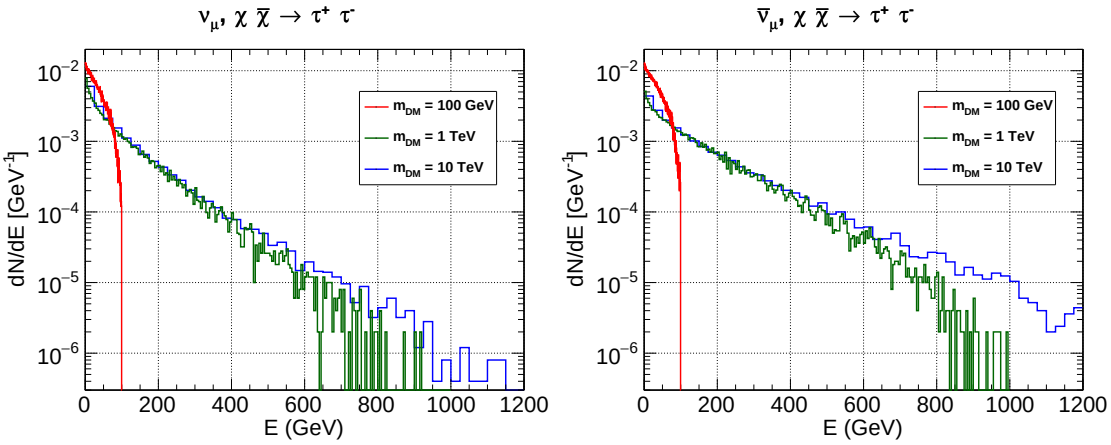

Figure 5.2: Neutrino (left) and antineutrino (right) WIMP-pair annihilation spectra ($\mathrm{d}N/\mathrm{d}E$) for the $\tau^+\tau^-$ annihilation channel and several WIMP masses at 1 AU from the Sun.

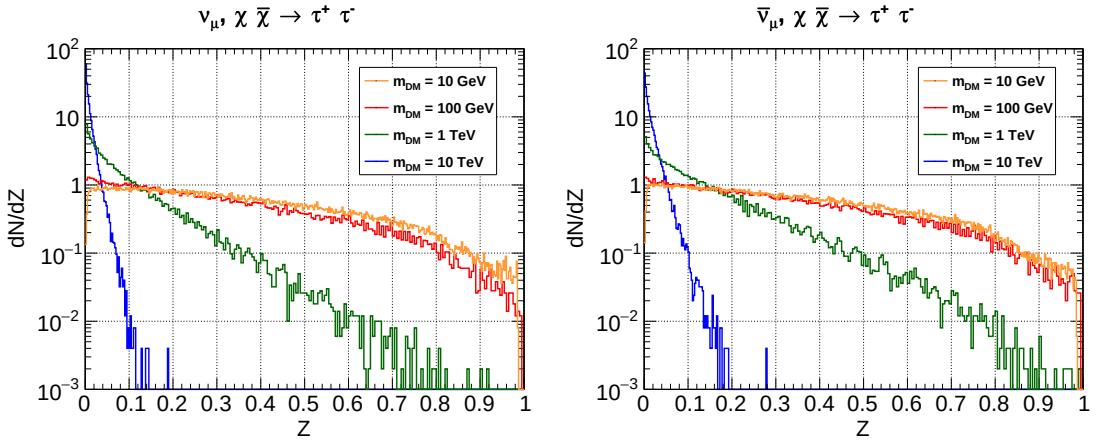

Figure 5.3: Neutrino (left) and antineutrino (right) WIMP-pair annihilation spectra ($\mathrm{d}N/\mathrm{d}Z$) for the $\tau^+\tau^-$ annihilation channel and several WIMP masses at 1 AU from the Sun.

i. **Basic cuts**

   a) **Maximum ToT among trigger hits < 250 ns**. This cut removes the spark events from the sample.

   b) **Upgoing cut**. Atmospheric downgoing muons can reach the detector and be reconstructed as downgoing tracks. To avoid this muon contamination, upgoing ($\theta_{zenith} > 90°$) events are selected.

   c) **Likelihood of the reconstructed track > 40**. This quality cut in the reconstruction removes pure noise events from the sample.

ii. **Agreement between hits time/position and reconstructed track hypothesis**

   a) **Number of early trigger hits < 6 hits.** An excess in the number of triggers in a very small fraction of time is often a consequence of a misreconstruction.

   b) **Number of DOMs with Cherenkov condition ≥ 8**. An event activating a smaller number of DOMs may produce an unclear signal, potentially leading to errors in its reconstruction.

iii. **Track quality**

   a) **Likelihood over the number of hits used in the reconstruction > 2**. Atmospheric muons typically have a lower likelihood per number of hits.

   b) **Likelihood difference between best upgoing and best downgoing reco > 40**, to remove ambiguous reconstructions.

   c) **Likelihood > (Vertex radial position − 30) · 5.6 + 60**. This relationship has been proved to be very efficient at removing atmospheric muons from the sample.

iv. **Containment cuts**

   a) **Vertex radial position < 60 m**, to define the radius in which the event vertex is accepted.

   b) **Trigger hits mean Z position > 55 m**, to cut the events in the lower part of the detector, where typically atmospheric muons are observed.

WIMP mass range	β	N_{hits}	Track reco. likelihood
10 GeV – 300 GeV	< 1.0	> 20	> 120
300 GeV – 10 TeV	< 1.0	> 20	> 60

Table 5.2: List of cuts that optimise the sensitivity for the $\tau^+\tau^-$ and the W^+W^- annihilation channels.

WIMP mass range	β	N_{hits}	Track reco. likelihood
10 GeV – 300 GeV	< 1.0	> 40	> 120
300 GeV – 10 TeV	< 0.9	> 20	> 80

Table 5.3: List of cuts that optimise the sensitivity for the $b\bar{b}$ annihilation channel.

Annihilation channel	WIMP mass range	Num. Events
$\tau^+\tau^-$	10 GeV – 300 GeV	2239
$\tau^+\tau^-$	300 GeV – 10 TeV	2364
W^+W^-	10 GeV – 300 GeV	2239
W^+W^-	300 GeV – 10 TeV	2364
$b\bar{b}$	10 GeV – 300 GeV	2235
$b\bar{b}$	300 GeV – 10 TeV	2243

Table 5.4: Number of events in the data sample that survive after applying all selection cuts (see Tables 5.2 and 5.3).

c) **Trigger hits mean Z position > vertex position Z**. A trigger below the vertex typically indicates that the reconstruction failed.

A second set of cuts is further applied in order to reduce the atmospheric neutrino contribution and to maximise the sensitivity on the neutrino flux, with cuts that depend on the WIMP mass and channel. In order to obtain the optimal set of cuts, the sensitivity on the neutrino flux is computed for each combination of WIMP mass and annihilation channel, for a different combination of cuts in the β parameter – *i.e.*, the error in the reconstuction of the track direction, described in Sec. §4.3), the number of hits and the track likelihood. The procedure for computing the sensitivity on the flux is described in Sec. §5.3. However, the final results for the chosen set of cuts are shown below since the plots and numbers shown in the following section are

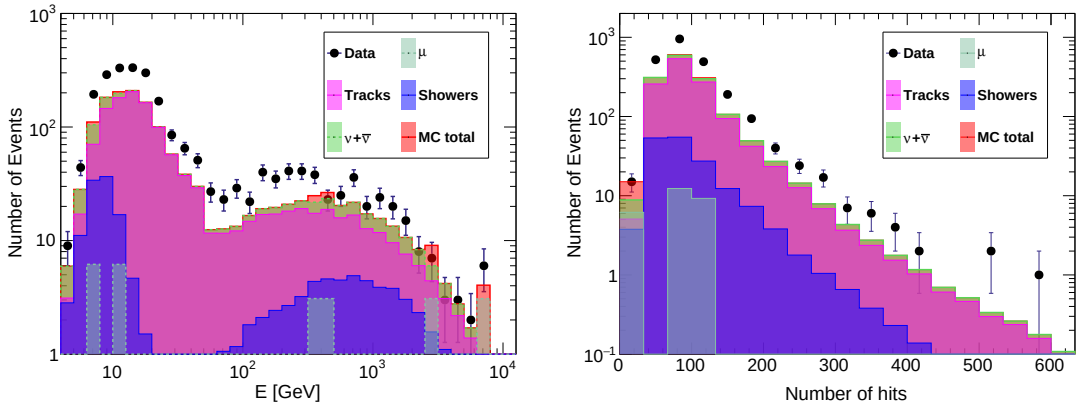

Figure 5.4: Monte Carlo vs data comparison for ORCA6. Left: Reconstructed energy. Right: Number of hits. The set of cuts applied is the corresponding to the low mass group for the $\tau^+\tau^-$ annihilation channel (see Table 5.2).

cut-dependent. Tables 5.2 and 5.3 show the cuts that optimise the sensitivity for the three WIMP-pair annihilation channels considered. Table 5.4 shows the number of events that survive in the data sample after applying the complete set of cuts.

Fig. 5.4 shows the reconstructed energy and number of hits for the Monte Carlo and the data. Although it has been corrected in new versions of the Monte Carlo – which were not yet available when we started this analysis –, the disagreement observed between data and Monte Carlo does not affect our analysis significatively, since we don't weight Monte Carlo with the atmospheric flux, but with the WIMP annihilation spectrum. To characterise the background we just refer to the data, as explained in the next section.

5.3 Analysis

We use an unbinned likelihood method to discriminate the signal from the background, comparing the 'background' hypothesis with the 'signal+background' hypothesis. The general scheme of our analysis, to be developed in the different subsections below, is the following. :

1. We compute the **Point Spread Function** (PSF) and the **Probability Density Function** (PDF). The PSF represents the probability for a solar event to be reconstructed with a certain angular distance to the Sun, while the PDF is the 2D map of the number of hits and the β value.
    - For the background, we use a scrambled data sample made from the real data, but randomizing the time of the events. This ensures that any possible signal event present in the sample is treated as background instead.
    - For the signal, we use the ORCA6 standard MC production software (see Sec. §4.2 for additional details) weighted by the WIMP-pair annihilation spectra.
2. **Skymaps** populated with both signal and background events are generated according to the PSF and PDF. The number of background events in each skymap corresponds to the total number of events in the sample (see Table 5.4), while the number of injected signal events is varied between 0 and 19.
3. The **likelihood function** is applied to the skymaps. The maximization of the likelihood for all the skymaps provides the **Test Statistics** (Test Statistics) distribution.
4. **Poissonian** and **Gaussian smearings** are applied over the TS distributions in order to include natural fluctuations and uncertainties associated to the detector.
5. The n_{90} is obtained as the 90% CL upper limit for a measurement equal to the median of the background TS distribution.
6. We compute the **effective area** and the **acceptance** of the detector to the signal using the WIMP-pair annihilation spectra.

7. The **sensitivity** to the flux of neutrinos from DM annihilations is obtained from the n_{90}, the livetime and the acceptance. A sensitivity on the cross section is obtained as well. At this point we chose the final set of selection cuts for each WIMP mass and annihilation channel (see Tables 5.2 and 5.3).

8. An **unblinding** is applied to the data. The likelihood function is minimised for a skymap composed by the events in the data sample, obtaining the TS of the data and the reconstructed signal in the skymap.

9. If no signal over the expected background is found, **limits on the flux of neutrinos** and on the **cross section** are computed.

10. If the TS of the data is higher than the median of the background TS distribution, the limit is calculated using the TS of the data. In the opposite case, a conservative scenario is adopted and the limit is set to the sensitivity.

The likelihood ingredients: PSF and PDF

The likelihood function used in this analysis can be written

$$\ln \mathcal{L}(n_s) = \sum_{i=1}^{N} \ln \left[n_s \mathcal{S}\left(\Psi_{\odot,i}, \beta_i, N_{hits,i}\right) + n_b \mathcal{B}\left(\Psi_{\odot,i}, \beta_i, N_{hits,i}\right) \right] - (n_s + n_b), \tag{5.2}$$

being $\mathcal{S}$ and $\mathcal{B}$ the signal and background probability density functions, n_b the number of background events, n_s the number of injected signal events and $N = n_b + n_s$ the total number of events.

The probability density functions $\mathcal{S}$ and $\mathcal{B}$ are introduced in the analysis as histograms. They are expressed as the product of the PSF distribution (*i.e.*, the probability distribution for an event to be reconstructed with a certain angular distance $\Psi_\odot$ to the Sun) and the PDF (*i.e.*, the two dimensional distribution of the energy estimator, N_{hits}, and the estimated error in the reconstruction of the track direction, β).

The PSF is then built in a different way for signal and background:

- For the signal, we use the standard ORCA6 MC neutrino production weighted by the WIMP-pair annihilation spectra. The Sun is assumed to be a point-like source and its position is assumed to be known. The angular distance from each signal event to the Sun is computed from the true direction (given by the

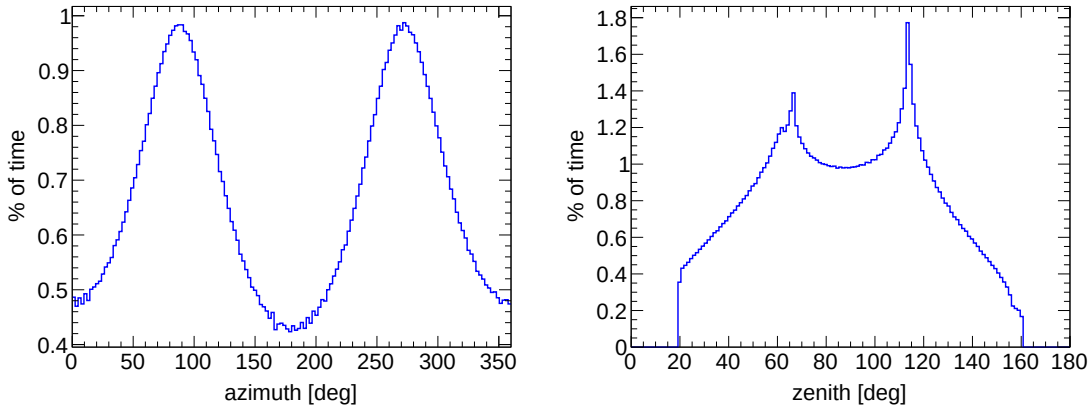

Figure 5.5: Path of the Sun during the 543 days livetime of the analysed ORCA6 data sample. Each bin represents a position on the sky, and the Y axis is the percentage of the time in which the Sun is located in that position. The zenith and the azimuth are given for the coordinates of the KM3NeT/ORCA detector, 47°48.3′N and 6°01.7′E.

MC) and the reconstructed direction,

$$\cos\left(\Psi_{\odot}\right) = \vec{u}(1, \theta_{MC}, \phi_{MC}) \cdot \vec{v}(1, \theta_{reco}, \phi_{reco}). \tag{5.3}$$

The previous assumption is supported by the fact that the angular size of the Sun, with a radius $r_{\odot} = 0.26°$, is much smaller than the angular resolution of ORCA6 – typically a few degrees.

- For the background, the direction of the events is compared to the position of the Sun. Due to the fact that scrambled data is used at this stage of the analysis, the true position of the Sun for each event is unknown. Therefore, the path of the Sun at the ORCA location during the livetime of the sample is tracked and a random position is chosen to be compared with each event. Fig. 5.5 shows the tracked path of the Sun during the livetime of the analysed data sample.

Both signal and background PSFs are normalised to 1. Fig. 5.6 shows two examples of PSF distributions for the three WIMP-pair annihilation channels explored, $\tau^+\tau^-$ (red), W^+W^- (blue) and $b\bar{b}$ (green), together with the background PSF distribution for the corresponding sets of cuts.

As already mentioned, the background PDF is built from scrambled data while the signal PDF is built from the standard ORCA MC production weighted by the

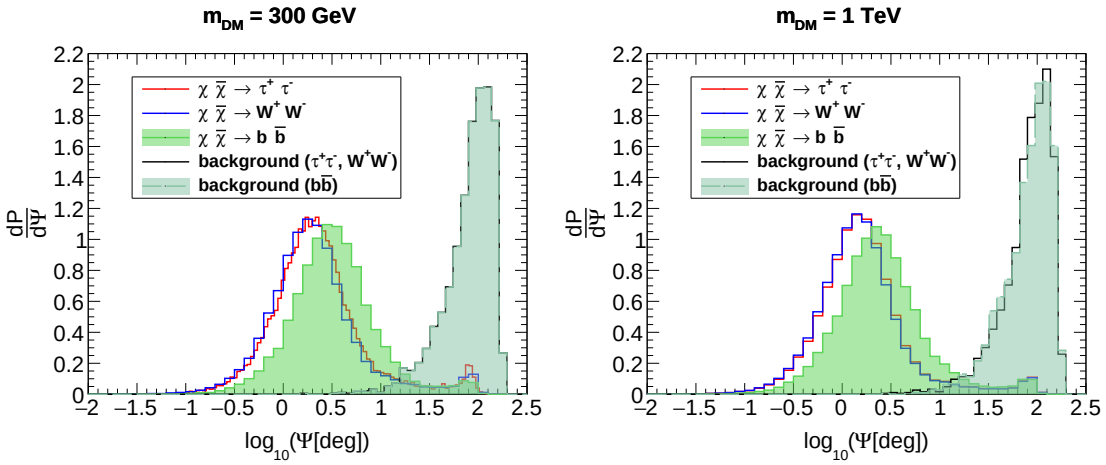

Figure 5.6: PSF distributions for a WIMP mass of 300 GeV (left) and 1 TeV (right) for the $\tau^+\tau^-$, W^+W^- and $b\bar{b}$ annihilation channels. The black line represents the background PSF that is used for the $\tau^+\tau^-$ and W^+W^- annihilation channels, and the pallid green dashed line is the background PSF used for the $b\bar{b}$ annihilation channel. Both the $b\bar{b}$ signal and background PSF lines are filled to remark that the set of cuts used for the $b\bar{b}$ channel is different than the set of cuts used for the other two channels.

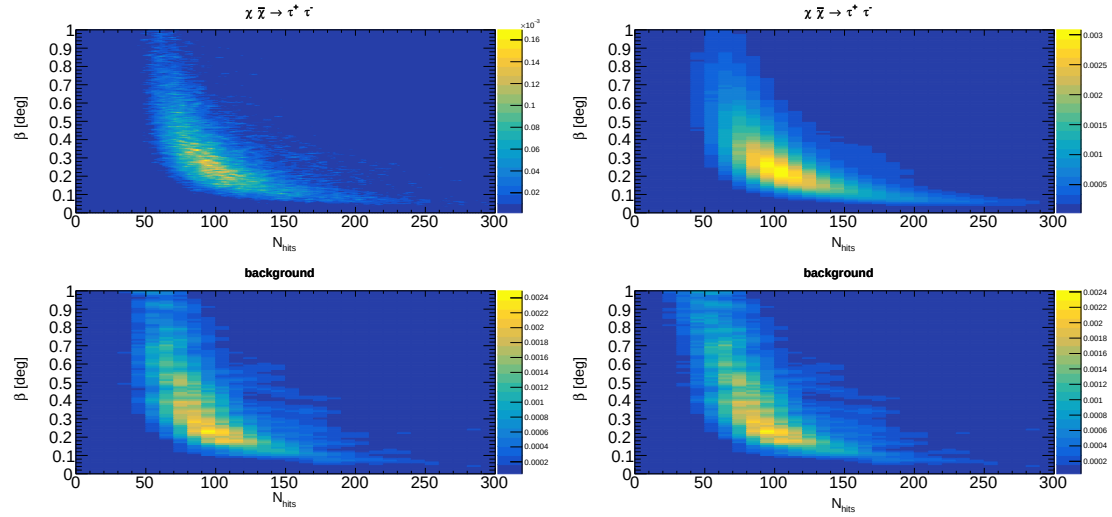

Figure 5.7: PDF distributions for the $\tau^+\tau^-$ channel and for the background for a WIMP mass of 300 GeV (left) and 1 TeV (right).

WIMP-pair annihilation spectra. They represent the probability for an event to be reconstructed with a certain value of β and N_{hits}. Fig. 5.7 shows four examples of PDF: two for the signal of the $\tau^+\tau^-$ annihilation channel and two for the corresponding backgrounds. The examples are shown for a WIMP mass of 300 GeV and 1 TeV.

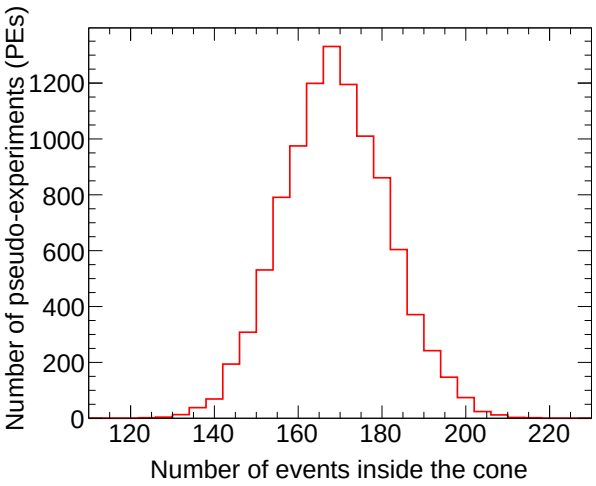

Figure 5.8: Number of events inside the 30° cone around the Sun for a total of 10^4 PEs.

Pseudo-experiments

Pseudo-experiments (PEs) are a simulations of 'fake' skymaps. Each skymap is populated with a fixed number of background events inferred from scrambled data and a variable number n_{inj} of *injected* signal events, from 0 to 29 in our case. The properties of the events within these skymaps (the distance to the Sun location, the β parameter and the number of hits) are selected based on the corresponding PSFs and PDFs.

For each annihilation channel, WIMP mass and number of injected signal events, we have generated a total of 10^4 PEs. In each skymap, the likelihood function (described in Eq. (5.2)) is maximised to determine the number of *reconstructed* signal events, n_{reco}.

In order to reduce the processing load in the Likelihood function computation, only events inside a cone with a 30° radius around the Sun are processed. Events outside this cone are treated as background for computational purposes. Fig. 5.8 shows the total number of events inside the cone for the background-only hypothesis ($n_{\text{inj}} = 0$) for the 10^4 PEs. An average of 168 events lie inside the cone.

Fig. 5.9 shows the average number of reconstructed signal events for the $\tau^+\tau^-$ channel as a function of the number of injected signal events for WIMP masses of 100 GeV, 300 GeV, 500 GeV and 1 TeV. The black line represents the scenario in which the reconstructed number of signal events matches the number of injected signal events,

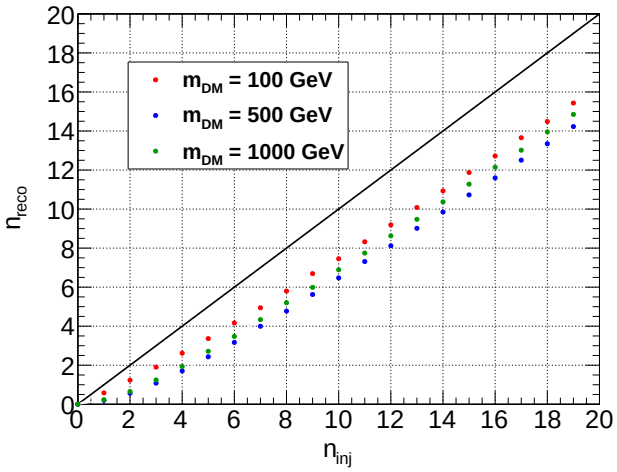

Figure 5.9: Mean number of reconstructed signal events as a function of the total number of injected signal events in the Likelihood for the $\tau^+\tau^-$ channel for several WIMP masses.

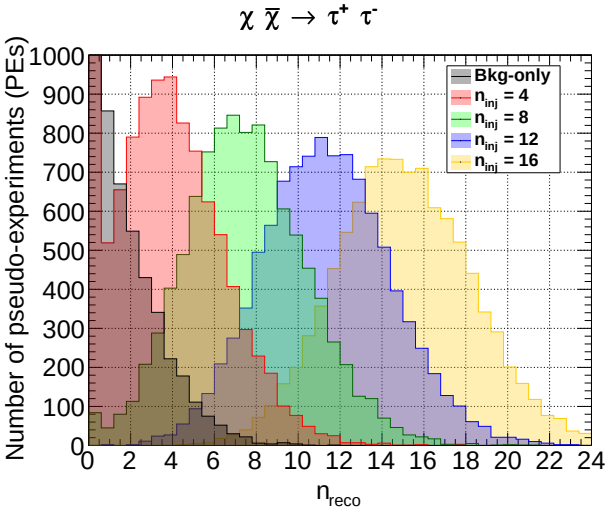

Figure 5.10: Distribution of reconstructed signal events in a total of 10^4 PEs for the background-only case and several values of n_{inj}. The plot corresponds to the $\tau^+\tau^-$ annihilation channel and a WIMP mass of 300 GeV.

$n_{\text{reco}} = n_{\text{inj}}$. A tendency to underestimation is observed in the number of reconstructed signal events. This underestimation becomes more pronounced with increasing WIMP mass, and it can be attributed to the similarities between the signal and background PDFs and PSFs, which can hinder the optimization process of the likelihood.

Fig. 5.10 shows the distribution of n_{reco} values obtained through the likelihood function for the 10^4 PEs for several values of n_{inj} and a WIMP of 300 GeV that annihilates to $\tau^+\tau^-$. The black-grey distribution represents the background-only case ($n_{\text{inj}} = 0$), whereas the red, green, blue and yellow lines correspond to 4, 8, 12 and 16) injected signal events, respectively.

Test statistic distributions

To address the statistical significance of a signal we need to compare the hypothesis of the existence of a signal within the dataset (H1) to the null hypothesis (H0), in which no signal is found among the background. This comparison is performed using the likelihood ratio principle [166, 167]. The likelihoods associated to each hypothesis are built using pseudo-experiments, and a test statistic (TS) is calculated from the ratio of the likelihoods:

$$TS = \log_{10}\left(\frac{\mathcal{L}_{H1}(n_{inj})}{\mathcal{L}_{H0}(n_{inj} = 0)}\right). \tag{5.4}$$

For each combination of WIMP mass, annihilation channel and number of injected signal events, applying the expression above to the 10^4 PEs results in a TS distribution.

To obtain continuous values representing the count of signal events and to take into account statistical fluctuations, a Poissonian smearing is applied to the TS distributions. The resulting TS distributions become then dependent on the Poissonian mean parameter, denoted as μ. We generate 20 Poissonian distributions for each value of n_{inj}, implying that the Poissonian mean (μ) varies in steps of 0.05. Together with this Poissonian smearing, we apply a Gaussian smearing to characterise the natural fluctuations. Among others, this also includes a 10% systematic uncertainty [168] that is introduced from the reconstruction of the neutrino track direction.

The smearing changes the distribution $P(TS|i)$ into a continuous and smooth distribution $P(TS|\mu)$ defined as

$$P(TS|\mu) = \sum_{i=0}^{n_{inj}^{max}} P(TS|i)P(i|\mu), \tag{5.5}$$

where

$$P(i|\mu) = \int_{\mu-4\sigma_\mu}^{\mu+4\sigma_\mu} P(i|\bar{\mu})G(\bar{\mu}|\mu,\sigma_\mu)d\bar{\mu}, \tag{5.6}$$

and

- $P(TS|\mu)$ is the TS distribution for a Poissonian mean μ of detected events.
- $P(TS|i)$ is the TS distribution for a number of i injected events (results from the PE).
- $P(i|\mu)$ is the Poissonian probability to detect i events given a mean μ of detected events.
- $P(i|\bar{\mu})$ is the Poissonian probability to detect i events given a mean $\bar{\mu}$ of detected events.
- $G(\bar{\mu}|\mu,\sigma_\mu)$ is the Gaussian smearing: the probability to detect $\bar{\mu}$ events given a mean μ of detected events with a standard deviation σ_μ.
- n_{inj}^{max} is the total number of injected events in the PE.

We assume a value $\sigma_\mu = 0.15$ to take into account the different sources of natural fluctuations in the data taking (*e.g.*, the orientation of the detector).

As an example, Fig. 5.11 shows the TS distributions for the background-only case (black line) and several values of n_{inj}: 3 (red), 4 (green), 5 (pink) and 6 (blue). The dashed line corresponds to the median of the background-only case. The first peak of the TS distributions corresponds to the cases when the likelihood function returns its minimum allowed value, which is $n_{\text{reco}} = 0.001$.

To improve the visualization and avoid zeros in the argument of the logarithm function, we shift the TS distributions to

$$Q = \log_{10}(TS + C), \tag{5.7}$$

where C is a constant factor that will be applied to each TS distribution for a given combination of WIMP mass and annihilation channel.

Effective Area and Acceptance

The effective area $A^(E)$ is defined as the geometric projection of a detector's surface to a certain energy flux, assuming a 100% efficiency. If a certain flux of neutrinos of

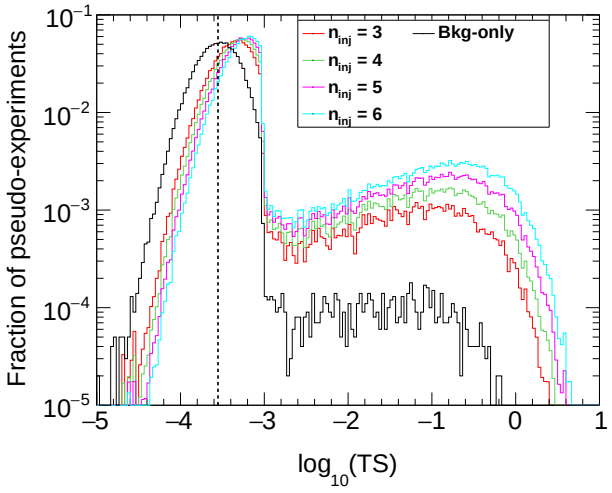

Figure 5.11: TS distributions for the $\tau^+\tau^-$ annihilation channel and a WIMP mass of 300 GeV, normalised to 1. The dashed line indicates the median of the background-only distribution ($n_{\text{inj}} = 0$).

energy E crosses the detector, the product of this flux and the effective area at that energy gives the number of expected events at the detector. This parameter can only be calculated through Monte Carlo simulations. The effective area (usually expressed in units of m^2) depends on several key variables, namely, the energy of the neutrino flux, the solid angle and the fraction of detected events. The latter implies that the effective area also depends implicitly on the set of cuts applied to the sample.

We can consider the effective area for NC and CC events,

$$A^{\text{eff}}_{\text{NC (CC)}} = \frac{1}{m\ N^{\text{gen}}_{\text{NC (CC)}}\ \ln 10 \cdot W_{\text{bin}}\,\Omega} \sum_{\substack{i\in\text{bin}\\ i\in\text{NC (CC)}}} w_i^2\, E_i^{-1}, \tag{5.8}$$

being W_{bin} the width of the considered energy bin, w_i^2 the generation weight of the event, Ω the solid angle and $N^{\text{gen}}_{\text{NC (CC)}}$ the number of Monte Carlo events generated in the neutral current (charged current) Monte Carlo interaction. The total effective area is then

$$A^{\text{eff}} = A^{\text{eff}}_{\text{CC}} + A^{\text{eff}}_{\text{NC}}. \tag{5.9}$$

We have used the Monte Carlo available to the ORCA collaboration and have applied the cuts described before to obtain the effective area of the detector in its 6 lines configuration. Fig. 5.12 shows A^{eff} of ORCA6 for an upgoing ν_μ and $\bar{\nu}_\mu$, whereas in Fig. 5.13 we plot the CC, NC and total (NC+CC) effective area for a ν_μ. We see

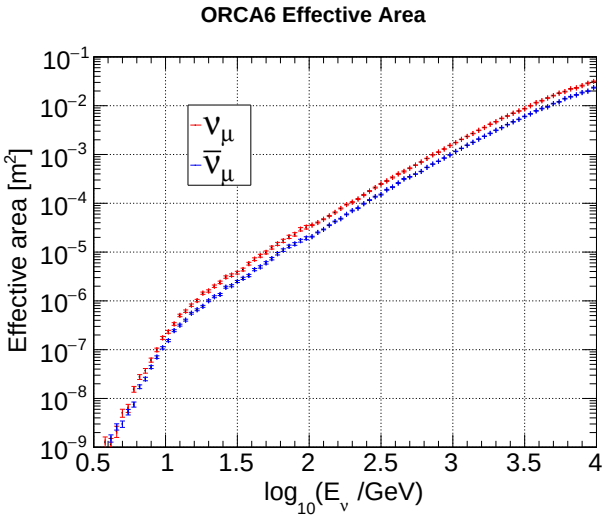

Figure 5.12: Total effective area of ORCA6. The cuts corresponding to the *low mass* range for the $\tau^+\tau^-$ WIMP-pair annihilation channel are applied (see Tables 5.2).

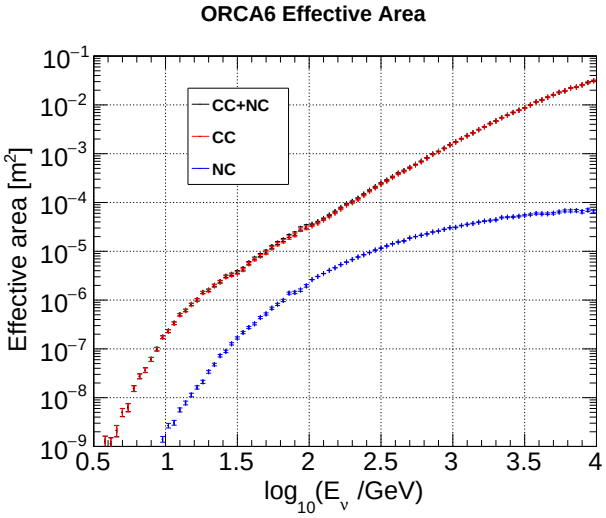

Figure 5.13: ORCA6 effective area for neutrinos for the CC, NC and CC+NC. The cuts corresponding to the *low mass* range for the $\tau^+\tau^-$ WIMP-pair annihilation channel are applied (see Table 5.2).

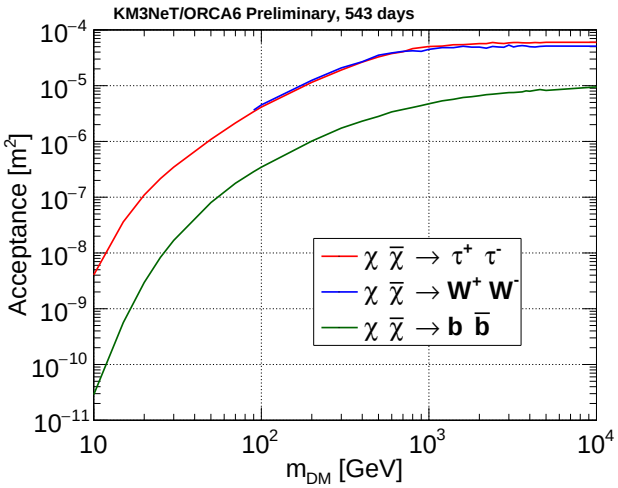

Figure 5.14: ORCA6 acceptance to the WIMP signal coming from the Sun, as a function of the WIMP mass, after applying the final selection cuts (Tables 5.2 and 5.2) and for the three studied channels. Total livetime 543 days.

that the cuts assumed make much more efficient the detection of track-like events than the point-like events associated to NC interactions: the total effective area is dominated by the contribution from neutrino CC events. Both plots correspond to the cuts for low mass DM with $\tau^+\tau^-$ or W^+W^- annihilation channel (see Table 5.2).

A new variable can be defined not for neutrinos of a given energy but to a flux that extends in an energy interval. The *Acceptance* is the weighted mean of the detector's effective area convoluted with that neutrino spectra $\mathrm{d}N_{\nu_\mu(\bar{\nu}_\mu)}/\mathrm{d}E_{\nu_\mu(\bar{\nu}_\mu)}$. This variable is be a function of the WIMP mass and is usually expressed in units of m^2:

$$Acc(m_{DM}) = \frac{\int_0^{m_{DM}} A_\nu^{\mathrm{eff}}(E)\cdot\frac{\mathrm{d}N_\nu}{\mathrm{d}E}\cdot\mathrm{d}E + \int_0^{m_{DM}} A_{\bar{\nu}}^{\mathrm{eff}}(E)\cdot\frac{\mathrm{d}N_{\bar{\nu}}}{\mathrm{d}E}\cdot\mathrm{d}E}{\int_0^{m_{DM}}\left(\frac{\mathrm{d}N_\nu}{\mathrm{d}E}\cdot\mathrm{d}E + \frac{\mathrm{d}N_{\bar{\nu}}}{\mathrm{d}E}\cdot\mathrm{d}E\right)}. \tag{5.10}$$

As shown in Eq. (5.10), the Acceptance is averaged over the number of neutrinos and anti-neutrinos predicted by the model, and it is also determined (see Fig. 5.14) by the upper limit of the WIMP mass m_{DM}, and the annihilation channel under consideration ($\tau^+\tau^-$, W^+W^- and $b\bar{b}$). Notice that different annihilation channels and WIMP mass values lead to different neutrino spectra that find different effective area when reaching the detector.

The expected number of events (N_{evt}) for a given neutrino flux Φ_ν (neutrinos per m^2 and second) crossing the detector during a data taking lifetime T (in units of

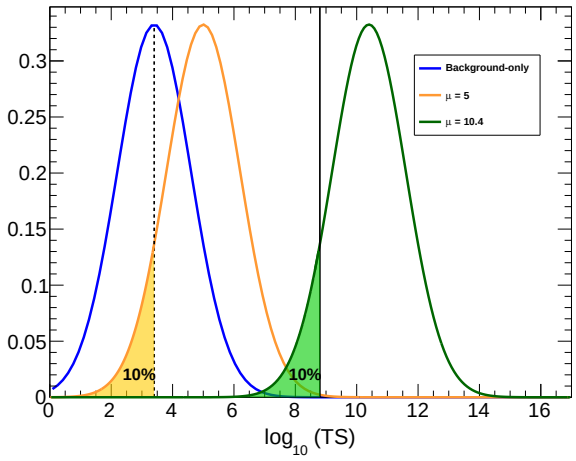

Figure 5.15: General scheme for the calculation of n_{90}. The blue histogram on the left represents the background-only distribution, with a median value corresponding to the dashed line. The orange distribution corresponds to an alternate hypothesis with median $\mu = 5$ events in the data sample. The green line corresponds to an alternative hypothesis with median $\mu = 10.4$ events. The black, solid line indicates the TS of the data after unblinding, also called TS_{obs} (see Sec. §5.3 for additional details). The shaded areas indicate the 10th percentile of the distribution. In this example, the 10% tail of the orange histogram is below the median of the background-only distribution, meaning that the n_{90} value for the sensitivity is the median of the orange distribution ($n_{90} = 5$ in this example). On the other hand, the 10% tail of the green distribution is below n_{obs}, implying that the n_{90} value for the limits in this example is the median of the green distribution, ($n_{90} = 10.4$ in this example).

seconds) [169, 170, 171, 172] is given by

$$N_{\text{evt}} = Acc(m_{DM})\,\Phi_{\nu}\,T. \tag{5.11}$$

n_{90} and sensitivity

The n_{90} is defined as the minimum number of signal events within a given dataset required to claim a discovery with a 90% CL. Statistically [173], the n_{90} corresponds to the minimal number of events needed to reject the 'null hypothesis' H0 – *i.e.*, a scenario where only background processes are at play – ensuring a 90% confidence level. Furthermore, this criterion mandates a 50% probability of accepting the alternative hypothesis H1, claiming the presence of a signal in the dataset. Fig. 5.15 shows an illustrative representation of the hypotheses testing.

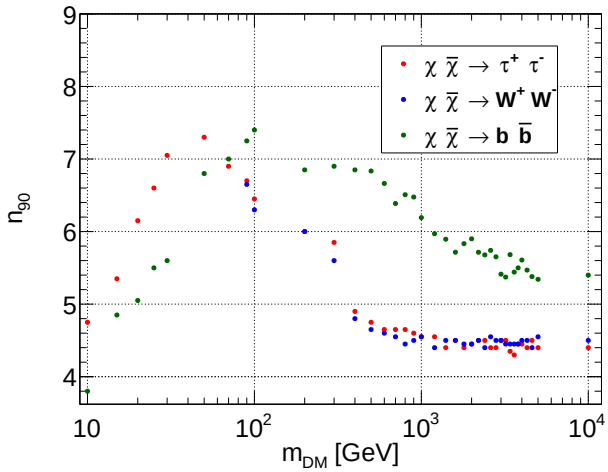

Figure 5.16: n_{90} as a function of the WIMP mass after applying the final selection cuts (Tables 5.2 and 5.3) for the three WIMP-pair annihilation channels.

For a given combination of WIMP mass and annihilation channel, the calculation of the n_{90} requires the following steps.

i. Compute the TS distribution for the set of hypotheses assumed in the PE. Each hypothesis corresponds to a different number of injected signal events, being $n_{\text{inj}} = 0$ the background-only scenario.

ii. Compute the median of the background-only TS distribution.

iii. Find the TS distribution whose 10th percentile is equal to the median of the background-only distribution.

iv. The mean of such TS distribution is n_{90}, *i.e.*, the minimum number of events needed to claim that the signal has been observed at 90% CL. Fig. 5.16 shows the n_{90} value for all the combinations of WIMP masses and annihilation channels.

The minimum number of signal events needed to claim that the sample contains a signal can be translated into *sensisitivity* or minimum total flux of neutrinos coming from the Sun from WIMP-pair annihilations required to make the claim,

$$\Phi_{\nu_\mu+\bar{\nu}_\mu}(m_{DM}) = \frac{n_{90}}{T \cdot Acc(m_{DM})}. \tag{5.12}$$

Fig. 5.17 shows the sensitivity to the $\nu_\mu + \bar{\nu}_\mu$ flux. The sensitivity is higher at low masses because most of the neutrinos produced by low mass WIMPs have energy

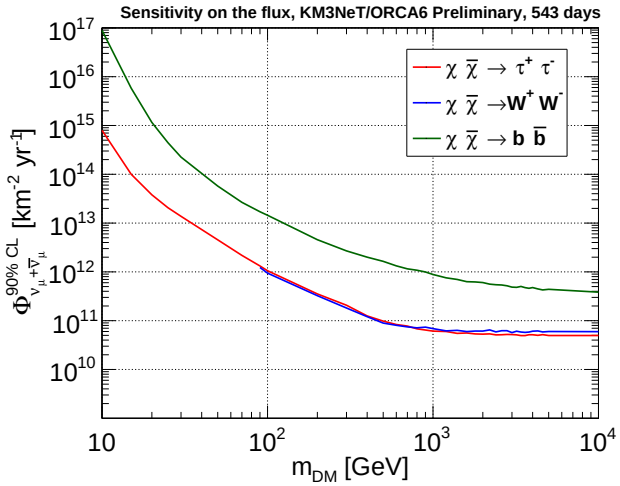

Figure 5.17: ORCA6 sensitivity to the WIMP signal coming from the Sun, as a function of the WIMP mass, after applying the final selection cuts (Tables 5.2 and 5.3) and for the three studied channels. Total livetime 543 days.

lower than the ORCA6 threshold, 1 GeV, and, consequently, most of the signal lies outside the energy range of the detector. On the other side, at higher masses most of the signal lies in the ORCA energy range of detection. Therefore, the sensitivity is lower. Starting on the TeV range, the curve tends to flatten due to the fact that neutrinos with energies in the TeV range and above are produced. These neutrinos are not likely to escape from the Sun, and the sensitivity saturates.

Unblinding results

Following the policies of the KM3NeT collaboration, once we established the selection cuts and computed the sensitivity we entered a period when our analysis was documented, presented and discussed in several Working Group and Collaboration meetings. Once it passed the reviews by the internal referees, the green light for the unblinding of the data was granted. The so-called unblinding process involves the following steps:

i. The unaltered data sample is used to build the PSF and PDF of the data.

ii. The likelihood method is applied over the skymap defined by the unblinded data sample. If the reconstructed – observed – signal events is higher than the n_{90}, $n_{\text{obs}} > n_{90}$, a discovery could be claimed.

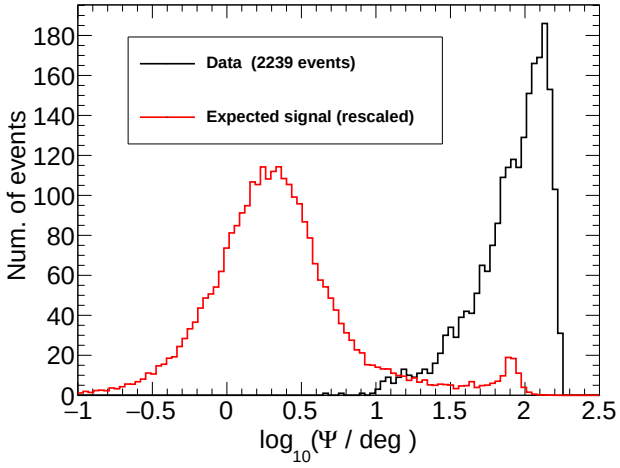

Figure 5.18: Distribution of the angular distance of the unblinded data events (543 days livetime) to the Sun (black). The red histograms correspond to the (rescaled) distribution of the Monte Carlo $\chi\bar{\chi} \to \tau^+\tau^-$ signal events (PSF) for a $m_{DM} = 300\,\text{GeV}$.

iii. If $n_{\text{obs}} < n_{90}$, a limit on the neutrino flux is computed in the following way:

   a) The TS value of the skymap defined by the real data sample, TS_{obs}, is calculated.

   b) If TS_{obs} is greater than the median of the background-only TS distribution (calculated previously from the PE), a new n_{90} upper limit value is obtained from this TS value (see Fig. 5.15) and the limit to the flux of neutrinos is calculated using Eq. (5.12).

   c) If TS_{obs} is smaller than the median of the background-only TS distribution, a conservative scenario is adopted and the limit is set equal to the sensitivity.

Fig. 5.18 shows the distribution of the reconstructed angular distance from the events to the Sun, for the unblinded data sample and for the expected signal for the $\tau^+\tau^-$ annihilation channel and a WIMP mass of 300 GeV.

The unblinding revealed no evidence of WIMP-pair annihilation signal in the data above the expected background. The observed signal upper limit, n_{obs}, resulted smaller than all n_{90} values quoted for all combinations of WIMP mass in the three annihilation channels. Therefore, the limits on the neutrino flux are set equal to the sensitivities. Fig. 5.19 shows the TS distribution calculated from the PEs compared

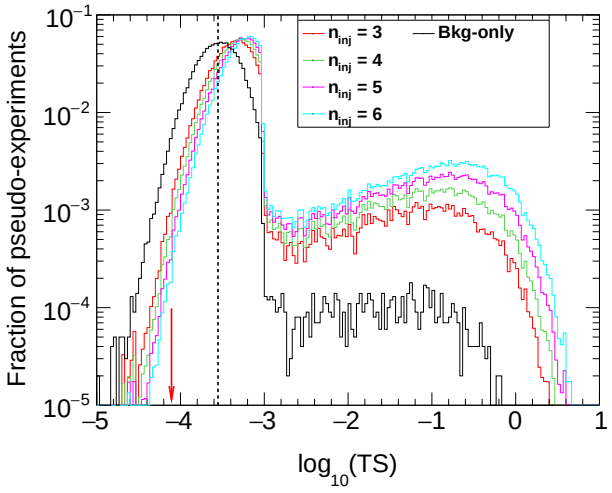

Figure 5.19: TS distributions for the $\tau^+\tau^-$ annihilation channel and a WIMP mass of 300 GeV, normalised to 1. The dashed line indicates the median of the background-only distribution ($n_{\text{inj}} = 0$). The red arrow indicates the TS of the data, $TS_{\text{obs}} = -4.1$.

with the value of the TS obtained with the unblinded data (TS_{obs}) for a WIMP mass of 300 GeV and the $\tau^+\tau^-$ annihilation channel. Fig. 5.20 shows the limits on the neutrino+antineutrino flux obtained using Eq. (5.12).

We can finally translate this limit on the neutrino flux into a limit in the WIMP-nucleon interaction cross section. For simplicity, we assume a stationary regime with the capture rate of DM in the Sun (C_r) twice the annihilation rate (Γ_r):

$$C_r = 2\Gamma_r. \tag{5.13}$$

On the other hand, the annihilation rate is related to the limit on the neutrino flux at ORCA6,

$$\Gamma_r = \frac{R_E^2}{2D_{SE}} \Phi_{\nu_\mu + \bar{\nu}_\mu}, \tag{5.14}$$

being R_E the radius of the Earth and D_{SE} the distance between the Sun and the Earth.

The capture rate through spin dependent interactions can be expressed

$$C_r = \Lambda^{SD} \sigma^{SD}, \tag{5.15}$$

where Λ^{SD} is a factor that depends on the WIMP mass, the annihilation channel, among other factors. An analogous expression would describe the capture rate through spin independent interactions.

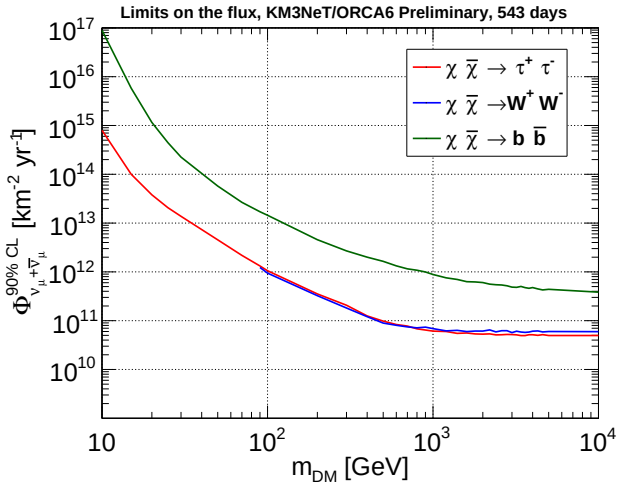

Figure 5.20: ORCA6 90% CL limit to the neutrino flux coming from WIMP-pair annihilation in the Sun (this work), as a function of the WIMP mass, after applying the final selection cuts (Tables 5.2 and 5.3) and for the three studied channels. Total livetime 543 days.

From the equations above we obtain

$$\sigma^{SD(SI)} = K^{SD(SI)} \cdot \Phi_{\nu_\mu+\bar{\nu}_\mu}, \tag{5.16}$$

with

$$K^{SD(SI)} = R_E^2/(D_{SE} \cdot \Lambda^{SD(SI)}) \tag{5.17}$$

being the so-called conversion factor (in units of $\mathrm{pb\,km^2\,yr}$). The conversion factors are obtained with the DarkSUSY package [159] under the following assuptions:

- The DM density in the proximity of the Sun is set to $\rho = 0.3\,\mathrm{GeV/cm^3}$ and its velocity is assumed to follow a Maxwellian distribution with a mean of 270 m/s.
- For the spin-dependent interactions, the DM particles couple only to protons (not to neutrons, $c_n = 0$).
- For the spin-independent interactions, it is assumed an equal coupling to protons and neutrons ($c_p = c_n$).

In Fig. 5.21 we show the conversion factor between WIMPs and baryonic matter [159] for spin-dependent and spin-independent interactions .

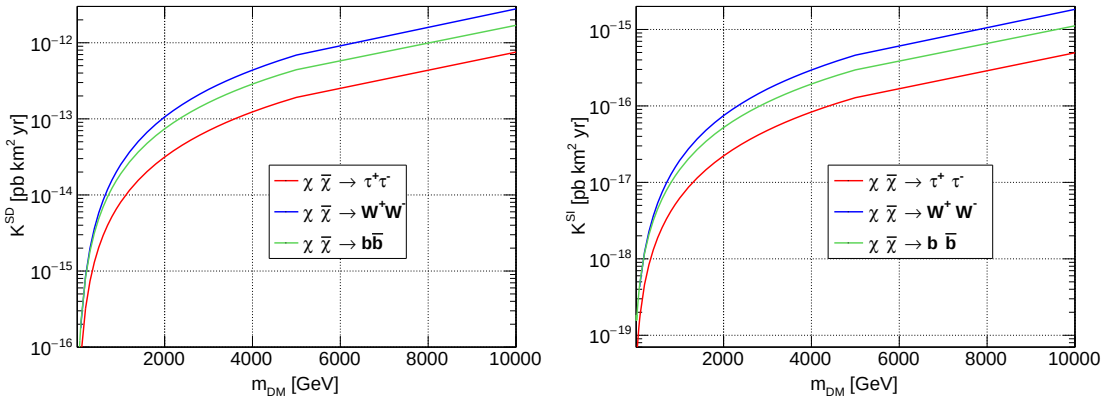

Figure 5.21: Conversion factors as a function of the WIMP mass, computed with DarkSUSY [159] for the spin-dependent (left) and spin-independent (right) interaction cross sections, and for the three WIMP-pair annihilation channels.

Figs. 5.22 and 5.23 summarise the final results obtained in this second part of the thesis. We show the limits from our analysis on the spin-dependent and spin-independent cross sections. We include for comparison the current bounds from ANTARES, IceCube, IceCore, Super-Kamiokande and PICO-60 for the first one and from ANTARES, IceCube, IceCore, Super-Kamiokande and XENON-1T for the spin-independent cross section.

The limits obtained in this work with the ORCA6 detector are still above the ones obtained by other experiments. However, the 6 DUs currently operative will be multiplied by 20 once the full ORCA configuration with 115 DUs is achieved. Therefore, our analysis reveals the potential of the ORCA detector in the search for DM. In particular, with a livetime of only 543 days, it has already outperformed its predecessor, ANTARES, at some DM masses. The search for 1–100 GeV neutrinos from point-like sources with ORCA will indeed explore new grounds during the next decade.

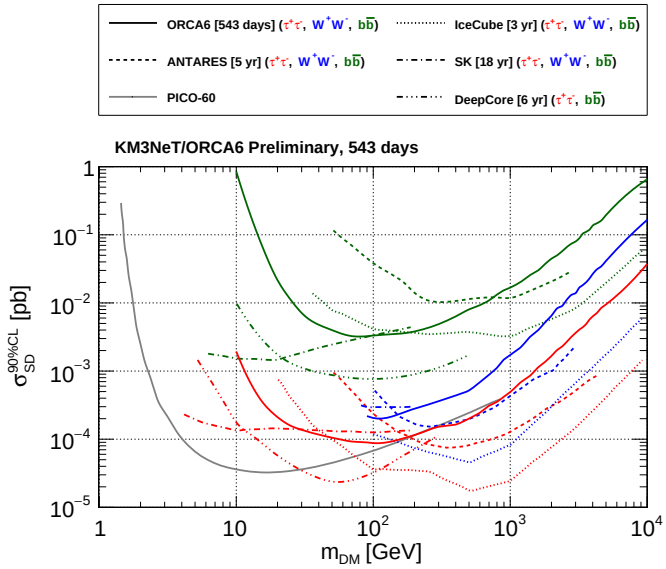

Figure 5.22: ORCA6 90% CL upper limit to the WIMP-nucleon spin-dependent cross section (this work), as a function of the WIMP mass, and for the three studied channels. Total livetime 543 days. The other lines represent the results from IceCube [174], ANTARES [175], Super-Kamiokande [176], DeepCore [177] and PICO-60 [99].

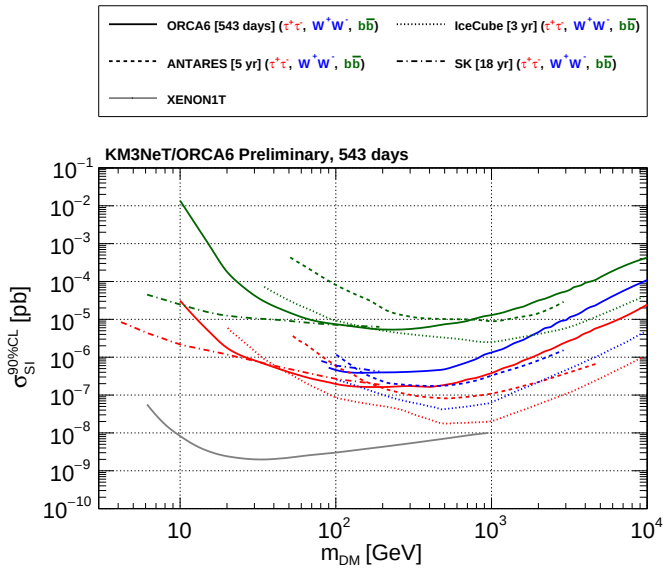

Figure 5.23: ORCA6 90% CL upper limit to the WIMP-nucleon spin-independent cross section (this work), as a function of the WIMP mass, and for the three studied channels. Total livetime 543 days. The other lines represent the results from IceCube [174], ANTARES [175], Super-Kamiokande [176] and XENON-1T [94].

Summary and discussion

A billion neutrinos go swimming in heavy water: one gets wet.

Michael Kamakana.

Dark matter has been a subject of study during the past 50 years. A large variety of candidates has been proposed, with a spectrum of masses that goes from the axion at 10^{-12} eV to primordial black holes at 10^{58} eV. Among them, the most popular has been the WIMP. On one hand, the WIMP has usually been proposed within a framework that *solves* some other issues of the SM, like the stability of the electroweak scale (*e.g.*, the lightest supersymmetric particle). On the other hand, it has been attractive because the WIMP has phenomenological implications in direct, indirect and collider searches.

A WIMP could accumulate in astrophysical objects like the Sun or the galactic center. As the local DM density increases, the possibility of annihilations increases as well. If detected, the high energy secondaries from these annihilations would be an indirect sign of DM. Notice that the hottest objects of the universe (proto-neutron stars) have a temperature below 50 MeV, so the detection of any emission at higher energies would be very interesting.

The indirect detection of DM has been the main topic of this thesis. In particular, neutrinos offer the possibility to *see* the interior of the Sun or distant astrophysical objects. Of course, being weakly interacting also adds difficulty in the detection: we need to monitor very large volumes to register just a few events. We have focused on the production and the detection of a DM WIMP trapped in the Sun. After decades of intense direct searches with negative results, our generic objective has been to calibrate how *natural* the WIMP still is. More precisely, whether the bounds from direct searches are consistent with the observed relic abundance and if they leave any

room to expect a signal in neutrino telescopes. Notice that the same elastic processes probed at XENON1T are producing the DM capture by the Sun.

Our work in this thesis includes two parts: a phenomenological and an experimental one. The phenomenology, in turn, is further divided into two chapters. In Chapter 2, we study and charaterise the neutrino fluxes that would be a background in the search for DM from the Sun: the atmospheric neutrino flux and the ones produced by CRs showering in the solar surface. The latter are interesting by themselves, but they are also an irreducible background in these searches. We have developed an scheme that avoids the uncertainties introduced by the solar magnetism by correlating observations in different astroparticle channels at TeV energies, namely, the CR shadow of the Sun at HAWC and the gamma flux from the solar disk at Fermi-LAT and HAWC. The scenario also implies a high energy neutron flux (non observable with current detectors) and a muon shadow of the Sun that has just been detected by IceCube. Most important for the work presented here, it implies a well defined neutrino background from the solar disk. At low energies ($E \leq 1$ TeV) CRs do not reach the solar surface and the background is the atmospheric one plus the neutrinos produced by neutrons entering the atmosphere. At 2–20 TeV CRs reach the Sun and the emission of secondaries is mostly isotropic, inducing an albedo flux that adds to the neutrinos produced in the side of the Sun not facing the Earth. At CR energies above 50 TeV magnetic effects can be neglected and neutrinos reaching the Earth must cross the Sun before. To calculate these fluxes, we have written and solved cascade equations in the Sun. Our results for the fluxes of neutrinos, neutrons, and gamma rays emitted by the Sun can be seen in Fig. 2.15. We find remarkable that our model fits very well the gamma-ray flux from the Sun compared to the gamma flux measured by Fermi-LAT [78] and *predicted* correctly a very recent observation at 1 TeV by HAWC [74]. It is also important to notice that current bounds imply that most DM models connected to the visible matter through a spin independent interaction will give a signal well below this background at neutrino telescopes [61].

In Chapter 3 we define a DM model that provides an optimal signal at telescopes. Our candidate is a Majorana fermion χ connected to a heavy neutrino N that completes the neutrino sector through an inverse see-saw mechanism at the TeV scale. χ can annihilate into a monochromatic neutrino through the Higgs portal. The model has three independent couplings (c_s, c_a, and c_N), two masses (m_χ and m_N) and one heavy-light mixing (s_α). In direct detection experiments the contribution of c_a and c_N is irrelevant, so we can use them to reproduce the relic abundance necessary to explain the DM, $\Omega_{\rm DM}h^2 = 0.12$. c_s, in turn, fixes the signal in direct searches and

the capture rate by the Sun, that we calculate. Figs. 3.11 and 3.12 show the signal, well above the background, that could be expected for WIMP masses of 300 GeV and 1 TeV.

The experimental part of this thesis has also two chapters. In Chapter 4 we describe KM3NeT, a neutrino telescope currently being built in the Mediterranean Sea. The experiment includes two detectors, ARCA and ORCA, located in Italy and France, respectively. Among the many analyses being carried out by the KM3NeT collaboration there is also the search for DM in different astrophysical bodies. In particular, the Sun is one of the most promising ones because of its proximity and size.

Then in Chapter 5 we analysed a dataset from the ORCA neutrino telescope in its configuration with 6 Detection Units, including 553 days of data. We consider WIMP-like particles that annihilate into $\tau^+\tau^-$, W^+W^-, or $b\bar{b}$, assuming in each case a 100% branching ratio. For each channel and WIMP mass we characterise the signal and background using the WimpSim package [165] together with PSFs and PDFs deduced from the Monte Carlo of the collaboration and the srambled data. Then we built 10^4 Pseudo-experiments and evaluated each skymap with a Likelihood function. The minimization of this function gave us the number of reconstructed signal events for that skymap, n_{reco}. Then we obtained the Test Statistic distribution, applying a Poissonian smearing. With this we deduced the n_{90} and calculated the sensitivity to the neutrino flux produced in WIMP annihilations. Finally we performed a data unblinding – *i.e.*, repeated the process but this time using the real dataset instead of the scrambled data – and found no signal excess over the expected background. Based on this null search result, we set limits on the sensitivity, that are subsequently converted into limits on the cross section for DM-nucleon collisions. Our analysis does not find a signal but puts competitive limits (see Figs. 5.22 and 5.23), which demonstrates the potential of the KM3NeT/ORCA detector and the KM3NeT infrastructure to make discoveries in the future, once completed on its final configuration.

We conclude that, despite decades of searches that constrain its parameter space, the WIMP paradigm is still viable. Moreover, the possibility to probe it in a variety of different experiments, which is basically what makes it specially interesting, still remains.

Resumen y discusión

> Mil millones de neutrinos se van a nadar en agua pesada; uno de ellos se moja.
>
> Michael Kamakana.

La materia oscura ha sido objeto de estudio durante los últimos 50 años. Aunque su naturaleza aún es desconocida, se han propuesto una gran variedad de candidatos, con un espectro de masas que va desde el axión a 10^{-12} eV hasta los agujeros negros primordiales a 10^{58} eV. Entre ellos, el modelo más popular ha sido el WIMP. Entre los motivos de su popularidad se encuentran, por un lado, el hecho de que el WIMP generalmente se ha propuesto dentro de un marco que "resuelve" otros problemas del Modelo Estándar, como la estabilidad de la escala electrodébil (por ejemplo, la partícula supersimétrica más ligera podría ser un WIMP). Por otro lado, es un modelo atractivo porque tiene implicaciones fenomenológicas en búsquedas directas, indirectas y de colisionadores.

Los WIMPs podrían acumularse en objetos astrofísicos como el Sol o el centro galáctico. A medida que éstos quedasen atrapados en dichos objetos y aumentase la densidad local de materia oscura en los mismos, también aumentaría la posibilidad de éstos se aniquilen. Si se detectasen, las partículas secundarias de alta energía provenientes de estas aniquilaciones serían una señal indirecta de la existencia de materia oscura. Cabe destacar que los objetos más calientes del universo (protoestrellas de neutrones) tienen una temperatura inferior a 50 MeV, por lo que la detección de cualquier emisión a energías más altas sería muy interesante y podría arrojar luz sobre el misterio que rodea a la materia oscura.

La detección indirecta de materia oscura ha sido el tema principal de esta tesis. Dado que los neutrinos interactúan débilmente, pueden atravesar grandes longitudes sin interactuar, y, por lo tanto, permiten "ver" el interior de las fuentes en las que se

producen. Sin embargo, el hecho de que interactúen con muy poca frecuencia también complica su detección: necesitamos detectores con volúmenes muy grandes para poder registrar unos pocos eventos de interacciones de neutrinos. En esta tesis nos hemos centrado en la caraterización y detección de WIMPs atrapados en el Sol. Después de décadas de intensas búsquedas directas con resultados negativos, el objetivo de esta tesis ha sido calibrar cómo de "natural" sigue siendo el modelo de materia oscura de WIMPs. Más concretamente, queremos comprobar si las restricciones de las búsquedas directas son consistentes con la abundancia reliquia necesaria para la materia oscura y si dejan algún margen para poder observar una señal de aniquilación de pares de WIMP en los telescopios de neutrinos. Cabe destacar que las mismas colisiones elásticas que se buscan en experimentos de detección directa como XENON1T son también los que se producirían en el Sol cuando la materia oscura queda atrapada en el mismo.

Nuestro trabajo en esta tesis se divide en dos partes: una fenomenológica y otra experimental. La fenomenología, a su vez, está formada por dos capítulos. En el Capítulo 2, estudiamos y caracterizamos los flujos de neutrinos que podrían ser un fondo en la búsqueda de materia oscura proveniente del Sol: el flujo de neutrinos atmosféricos y los producidos por lluvias de rayos cósmicos en la superficie solar. Si bien éstos son interesantes por sí mismos, también constituyen un fondo inevitable en estas búsquedas. Hemos desarrollado un esquema que evita las incertidumbres introducidas por el magnetismo solar al correlacionar observaciones en diferentes canales de astropartículas a energías del orden del TeV. Estos canales son la sombra de rayos cósmicos del Sol en HAWC y el flujo de rayos gamma provenientes del disco solar en Fermi-LAT y HAWC. Nuestro modelo también predice un flujo de neutrones de alta energía (no observable con detectores actuales) y una sombra de muones del Sol que acaba de ser detectada por IceCube. Además, la existencia de estos flujos implica un fondo de neutrinos bien definido proveniente del disco solar. A bajas energías ($E \leq 1$ TeV), los rayos cósmicos no alcanzan la superficie solar y el fondo está compuesto por el atmosférico, más los neutrinos producidos por los neutrones que llegan a la atmósfera. En el rango de 2 a 20 TeV, los rayos cósmicos llegan al Sol y la emisión de partículas secundarias es mayormente isotrópica, lo que induce un flujo de albedo que se suma a los neutrinos producidos en el lado del Sol que no está apuntando a la Tierra. A energías de rayos cósmicos superiores a 50 TeV, los efectos magnéticos pueden ser despreciados y todos los neutrinos que llegan a la Tierra deben atravesar el Sol antes. Para calcular estos flujos, hemos escrito y resuelto ecuaciones de cascada en el Sol. Nuestros resultados para los flujos de neutrinos, neutrones

y rayos gamma emitidos por el Sol se muestran en la Figura 2.15. Cabe destacar que nuestro modelo se ajusta muy bien al flujo de rayos gamma proveniente del Sol medido por Fermi-LAT [78] y *predijo* correctamente una observación muy reciente a 1 TeV por HAWC [74]. Por último, es importante señalar que las cotas actuales implican que la mayoría de los modelos de materia oscura conectados a la materia visible a través de una interacción independiente del espín darán una señal muy por debajo de este fondo en telescopios de neutrinos [61].

En el Capítulo 3 definimos un modelo de materia oscura que proporciona una señal óptima en telescopios de neutrinos. Nuestro candidato a materia oscura es un fermión de Majorana χ conectado a un neutrino pesado N que completa el sector de neutrinos a través de un mecanismo de see-saw inverso a la escala del TeV. La partícula χ puede aniquilarse en un neutrino monocromático a través del Higgs portal. El modelo tiene tres acoplamientos independientes (c_s, c_a, y c_N), dos masas (m_χ y m_N) y una mezcla entre partículas ligeras y pesadas (s_α). En experimentos de detección directa, la contribución de c_a y c_N es irrelevante, por lo que podemos usarlos para reproducir la abundancia reliquia necesaria para explicar la materia oscura, $\Omega_{\rm DM}h^2 = 0.12$. c_s, a su vez, fija la señal en búsquedas directas y el ritmo de captura del Sol, que tambien calculamos en este capítulo. Las figuras 3.11 y 3.12 muestran la señal, muy por encima del fondo, que podríamos esperar para masas de WIMP de 300 GeV y 1 TeV, respectivamente.

La parte experimental de esta tesis también consta de dos capítulos. En el Capítulo 4 describimos KM3NeT, un telescopio de neutrinos que está siendo construido en el Mar Mediterráneo. El experimento está compuesto por dos detectores, ARCA y ORCA, localizados en Italia y Francia, respectivamente. Entre los numeros análisis que se están llevando a cabo en la colaboración KM3NeT también encontramos búsquedas de materia oscura en diferentes fuentes astrofísicas. En particular, el Sol es una de las más prometedoras debido a su proximidad y tamaño.

Posteriormente, en el Capítulo 5, analizamos un set de datos del telescopio de neutrinos ORCA en su configuración con 6 *Detection Units*, que contiene un *livetime* o *tiempo de vida* de 553 días. Consideramos partículas tipo WIMP que se aniquilan en $\tau^+\tau^-$, W^+W^- o $b\bar{b}$, asumiendo en cada caso un *Branching Ratio* del 100%. Para cada canal de aniquilación y masa de WIMP, caracterizamos la señal y el fondo utilizando el software WimpSim [165] junto con las PSFs y PDFs obtenidas a partir del Monte Carlo de la colaboración y de los datos *scrambled*. A continuación, construimos 10^4 Pseudo-experimentos y evaluamos cada mapa celeste con una función Likelihood. La minimización de esta función nos proporciona el

número de eventos de señal reconstruidos para cada mapa celeste, n_{reco}. Después hemos obtenido la distribución del Test Statistic, aplicando un smearing de Poisson. Con esto deducimos el valor del n_{90} y calculamos la sensibilidad al flujo de neutrinos producido en aniquilaciones de WIMP. Finalmente, realizamos un *unblinding* de los datos – es decir, repetimos el proceso pero esta vez utilizando el conjunto de datos reales en lugar de los datos scrambled – y no encontramos ningún exceso de señal sobre el fondo esperado. Basándonos en este resultado, establecemos límites en la sensibilidad, que posteriormente se convierten en límites en la sección eficaz para colisiones de materia oscura con nucleones. Nuestro análisis no encuentra una ninguna señal, pero establece límites competitivos (ver Figuras 5.22 y 5.23), lo que demuestra el potencial del detector KM3NeT/ORCA y la infraestructura de KM3NeT para hacer descubrimientos en el futuro, una vez que se complete en su configuración final.

Concluimos que, a pesar de décadas de búsquedas que limitan su espacio de parámetros, el paradigma WIMP aún es viable. Además, la posibilidad de investigarlo en una gran variedad de experimentos diferentes, que es básicamente lo que lo hace tan interesante, aún permanece.

Appendix

A

Fit to atmospheric and solar neutrino fluxes

Here we provide approximate fits for the atmospheric and solar fluxes integrated over the angular region ($\Delta\Omega_\odot$) occupied by the Sun. In these expressions E is in GeV and t in years ($t = 0$ at the solar minimum), whereas $\Delta\Omega_\odot\, \Phi^{\rm atm}_{\nu_\mu}$ is given in GeV cm^{-2} s^{-1}. The angle $\theta^*(\theta_z)$ is defined in [55, 60]:

$$\tan\theta^* = \frac{R_\oplus \sin\theta_z}{\sqrt{R_\oplus^2 \cos^2\theta_z + (2R_\oplus + h)\, h}}\,. \tag{A.1}$$

For the atmospheric flux we have

$$\Delta\Omega_\odot\, \Phi^{\rm atm}_{\nu_\mu}(E,\theta) = 0.068\; E^{-2.97-0.0109\log E - 0.00139\log^2 E}\; F_1^{\rm atm}(E,\theta)\,; \tag{A.2}$$

$$\Delta\Omega_\odot\, \Phi^{\rm atm}_{\nu_e}(E,\theta) = 0.030\; E^{-3.30-0.0364\log^{1.35} E + 0.0103\log^{1.85} E}\; F_2^{\rm atm}(E,\theta) \tag{A.3}$$

with

$$F_1^{\rm atm}(E,\theta) = \frac{\left(\frac{176}{E}\right)^{0.6} + \cos[\theta^*(\frac{\pi}{4})]}{\left(\frac{176}{E}\right)^{0.6} + \cos[\theta^*(\theta_z)]}\,;\quad F_2^{\rm atm}(E,\theta) = \frac{\left(\frac{7.5\times10^{-4}}{E}\right)^{0.21} + \cos[\theta^*(\frac{\pi}{4})]}{\left(\frac{7.5\times10^{-4}}{E}\right)^{0.21} + \cos[\theta^*(\theta_z)]}\,. \tag{A.4}$$

For the atmospheric neutrinos from both the CR shadow of the Sun and solar neutrons,

$$\Delta\Omega_\odot\, \Phi^{\rm shad+n}_{\nu_\mu}(E,\theta,t) = 0.0670\; E^{G_1^{\rm atm}(E,t)}\; F_2^{\rm atm}(E,\theta)\,; \tag{A.5}$$

$$\Delta\Omega_\odot\, \Phi^{\rm shad+n}_{\nu_e}(E,\theta,t) = 0.0212\; E^{G_2^{\rm shad+n}(E,t)}\; F_2^{\rm atm}(E,\theta) \tag{A.6}$$

with

$$\begin{aligned} G_1^{\rm shad+n}(E,t) = &-2.98 - 0.017\log E + 0.012\cos\frac{2\pi t}{11}\log^2 E - \\ &3.3\times10^{-4}\log^3 E - 3.9\times10^{-6}\log^5 E\,; \end{aligned} \tag{A.7}$$

$$G_2^{\text{shad+n}}(E,t) = -3.1 - 0.061\log E - \cos\frac{2\pi t}{11}\left(0.00305\log E + 2.1\times10^{-6}\log^5 E\right) - 5.4\times10^{-7}\log^6 E\,. \tag{A.8}$$

Finally, the neutrinos produced in the Sun come in the three flavors with the same frequency and

$$\Delta\Omega_\odot\,\Phi^\odot_{\nu_i}(E,t) = \left(0.917\times10^{-4} - \frac{0.037\sin^2\frac{\pi t}{11}}{900+E}\right) \times E^{-1.20-0.1\log E-0.0042\log^2 E+1.6\times10^{-5}\log^4 E}\,. \tag{A.9}$$

Bibliography

[1] S. L. Glashow. "Partial Symmetries of Weak Interactions". In: *Nucl. Phys.* 22 (1961), pp. 579–588. DOI: 10.1016/0029-5582(61)90469-2.

[2] S. Weinberg. "A Model of Leptons". In: *Phys. Rev. Lett.* 19 (1967), pp. 1264–1266. DOI: 10.1103/PhysRevLett.19.1264.

[3] Y. Nambu. "Relativistic groups and infinite-component fields". In: *8th Nobel Symposium*. 1968.

[4] C.-N. Yang and R. L. Mills. "Conservation of Isotopic Spin and Isotopic Gauge Invariance". In: *Phys. Rev.* 96 (1954). Ed. by J.-P. Hsu and D. Fine, pp. 191–195. DOI: 10.1103/PhysRev.96.191.

[5] A. Einstein. "The Field Equations of Gravitation". In: *Sitzungsber. Preuss. Akad. Wiss. Berlin (Math. Phys.)* 1915 (1915), pp. 844–847.

[6] *Physics at LEP: CERN, Geneva, Switzerland 19 Mar 1985. LEP Physics Jamboree*. CERN. Geneva: CERN, 1986. DOI: 10.5170/CERN-1986-002-V-1. URL: https://cds.cern.ch/record/166310.

[7] W. de Boer. "Precision Experiments at LEP". In: *Adv. Ser. Direct. High Energy Phys.* 23 (2015), pp. 107–136. DOI: 10.1142/9789814644150_0005. arXiv: 1509.06050 [hep-ex].

[8] D. Hanneke, S. Fogwell, and G. Gabrielse. "New Measurement of the Electron Magnetic Moment and the Fine Structure Constant". In: *Phys. Rev. Lett.* 100 (2008), p. 120801. DOI: 10.1103/PhysRevLett.100.120801. arXiv: 0801.1134 [physics.atom-ph].

[9] C. G. Callan Jr., R. F. Dashen, and D. J. Gross. "The Structure of the Gauge Theory Vacuum". In: *Phys. Lett. B* 63 (1976). Ed. by J. C. Taylor, pp. 334–340. DOI: 10.1016/0370-2693(76)90277-X.

[10] R. Jackiw and C. Rebbi. "Vacuum Periodicity in a Yang-Mills Quantum Theory". In: *Phys. Rev. Lett.* 37 (1976). Ed. by J. C. Taylor, pp. 172–175. DOI: 10.1103/PhysRevLett.37.172.

[11] M. Magg and Ch. Wetterich. "Neutrino mass problem and gauge hierarchy". In: *Physics Letters B* 94.1 (1980), pp. 61–64. ISSN: 0370-2693. DOI: https://doi.org/10.1016/0370-2693(80)90825-4. URL: https://www.sciencedirect.com/science/article/pii/0370269380908254.

[12] R. D. Peccei and H. R. Quinn. "CP Conservation in the Presence of Instantons". In: *Phys. Rev. Lett.* 38 (1977), pp. 1440–1443. DOI: 10.1103/PhysRevLett.38.1440.

[13] V. Trimble. "Existence and Nature of Dark Matter in the Universe". In: *Ann. Rev. Astron. Astrophys.* 25 (1987), pp. 425–472. DOI: 10.1146/annurev.aa.25.090187.002233.

[14] A. G. Riess et al. "Observational evidence from supernovae for an accelerating universe and a cosmological constant". In: *Astron. J.* 116 (1998), pp. 1009–1038. DOI: 10.1086/300499. arXiv: astro-ph/9805201.

[15] R. M. Wald. *Quantum Field Theory in Curved Space-Time and Black Hole Thermodynamics*. Chicago Lectures in Physics. Chicago, IL: University of Chicago Press, 1995. ISBN: 978-0-226-87027-4.

[16] C. Rovelli. *Quantum gravity*. Cambridge Monographs on Mathematical Physics. Cambridge, UK: Univ. Pr., 2004. DOI: 10.1017/CBO9780511755804.

[17] S. O. Bilson-Thompson, F. Markopoulou, and L. Smolin. "Quantum gravity and the standard model". In: *Class. Quant. Grav.* 24 (2007), pp. 3975–3994. DOI: 10.1088/0264-9381/24/16/002. arXiv: hep-th/0603022.

[18] E. Gildener and S. Weinberg. "Symmetry Breaking and Scalar Bosons". In: *Phys. Rev. D* 13 (1976), p. 3333. DOI: 10.1103/PhysRevD.13.3333.

[19] W. Pauli. "Pauli letter collection: letter to Lise Meitner". Typed copy. URL: https://cds.cern.ch/record/83282.

[20] P. A. Zyla et al. "Review of Particle Physics". In: *PTEP* 2020.8 (2020), p. 083C01. DOI: 10.1093/ptep/ptaa104.

[21] A. Connolly, R. S. Thorne, and D. Waters. "Calculation of High Energy Neutrino-Nucleon Cross Sections and Uncertainties Using the MSTW Parton Distribution Functions and Implications for Future Experiments". In: *Phys. Rev. D* 83 (2011), p. 113009. DOI: 10.1103/PhysRevD.83.113009. arXiv: 1102.0691 [hep-ph].

[22] M. G. Aartsen et al. "Evidence for High-Energy Extraterrestrial Neutrinos at the IceCube Detector". In: *Science* 342 (2013), p. 1242856. DOI: 10.1126/science.1242856. arXiv: 1311.5238 [astro-ph.HE].

[23] P. Meszaros. "Astrophysical Sources of High Energy Neutrinos in the IceCube Era". In: *Ann. Rev. Nucl. Part. Sci.* 67 (2017), pp. 45–67. DOI: 10.1146/annurev-nucl-101916-123304. arXiv: 1708.03577 [astro-ph.HE].

[24] G. Sirri. "The CNGS neutrino beam". In: *Nucl. Phys. B Proc. Suppl.* 172 (2007). Ed. by P. S. Marrocchesi, F. L. Navarria, M. Paganoni, and P. G. Pelfer, pp. 149–151. DOI: 10.1016/j.nuclphysbps.2007.08.145.

[25] T. K. Gaisser. "The Atmospheric Neutrino Flux". In: *Ch. 3 in Probing Particle Physics with Neutrino Telescopes. World Scientific* ISBN: 9789813275010 (2020). Ed. by C. Pérez de los Heros. arXiv: 1910.08851 [astro-ph.HE].

[26] A. Mirizzi et al. "Supernova Neutrinos: Production, Oscillations and Detection". In: *Riv. Nuovo Cim.* 39.1-2 (2016), pp. 1–112. DOI: 10.1393/ncr/i2016-10120-8. arXiv: 1508.00785 [astro-ph.HE].

[27] H. Netzer. "Revisiting the Unified Model of Active Galactic Nuclei". In: *Ann. Rev. Astron. Astrophys.* 53 (2015), pp. 365–408. DOI: 10.1146/annurev-astro-082214-122302. arXiv: 1505.00811 [astro-ph.GA].

[28] U. F. Katz and Ch. Spiering. "High-Energy Neutrino Astrophysics: Status and Perspectives". In: *Prog. Part. Nucl. Phys.* 67 (2012), pp. 651–704. DOI: 10.1016/j.ppnp.2011.12.001. arXiv: 1111.0507 [astro-ph.HE].

[29] J. C. Street and E. C. Stevenson. "New Evidence for the Existence of a Particle of Mass Intermediate Between the Proton and Electron". In: *Phys. Rev.* 52 (1937), pp. 1003–1004. DOI: 10.1103/PhysRev.52.1003.

[30] D. E. Groom, N. V. Mokhov, and S. I. Striganov. "Muon stopping power and range tables 10-MeV to 100-TeV". In: *Atom. Data Nucl. Data Tabl.* 78 (2001), pp. 183–356. DOI: 10.1006/adnd.2001.0861.

[31] M. Masip. "High energy neutrinos from the Sun". In: *Astropart. Phys.* 97 (2018), pp. 63–68. DOI: 10.1016/j.astropartphys.2017.11.003. arXiv: 1706.01290 [hep-ph].

[32] E. P. Cherenkova. "The discovery of the Cherenkov radiation". In: *Nucl. Instrum. Meth. A* 595 (2008). Ed. by A. Bressan, S. Dalla Torre, B. Gobbo, and F. Tessarotto, pp. 8–11. DOI: 10.1016/j.nima.2008.07.006.

[33] P. A. Cherenkov. "Visible luminescence of pure liquids under the influence of γ-radiation". In: *Dokl. Akad. Nauk SSSR* 2.8 (1934), pp. 451–454. DOI: 10.3367/UFNr.0093.196710n.0385.

[34] P. A. Cherenkov. "Visible radiation produced by electrons moving in a medium with velocities exceeding that of light". In: *Phys. Rev.* 52.4 (1937), pp. 378–379. DOI: 10.1103/PhysRev.52.378.

[35] J. Hofestädt on behalf of theKM3NeT Collaboration. "Measuring the neutrino mass hierarchy with KM3NeT/ORCA". In: *Journal of Physics: Conference Series* 1342.1 (Jan. 2020), p. 012028. DOI: 10.1088/1742-6596/1342/1/012028. URL: https://dx.doi.org/10.1088/1742-6596/1342/1/012028.

[36] J. J. Hernández Rey, N. R. Khan Chowdhury, J. Manczak, S. Navas, and J. D. Zornoza. "Search for neutrino non-standard interactions with ANTARES and KM3NeT-ORCA". In: *JINST* 16.09 (2021), p. C09016. DOI: 10.1088/1748-0221/16/09/C09016. arXiv: 2107.14296 [hep-ex].

[37] D. N. Spergel et al. "First year Wilkinson Microwave Anisotropy Probe (WMAP) observations: Determination of cosmological parameters". In: *Astrophys. J. Suppl.* 148 (2003), pp. 175–194. DOI: 10.1086/377226. arXiv: astro-ph/0302209.

[38] M. S. Turner. "Λ CDM: Much More Than We Expected, but Now Less Than What We Want". In: *Found. Phys.* 48.10 (2018), pp. 1261–1278. DOI: 10.1007/s10701-018-0178-8. arXiv: 2109.01760 [astro-ph.CO].

[39] D. Brout et al. "The Pantheon+ Analysis: Cosmological Constraints". In: *Astrophys. J.* 938.2 (2022), p. 110. DOI: 10.3847/1538-4357/ac8e04. arXiv: 2202.04077 [astro-ph.CO].

[40] A. Sneppen et al. "Measuring the Hubble constant with kilonovae using the expanding photosphere method". In: *Astron. Astrophys.* 678 (2023), A14. DOI: 10.1051/0004-6361/202346306. arXiv: 2306.12468 [astro-ph.CO].

[41] G. Jungman, M. Kamionkowski, and K. Griest. "Supersymmetric dark matter". In: *Phys. Rept.* 267 (1996), pp. 195–373. DOI: 10.1016/0370-1573(95)00058-5. arXiv: hep-ph/9506380.

[42] J. M. Cline. "TASI Lectures on Early Universe Cosmology: Inflation, Baryogenesis and Dark Matter". In: *PoS* TASI2018 (2019), p. 001. arXiv: 1807.08749 [hep-ph].

[43] L. Husdal. "On Effective Degrees of Freedom in the Early Universe". In: *Galaxies* 4.4 (2016), p. 78. DOI: 10.3390/galaxies4040078. arXiv: 1609.04979 [astro-ph.CO].

[44] E. W. Kolb and M. S. Turner. *The Early Universe*. Vol. 69. 1990. ISBN: 978-0-201-62674-2. DOI: 10.1201/9780429492860.

[45] M. Cannoni. "Relativistic and nonrelativistic annihilation of dark matter: a sanity check using an effective field theory approach". In: *Eur. Phys. J. C* 76.3 (2016), p. 137. DOI: 10.1140/epjc/s10052-016-3991-2. arXiv: 1506.07475 [hep-ph].

[46] V. Hess. "Über Beobachtungen der durchdringenden Strahlung bei sieben Freiballonfahrten". In: *Phys. Z.* 13 (1912), pp. 1084–1091.

[47] V. Hess. "On the Observations of the Penetrating Radiation during Seven Balloon Flights". In: (July 2018). arXiv: 1808.02927 [physics.hist-ph].

[48] *University of Hamburg,* https://www.physik.uni-hamburg.de/iexp/groups/astroparticle/score/en/physics/.

[49] A. Haungs et al. "Investigating the 2nd knee: The KASCADE-Grande experiment". In: *J. Phys. Conf. Ser.* 47 (2006), p. 238. DOI: 10.1088/1742-6596/47/1/029. arXiv: astro-ph/0508286.

[50] W. D. Apel et al. "Kneelike structure in the spectrum of the heavy component of cosmic rays observed with KASCADE-Grande". In: *Phys. Rev. Lett.* 107 (2011), p. 171104. DOI: 10.1103/PhysRevLett.107.171104. arXiv: 1107.5885 [astro-ph.HE].

[51] *Caltech,* https://izw1.caltech.edu/ACE/ACENews/ACENews83.html.

[52] F. G. Schröder. "Radio detection of Extensive Air Showers". In: *25th European Cosmic Ray Symposium*. Jan. 2017. arXiv: 1701.05496 [astro-ph.HE].

[53] F. Riehn et al. "The hadronic interaction model SIBYLL 2.3c and Feynman scaling". In: *PoS* ICRC2017 (2018), p. 301. DOI: 10.22323/1.301.0301. arXiv: 1709.07227 [hep-ph].

[54] S. M. Barr, T. K. Gaisser, P. Lipari, and S. Tilav. "Ratio of ν_e/ν_μ in Atmospheric Neutrinos". In: *Phys. Lett. B* 214 (1988), pp. 147–150. DOI: 10.1016/0370-2693(88)90468-6.

[55] P. Lipari. "Lepton spectra in the earth's atmosphere". In: *Astropart. Phys.* 1 (1993), pp. 195–227. DOI: 10.1016/0927-6505(93)90022-6.

[56] B. Rossi and K. Greisen. "Cosmic-ray theory". In: *Rev. Mod. Phys.* 13 (1941), pp. 240–309. DOI: 10.1103/RevModPhys.13.240.

[57] D. Heck, J. Knapp, J. N. Capdevielle, G. Schatz, and T. Thouw. "CORSIKA: A Monte Carlo code to simulate extensive air showers". In: (Feb. 1998).

[58] T. K. Gaisser and M. Honda. "Flux of atmospheric neutrinos". In: *Ann. Rev. Nucl. Part. Sci.* 52 (2002), pp. 153–199. DOI: 10.1146/annurev.nucl.52.050102.090645. arXiv: hep-ph/0203272.

[59] W. Bai et al. "Forward production of prompt neutrinos from charm in the atmosphere and at high energy colliders". In: *JHEP* 10 (2023), p. 142. DOI: 10.1007/JHEP10(2023)142. arXiv: 2212.07865 [hep-ph].

[60] M. Gutiérrez, G. Hernández-Tomé, J. I. Illana, and M. Masip. "Neutrino events within muon bundles at neutrino telescopes". In: *Astropart. Phys.* 134-135 (2022), p. 102646. DOI: 10.1016/j.astropartphys.2021.102646. arXiv: 2106.01212 [hep-ph].

[61] M. Gutiérrez, M. Masip, and S. Muñoz. "The Solar Disk at High Energies". In: *Astrophys. J.* 941.1 (2022), p. 86. DOI: 10.3847/1538-4357/aca020. arXiv: 2206.00964 [astro-ph.HE].

[62] D. Seckel, T. Stanev, and T. K. Gaisser. "Albedo gamma-ray from cosmic ray interactions on the solar surface". In: *AIP Conf. Proc.* 220 (1991). Ed. by J. Matthews, pp. 227–231. DOI: 10.1063/1.40299.

[63] J. Christensen-Dalsgaard et al. "The Current State of Solar Modeling". In: *Science* 272.5266 (1996), pp. 1286–1292. DOI: 10.1126/science.272.5266.1286. eprint: https://www.science.org/doi/pdf/10.1126/science.272.5266.1286. URL: https://www.science.org/doi/abs/10.1126/science.272.5266.1286.

[64] N. Vinyoles and Serenelliet al. "A new Generation of Standard Solar Models". In: *Astrophys. J.* 835.2 (2017), p. 202. DOI: 10.3847/1538-4357/835/2/202. arXiv: 1611.09867 [astro-ph.SR].

[65] M. Asplund, N. Grevesse, A. J.s Sauval, and P. Scott. "The Chemical Composition of the Sun". In: *ARAA* 47.1 (2009), pp. 481–522. DOI: 10.1146/annurev.astro.46.060407.145222. arXiv: 0909.0948 [astro-ph.SR].

[66] M. Amenomori et al. "Probe of the Solar Magnetic Field Using the "Cosmic-Ray Shadow" of the Sun". In: *Phys. Rev. Lett.* 111.1 (2013), p. 011101. DOI: 10.1103/PhysRevLett.111.011101. arXiv: 1306.3009 [astro-ph.SR].

[67] A. Albert et al. "Observation of the cosmic ray shadow of the Sun with the ANTARES neutrino telescope". In: *Phys. Rev. D* 102.12 (2020), p. 122007. DOI: 10.1103/PhysRevD.102.122007. arXiv: 2007.00931 [astro-ph.HE].

[68] S. Aiello et al. "First observation of the cosmic ray shadow of the Moon and the Sun with KM3NeT/ORCA". In: *Eur. Phys. J. C* 83.4 (2023), p. 344. DOI: 10.1140/epjc/s10052-023-11401-5. arXiv: 2211.08977 [astro-ph.IM].

[69] E. N. Parker. "Dynamics of the Interplanetary Gas and Magnetic Fields". In: *Astrophys. J.* 128 (1958), pp. 664–676. DOI: 10.1086/146579.

[70] R. C. Tautz, A. Shalchi, and A. Dosch. "Simulating Heliospheric and Solar Particle Diffusion using the Parker Spiral Geometry". In: *J. Geophys. Res.* 116.A2 (2011), A02102. DOI: 10.1029/2010JA015936. arXiv: 1011.3325 [astro-ph.HE].

[71] D. Seckel, Todor Stanev, and T. K. Gaisser. "Signatures of cosmic-ray interactions on the solar surface". In: *Astrophys. J.* 382 (1991), pp. 652–666. DOI: 10.1086/170753.

[72] M. N. Mazziotta et al. "Cosmic-ray interactions with the Sun using the FLUKA code". In: *Phys. Rev. D* 101.8 (2020), p. 083011. DOI: 10.1103/PhysRevD.101.083011. arXiv: 2001.09933 [astro-ph.HE].

[73] O. Enriquez-Rivera and A. Lara. "The Galactic cosmic-ray Sun shadow observed by HAWC". In: *PoS* ICRC2015 (2016), p. 099. DOI: 10.22323/1.236.0099. arXiv: 1508.07351 [astro-ph.SR].

[74] A. Albert et al. "First HAWC Observations of the Sun Constrain Steady TeV Gamma-Ray Emission". In: *Phys. Rev. D* 98.12 (2018), p. 123011. DOI: 10.1103/PhysRevD.98.123011. arXiv: 1808.05620 [astro-ph.HE].

[75] J. Edsjo, J. Elevant, R. Enberg, and C. Niblaeus. "Neutrinos from cosmic ray interactions in the Sun". In: *JCAP* 06 (2017), p. 033. DOI: 10.1088/1475-7516/2017/06/033. arXiv: 1704.02892 [astro-ph.HE].

[76] Kenny C. Y. Ng, John F. Beacom, Annika H. G. Peter, and Carsten Rott. "Solar Atmospheric Neutrinos: A New Neutrino Floor for Dark Matter Searches". In: *Phys. Rev. D* 96.10 (2017), p. 103006. DOI: 10.1103/PhysRevD.96.103006. arXiv: 1703.10280 [astro-ph.HE].

[77] C. A. Argüelles, G. de Wasseige, A. Fedynitch, and B. J. P. Jones. "Solar Atmospheric Neutrinos and the Sensitivity Floor for Solar Dark Matter Annihilation Searches". In: *JCAP* 07 (2017), p. 024. DOI: 10.1088/1475-7516/2017/07/024. arXiv: 1703.07798 [astro-ph.HE].

[78] T. Linden et al. "Evidence for a New Component of High-Energy Solar Gamma-Ray Production". In: *Phys. Rev. Lett.* 121.13 (2018), p. 131103. DOI: 10.1103/PhysRevLett.121.131103. arXiv: 1803.05436 [astro-ph.HE].

[79] A. Albert et al. "Discovery of Gamma Rays from the Quiescent Sun with HAWC". In: *Phys. Rev. Lett.* 131.5 (2023), p. 051201. DOI: 10.1103/PhysRevLett.131.051201. arXiv: 2212.00815 [astro-ph.HE].

[80] Q.-W. Tang et al. "Unexpected dip in the solar gamma-ray spectrum". In: *Phys. Rev. D* 98.6 (2018), p. 063019. DOI: 10.1103/PhysRevD.98.063019. arXiv: 1804.06846 [astro-ph.HE].

[81] M. G. Aartsen et al. "Detection of the Temporal Variation of the Sun's Cosmic Ray Shadow with the IceCube Detector". In: *Astrophys. J.* 872.2 (2019), p. 133. DOI: 10.3847/1538-4357/aaffd1. arXiv: 1811.02015 [astro-ph.HE].

[82] M. G. Aartsen et al. "Measurements of the time-dependent cosmic-ray Sun shadow with seven years of IceCube data: Comparison with the Solar cycle and magnetic field models". In: *Phys. Rev. D* 103.4 (2021), p. 042005. DOI: 10.1103/PhysRevD.103.042005. arXiv: 2006.16298 [astro-ph.HE].

[83] A. Achterberg et al. "First Year Performance of The IceCube Neutrino Telescope". In: *Astropart. Phys.* 26 (2006), pp. 155–173. DOI: 10.1016/j.astropartphys.2006.06.007. arXiv: astro-ph/0604450.

[84] S. Adrian-Martinez et al. "Letter of intent for KM3NeT 2.0". In: *J. Phys. G* 43.8 (2016), p. 084001. DOI: 10.1088/0954-3899/43/8/084001. arXiv: 1601.07459 [astro-ph.IM].

[85] G. L. Fogli, E. Lisi, A. Mirizzi, D. Montanino, and P. D. Serpico. "Oscillations of solar atmosphere neutrinos". In: *Phys. Rev. D* 74 (2006), p. 093004. DOI: 10.1103/PhysRevD.74.093004. arXiv: hep-ph/0608321.

[86] M. Gutiérrez and M. Masip. "The Sun at TeV energies: gammas, neutrons, neutrinos and a cosmic ray shadow". In: *Astropart. Phys.* 119 (2020), pp. 102–440. DOI: 10.1016/j.astropartphys.2020.102440. arXiv: 1911.07530 [hep-ph].

[87] E. Christian et al. "New Data from the IS IS instrument Suite on Parker Solar Probe". In: *PoS* ICRC2021 (2021), p. 1306. DOI: 10.22323/1.395.1306.

[88] O. E. Malandraki et al. "Energetic particle observations close to the Sun by Solar Orbiter and Parker Solar Probe". In: *PoS* ICRC2021 (2022), p. 040. DOI: 10.22323/1.395.0040.

[89] M. Ardid., I. Felis, Moritz Lotze, and Christoph Tönnis. "Neutrinos from Cosmic Ray Interactions in the Sun as background for dark matter searches". In: *PoS* ICRC2017 (2018), p. 907. DOI: 10.22323/1.301.0907.

[90] M. G. Aartsen et al. "Searches for neutrinos from cosmic-ray interactions in the Sun using seven years of IceCube data". In: (Dec. 2019). DOI: 10.1088/1475-7516/2021/02/025. arXiv: 1912.13135 [astro-ph.HE].

[91] J. Villarreal et al. "Recent Progress in Solar Atmospheric Neutrino Searches with IceCube". In: *PoS* ICRC2021 (2021), p. 1174. DOI: 10.22323/1.395.1174. arXiv: 2107.13696 [astro-ph.HE].

[92] A. Albert et al. "Search for solar atmospheric neutrinos with the ANTARES neutrino telescope". In: *JCAP* 06.06 (2022), p. 018. DOI: 10.1088/1475-7516/2022/06/018. arXiv: 2201.11642 [astro-ph.HE].

[93] J. Berger et al. "Snowmass 2021 White Paper: Cosmogenic Dark Matter and Exotic Particle Searches in Neutrino Experiments". In: *Snowmass 2021*. July 2022. arXiv: 2207.02882 [hep-ph].

[94] E. Aprile et al. "Dark Matter Search Results from a One Ton-Year Exposure of XENON1T". In: *Phys. Rev. Lett.* 121.11 (2018), p. 111302. DOI: 10.1103/PhysRevLett.121.111302. arXiv: 1805.12562 [astro-ph.CO].

[95] N. Wyn Evans, Ciaran A. J. O'Hare, and Christopher McCabe. "Refinement of the standard halo model for dark matter searches in light of the Gaia Sausage". In: *Phys. Rev. D* 99.2 (2019), p. 023012. DOI: 10.1103/PhysRevD.99.023012. arXiv: 1810.11468 [astro-ph.GA].

[96] S. Chandrasekhar. *An introduction to the study of stellar structure*. 1939.

[97] A. Liam Fitzpatrick, Wick Haxton, Emanuel Katz, Nicholas Lubbers, and Yiming Xu. "The Effective Field Theory of Dark Matter Direct Detection". In: *JCAP* 02 (2013), p. 004. DOI: 10.1088/1475-7516/2013/02/004. arXiv: 1203.3542 [hep-ph].

[98] R. Catena and B. Schwabe. "Form factors for dark matter capture by the Sun in effective theories". In: *JCAP* 04 (2015), p. 042. DOI: 10.1088/1475-7516/2015/04/042. arXiv: 1501.03729 [hep-ph].

[99] PICO Collaboration. "Dark Matter Search Results from the Complete Exposure of the PICO-60 C_3F_8 Bubble Chamber". In: *Phys. Rev. D* 100.2 (2019), p. 022001. DOI: 10.1103/PhysRevD.100.022001. arXiv: 1902.04031 [astro-ph.CO].

[100] G. Arcadi, A. Djouadi, and M. Raidal. "Dark Matter through the Higgs portal". In: *Phys. Rept.* 842 (2020), pp. 1–180. DOI: 10.1016/j.physrep.2019.11.003. arXiv: 1903.03616 [hep-ph].

[101] R. N. Mohapatra and J. W. F. Valle. "Neutrino Mass and Baryon Number Nonconservation in Superstring Models". In: *Phys. Rev. D* 34 (1986), p. 1642. DOI: 10.1103/PhysRevD.34.1642.

[102] A. Ibarra, E. Molinaro, and S. T. Petcov. "TeV Scale See-Saw Mechanisms of Neutrino Mass Generation, the Majorana Nature of the Heavy Singlet Neutrinos and $(\beta\beta)_{0\nu}$-Decay". In: *JHEP* 09 (2010), p. 108. DOI: 10.1007/JHEP09(2010)108. arXiv: 1007.2378 [hep-ph].

[103] A. J. Cuesta, M. E. Gómez, J. I. Illana, and M. Masip. "Cosmology of an axion-like majoron". In: *JCAP* 04.04 (2022), p. 009. DOI: 10.1088/1475-7516/2022/04/009. arXiv: 2109.07336 [hep-ph].

[104] A. J. Cuesta, J. I. Illana, and M. Masip. "Photon to axion conversion during Big Bang Nucleosynthesis". In: *JCAP* 11 (2023), p. 103. DOI: 10.1088/1475-7516/2023/11/103. arXiv: 2305.16838 [hep-ph].

[105] E. Fernandez-Martinez, J. Hernandez-Garcia, and J. Lopez-Pavon. "Global constraints on heavy neutrino mixing". In: *JHEP* 08 (2016), p. 033. DOI: 10.1007/JHEP08(2016)033. arXiv: 1605.08774 [hep-ph].

[106] G. Hernández-Tomé, J. I. Illana, M. Masip, G. López Castro, and P. Roig. "Effects of heavy Majorana neutrinos on lepton flavor violating processes". In: *Phys. Rev. D* 101.7 (2020), p. 075020. DOI: 10.1103/PhysRevD.101.075020. arXiv: 1912.13327 [hep-ph].

[107] G. Hernández-Tomé, J. I. Illana, and M. Masip. "The ρ parameter and $H^0 \to \ell_i \ell_j$ in models with TeV sterile neutrinos". In: *Phys. Rev. D* 102.11 (2020), p. 113006. DOI: 10.1103/PhysRevD.102.113006. arXiv: 2005.11234 [hep-ph].

[108] J. M. Cline, K. Kainulainen, P. Scott, and Ch. Weniger. "Update on scalar singlet dark matter". In: *Phys. Rev. D* 88 (2013). [Erratum: Phys.Rev.D 92, 039906 (2015)], p. 055025. DOI: 10.1103/PhysRevD.88.055025. arXiv: 1306.4710 [hep-ph].

[109] J. Alberto Casas, David G. Cerdeño, Jesus M. Moreno, and Javier Quilis. "Reopening the Higgs portal for single scalar dark matter". In: *JHEP* 05 (2017), p. 036. DOI: 10.1007/JHEP05(2017)036. arXiv: 1701.08134 [hep-ph].

[110] J. M. Alarcon, J. Martin Camalich, and J. A. Oller. "The chiral representation of the πN scattering amplitude and the pion-nucleon sigma term". In: *Phys. Rev. D* 85 (2012), p. 051503. DOI: 10.1103/PhysRevD.85.051503. arXiv: 1110.3797 [hep-ph].

[111] A. Abdel-Rehim et al. "Direct Evaluation of the Quark Content of Nucleons from Lattice QCD at the Physical Point". In: *Phys. Rev. Lett.* 116.25 (2016), p. 252001. DOI: 10.1103/PhysRevLett.116.252001. arXiv: 1601.01624 [hep-lat].

[112] R. Garani and S. Palomares-Ruiz. "Evaporation of dark matter from celestial bodies". In: *JCAP* 05.05 (2022), p. 042. DOI: 10.1088/1475-7516/2022/05/042. arXiv: 2104.12757 [hep-ph].

[113] R. Garani and S. Palomares-Ruiz. "Dark matter in the Sun: scattering off electrons vs nucleons". In: *JCAP* 05 (2017), p. 007. DOI: 10.1088/1475-7516/2017/05/007. arXiv: 1702.02768 [hep-ph].

[114] K. Griest and D. Seckel. "Cosmic Asymmetry, Neutrinos and the Sun". In: *Nucl. Phys. B* 283 (1987). [Erratum: Nucl.Phys.B 296, 1034–1036 (1988)], pp. 681–705. DOI: 10.1016/0550-3213(87)90293-8.

[115] Q. Liu, J. Lazar, C. A. Argüelles, and A. Kheirandish. "χaroν: a tool for neutrino flux generation from WIMPs". In: *JCAP* 10 (2020), p. 043. DOI: 10.1088/1475-7516/2020/10/043. arXiv: 2007.15010 [hep-ph].

[116] S. Schael et al. "Precision electroweak measurements on the Z resonance". In: *Phys. Rept.* 427 (2006), pp. 257–454. DOI: 10.1016/j.physrep.2005.12.006. arXiv: hep-ex/0509008.

[117] G. Aad et al. "Measurements of Higgs boson production by gluon-gluon fusion and vector-boson fusion using $H \to WW^* \to e\nu\mu\nu$ decays in pp collisions at $\sqrt{s} = 13$ TeV with the ATLAS detector". In: *Phys. Rev. D* 108 (2023), p. 032005. DOI: 10.1103/PhysRevD.108.032005. arXiv: 2207.00338 [hep-ex].

[118] G. Aad et al. "Fiducial and differential cross-section measurements for the vector-boson-fusion production of the Higgs boson in the $H \to WW^* \to e\nu\mu\nu$ decay channel at 13 TeV with the ATLAS detector". In: *Phys. Rev. D* 108.7 (2023), p. 072003. DOI: 10.1103/PhysRevD.108.072003. arXiv: 2304.03053 [hep-ex].

[119] "Combination of searches for invisible decays of the Higgs boson using 139 fb−1 of proton-proton collision data at s=13 TeV collected with the ATLAS experiment". In: *Phys. Lett. B* 842 (2023), p. 137963. DOI: 10.1016/j.physletb.2023.137963. arXiv: 2301.10731 [hep-ex].

[120] G. Aad et al. "Search for dark matter produced in association with a Higgs boson decaying to tau leptons at $\sqrt{s} = 13$ TeV with the ATLAS detector". In: *JHEP* 09 (2023), p. 189. DOI: 10.1007/JHEP09(2023)189. arXiv: 2305.12938 [hep-ex].

[121] A. Djouadi, O. Lebedev, Y. Mambrini, and J. Quevillon. "Implications of LHC searches for Higgs–portal dark matter". In: *Phys. Lett. B* 709 (2012), pp. 65–69. DOI: 10.1016/j.physletb.2012.01.062. arXiv: 1112.3299 [hep-ph].

[122] A. Tumasyan et al. "A portrait of the Higgs boson by the CMS experiment ten years after the discovery." In: *Nature* 607.7917 (2022), pp. 60–68. DOI: 10.1038/s41586-022-04892-x. arXiv: 2207.00043 [hep-ex].

[123] S. Banerjee, P. S. B. Dev, A. Ibarra, T. Mandal, and M. Mitra. "Prospects of Heavy Neutrino Searches at Future Lepton Colliders". In: *Phys. Rev. D* 92 (2015), p. 075002. DOI: 10.1103/PhysRevD.92.075002. arXiv: 1503.05491 [hep-ph].

[124] *KM3NeT homepage*. https://www.km3net.org.

[125] "Contributions of KM3NeT to ICRC2023". In: *38th International Cosmic Ray Conference*. Sept. 2023. arXiv: 2309.05016 [astro-ph.HE].

[126] R. Bruijn and D. van Eijk. "The KM3NeT Multi-PMT Digital Optical Module". In: *PoS* ICRC2015 (2016), p. 1157. DOI: 10.22323/1.236.1157.

[127] A. Margiotta. "The KM3NeT deep-sea neutrino telescope". In: *Nucl. Instrum. Meth. A* 766 (2014). Ed. by T. Sumiyoshi et al., pp. 83–87. DOI: 10.1016/j.nima.2014.05.090. arXiv: 1408.1392 [astro-ph.IM].

[128] Di Palma, I. "KM3NeT Time Calibration". In: *EPJ Web Conf.* 207 (2019), p. 07001. DOI: 10.1051/epjconf/201920707001. URL: https://doi.org/10.1051/epjconf/201920707001.

[129] S. Adrián-Martínez et al. "The prototype detection unit of the KM3NeT detector". In: *Eur. Phys. J. C* 76.2 (2016), p. 54. DOI: 10.1140/epjc/s10052-015-3868-9. arXiv: 1510.01561 [astro-ph.IM].

[130] S. Adrián-Martínez et al. "Deep sea tests of a prototype of the KM3NeT digital optical module". In: *Eur. Phys. J. C* 74.9 (2014), p. 3056. DOI: 10.1140/epjc/s10052-014-3056-3. arXiv: 1405.0839 [astro-ph.IM].

[131] S. Biagi, T. Chiarusi, P. Piattelli, and D. Real. "2015 Proc. 34th Int. Cosmic Ray Conf. vol 001 p 1172 (for the KM3NeT Collaboration)PoS".

[132] C. Kopper. "Development of Monte-Carlo tools for the KM3NeT neutrino telescope". In: *Nucl. Instrum. Meth. A* 626-627 (2011). Ed. by E. G. Anassontzis, P. A. Rapidis, and L. K. Resvanis, S243–S245. DOI: 10.1016/j.nima.2010.06.251.

[133] A. Gazizov and M. P. Kowalski. "ANIS: High energy neutrino generator for neutrino telescopes". In: *Comput. Phys. Commun.* 172 (2005), pp. 203–213. DOI: 10.1016/j.cpc.2005.03.113. arXiv: astro-ph/0406439.

[134] D. Chirkin and W. Rhode. "Muon Monte Carlo: A High-precision tool for muon propagation through matter". In: (July 2004). arXiv: hep-ph/0407075.

[135] G. Carminati et al. "MUPAGE: a fast atmospheric MUon GEnerator for neutrino telescopes based on PArametric formulas". In: (July 2009). arXiv: 0907.5563 [astro-ph.IM].

[136] S. Ostapchenko, T. Thouw, and K. Werner. "The new VENUS model of hadronic interactions at ultrarelativistic energies". In: *Nuclear Physics B - Proceedings Supplements* 52.3 (1997), pp. 3–7. ISSN: 0920-5632. DOI: https://doi.org/10.1016/S0920-5632(96)00843-2. URL: https://www.sciencedirect.com/science/article/pii/S0920563296008432.

[137] S. Ostapchenko. "QGSJET-II: Towards reliable description of very high energy hadronic interactions". In: *Nucl. Phys. B Proc. Suppl.* 151 (2006). Ed. by P. K. F. Grieder, B. Pattison, and L. K. Resvanis, pp. 143–146. DOI: 10.1016/j.nuclphysbps.2005.07.026. arXiv: hep-ph/0412332.

[138] S. Roesler, R. Engel, and J. Ranft. "The Monte Carlo event generator DPMJET-III". In: *International Conference on Advanced Monte Carlo for Radiation Physics, Particle Transport Simulation and Applications (MC 2000)*. Dec. 2000, pp. 1033–1038. DOI: 10.1007/978-3-642-18211-2_166. arXiv: hep-ph/0012252.

[139] R. et al Brun. "GEANT3 User Guide". In: (1985). CERN Data Handling Division: DD/EE/84-1.

[140] P. A. Aarnio et al. "FLUKA: Hadronic benchmarks and applications". In: *International Conference on Monte Carlo Simulation in High-Energy and Nuclear Physics - MC 93*. 1993.

[141] M. Bleicher et al. "Relativistic hadron hadron collisions in the ultrarelativistic quantum molecular dynamics model". In: *J. Phys. G* 25 (1999), pp. 1859–1896. DOI: 10.1088/0954-3899/25/9/308. arXiv: hep-ph/9909407.

[142] W. Ralph Nelson, H. Hirayama, and David W. O. Rogers. "The Egs4 Code System". In: (Dec. 1985).

[143] G. de Bonis. "GENHEN release v7r1". In: (2014).

[144] S. Aiello et al. "gSeaGen: The KM3NeT GENIE-based code for neutrino telescopes". In: *Computer Physics Communications* 256 (2020), p. 107477. ISSN: 0010-4655. DOI: https://doi.org/10.1016/j.cpc.2020.107477. URL: https://www.sciencedirect.com/science/article/pii/S0010465520302241.

[145] J. Schumann and B. Jung. "GiBUU based neutrino interaction simulations in KM3NeT". In: *JINST* 16.09 (2021), p. C09022. DOI: 10.1088/1748-0221/16/09/C09022. arXiv: 2107.13947 [hep-ex].

[146] A. Albert et al. "Monte Carlo simulations for the ANTARES underwater neutrino telescope". In: *JCAP* 01 (2021), p. 064. DOI: 10.1088/1475-7516/2021/01/064. arXiv: 2010.06621 [astro-ph.HE].

[147] A. G. Tsirigotis, G. Bourlis, A. Leisos, and S. E. Tzamarias. "Hellenic Open University Reconstruction \& Simulation (HOURS) software package: User Guide \& short reference of Event Generation, Cherenkov photon production and Optical Module simulation". In: (Feb. 2017). arXiv: 1702.00945 [astro-ph.IM].

[148] S. Agostinelli et al. "GEANT4–a simulation toolkit". In: *Nucl. Instrum. Meth. A* 506 (2003), pp. 250–303. DOI: 10.1016/S0168-9002(03)01368-8.

[149] M. de Jong. "JSirene : A program to simulate the detector response". In: (2012).

[150] M. de Jong. "The Jpp - JTools package". In: (2011).

[151] M. de Jong. "The Jpp - JPhysics package". In: (2011).

[152] D. Dornic, M. Colomer., and V. Kulikovskiy. "Detailed KM3NeT optical module simulation with Geant4 and supernova neutrino detection study". In: *PoS* ICRC2017 (2017), p. 983. DOI: 10.22323/1.301.0983.

[153] M. Lincetto. "Development of multi-messenger real-time analyses for the KM3NeT neutrinotelescope". PhD thesis (2021).

[154] A. J. Heijboer. "Track Reconstruction and Point Source Searches with Antares". PhD thesis (2004).

[155] Karel Melis, Aart Heijboer, and Maarten de Jong. "KM3NeT/ARCA Event Reconstruction Algorithms". In: *PoS* ICRC2017 (2018), p. 950. DOI: 10.22323/1.301.0950.

[156] S. Aiello et al. "Determining the neutrino mass ordering and oscillation parameters with KM3NeT/ORCA". In: *Eur. Phys. J. C* 82.1 (2022), p. 26. DOI: 10.1140/epjc/s10052-021-09893-0. arXiv: 2103.09885 [hep-ex].

[157] A. Trovato. "Development of reconstruction algorithms for large volume neutrino telescopes and their application to the KM3NeT detector". PhD thesis. Catania U., SSC, 2014.

[158] M. Blennow, J. Edsjo, and T. Ohlsson. "Neutrinos from WIMP annihilations using a full three-flavor Monte Carlo". In: *JCAP* 01 (2008), p. 021. DOI: 10.1088/1475-7516/2008/01/021. arXiv: 0709.3898 [hep-ph].

[159] T. Bringmann, J. Edsjö, P. Gondolo, P. Ullio, and L. Bergström. "DarkSUSY 6 : An Advanced Tool to Compute Dark Matter Properties Numerically". In: *JCAP* 07 (2018), p. 033. DOI: 10.1088/1475-7516/2018/07/033. arXiv: 1802.03399 [hep-ph].

[160] T. Sjostrand, S. Mrenna, and P. Z. Skands. "PYTHIA 6.4 Physics and Manual". In: *JHEP* 05 (2006), p. 026. DOI: 10.1088/1126-6708/2006/05/026. arXiv: hep-ph/0603175.

[161] J. Edsjö. "Nusigma 1.19 URL: http://www.wimpsim.astroparticle.se".

[162] A. N. Baushev. "Extragalactic dark matter and direct detection experiments". In: *Astrophys. J.* 771 (2013), p. 117. DOI: 10.1088/0004-637X/771/2/117. arXiv: 1208.0392 [astro-ph.CO].

[163] J. F. Navarro, C. S. Frenk, and S. D. M. White. "A Universal density profile from hierarchical clustering". In: *Astrophys. J.* 490 (1997), pp. 493–508. DOI: 10.1086/304888. arXiv: astro-ph/9611107.

[164] K. Choi, C. Rott, and Y. Itow. "Impact of the dark matter velocity distribution on capture rates in the Sun". In: *JCAP* 05 (2014), p. 049. DOI: 10.1088/1475-7516/2014/05/049. arXiv: 1312.0273 [astro-ph.HE].

[165] J. Edsjö et al. "WIMPSIM 5.0: WimpAnn, med_dec, solar_crnu and WimpEvent. 2019".

[166] J. Neyman. "Outline of a Theory of Statistical Estimation Based on the Classical Theory of Probabilit". In: *Phil. Trans. R. S. of London* Ser. A. 236 (1937), pp. 333–380. DOI: 10.1103/PhysRevLett.121.111302.

[167] Aalbert et al. "First all-flavor neutrino pointlike source search with the ANTARES neutrino telescope". In: *Phys. Rev.* D 96 082001 (2017). DOI: 10.1103/PhysRevD.96.082001.

[168] S. Adrián-Martínez et al. "Intrinsic limits on resolutions in muon- and electron-neutrino charged-current events in the KM3NeT/ORCA detector". In: *JHEP* 05 (2017), p. 008. DOI: 10.1007/JHEP05(2017)008. arXiv: 1612.05621 [physics.ins-det].

[169] A. Sánchez-Losa. "Search for high energy cosmic muon neutrinos from variable gamma-ray sources and time calibration of the optical modules of the ANTARES telescope". PhD thesis (2015).

[170] C. Tonnis. "Indirect search for dark matter in the Sun and the Galactic Centre with the ANTARES neutrino telescope". PhD thesis (2017).

[171] A. Nuñez-Castiñeyra. "From cosmological simulations to Dark Matter detection". PhD thesis (2020).

[172] D. López. "Dark Matter and Solar Atmospheric Neutrino Searches with the KM3NeT-ORCA and ANTARES Neutrino Telescopes". PhD thesis (2022).

[173] R. B. Davis et al. “Hypothesis Testing”. In: *Circulation* 114 (2006), pp. 1078–1082. DOI: 10.1161/circulationaha.105.586461.

[174] M. G. Aartsen et al. “Search for annihilating dark matter in the Sun with 3 years of IceCube data”. In: *Eur. Phys. J. C* 77.3 (2017). [Erratum: Eur.Phys.J.C 79, 214 (2019)], p. 146. DOI: 10.1140/epjc/s10052-017-4689-9. arXiv: 1612.05949 [astro-ph.HE].

[175] S. Adrián-Martínez et al. “Limits on dark matter annihilation in the sun using the ANTARES neutrino telescope”. In: *Physics Letters B* 759 (2016), pp. 69–74. ISSN: 0370-2693. DOI: https://doi.org/10.1016/j.physletb.2016.05.019. URL: https://www.sciencedirect.com/science/article/pii/S0370269316301666.

[176] K. Choi et al. “Search for neutrinos from annihilation of captured low-mass dark matter particles in the Sun by Super-Kamiokande”. In: *Phys. Rev. Lett.* 114.14 (2015), p. 141301. DOI: 10.1103/PhysRevLett.114.141301. arXiv: 1503.04858 [hep-ex].

[177] R. Abbasi et al. “Search for GeV-scale dark matter annihilation in the Sun with IceCube DeepCore”. In: *Phys. Rev. D* 105.6 (2022), p. 062004. DOI: 10.1103/PhysRevD.105.062004. arXiv: 2111.09970 [astro-ph.HE].